ANALYSIS AND PREDICTABILITY OF THE 1 DECEMBER 2011 WASATCH DOWNSLOPE WINDSTORM

by

John Lawson

A thesis submitted to the faculty of
The University of Utah
in partial fulfillment of the requirements for the degree of

Master of Science

Department of Atmospheric Science

The University of Utah

December 2013

The University of Utah Graduate School

STATEMENT OF THESIS APPROVAL

The thesis of **John Lawson**

has been approved by the following supervisory committee members:

John D. Horel	, Chair	**7/22/2013** Date Approved
W. James Steenburgh	, Member	**7/22/2013** Date Approved
Courtenay Strong	, Member	**7/22/2013** Date Approved

and by **Kevin D. Perry** , Chair/Dean of

the Department/College/School of **Atmospheric Sciences**

and by David B. Kieda, Dean of The Graduate School.

ABSTRACT

A downslope windstorm on 1 December 2011 led to considerable damage along a narrow 50-km swath at the western base of the Wasatch Mountains in northern Utah. Operational forecasts issued by the Salt Lake City National Weather Service Forecast Office provided accurate guidance for the event at lead times of 1–2 days, based in part on their locally-generated high-resolution numerical forecasts. The strongest surface winds began suddenly around 0900 UTC, primarily in the southern portion of the damage zone. Surface winds reached their peak intensity (gusts to 45 m s^{-1}) at ~1600 UTC, while the strongest winds shifted later to the northern end of the damage swath. The northward shift in strong surface winds relates to the rotation of synoptic-scale flow from northeasterly to easterly at crest level, controlled by an evolving anticyclonic Rossby wave-breaking event. A rawinsonde released at ~1100 UTC in the midst of strong (>35 m s^{-1}) easterly surface winds initially travelled horizontally before ascending rapidly within a downstream rotor. The sonde subsequently intersected a strong inversion at the top of the rotor due to dry air descending sharply from above crest level.

Weather Research and Forecasting (WRF) model simulations were completed to assess: (1) the fidelity of high-resolution models (1.3-km horizontal grid spacing) to resolve the dynamics of this downslope windstorm, and (2) why there was apparent enhanced predictability in high-resolution model guidance 1–2 days in advance. A simulation was initialized from North American Mesoscale analyses at 0600 UTC 29 November 2013 and forced on the outermost boundary over the next 72 h by subsequent analyses at 6-h intervals. The model simulation captured core features of the downslope wind event, including the spatial extent and timing of the strongest surface winds. However, the model developed stronger mountain-wave breaking in the lee of the Wasatch, a broader hydraulic jump, and a downstream rotor located farther west than observed. To investigate the predictability of this windstorm, an 11-member ensemble of 72-h WRF high-resolution

forecasts was initialized from 0000 UTC 29 November 2011 reforecasts from the Global Ensemble Forecast System. Eight of the eleven members generated a strong, localized windstorm with the outliers arising from reduced cross-barrier synoptic-scale flow.

For my parents, and wife Maggie.

CONTENTS

LIST OF FIGURES

LIST OF TABLES

ACKNOWLEDGMENTS

I thank Professor John Horel for constructive criticism, dedication to my progression, and (most importantly) a good sense of humor. I thank my two committee members, Professors Courteney Strong and Jim Steenburgh, for careful reading of drafts and useful suggestions. I thank the WRF-Users Group in the Department of Atmospheric Science for valuable assistance along the way. I thank WRF-Help in Boulder, CO, for vital assistance in running the ensemble reforecasts. I thank all in the Mountain Meteorology Group here in the Department for tips and tricks (sorry, *solutions*), and in particular, Trevor Alcott for many valuable words (paragraphs?) of advice. I thank Roger Akers, Chris Ander, Erik Crosman, Alex Jacques, Matt Lammers, Nola Lucke, Wil Mace, and Trevor Alcott, all for assistance in collecting data during the windstorm; I thank the latter again for going out during a second windstorm just for kicks! I thank the Center for High-Performance Computing at the University for provision of, maintenance of, and assistance with the supercomputers.

Finally, I thank my parents for support over the years, and my wife Maggie — mostly for her amazing patience.

This research was supported by NOAA/NWS Collaborative Science, Technology, and Applied Research Program Grant No. NA10NWS4680005.

CHAPTER 1

INTRODUCTION

Downslope windstorms are characterized by strong and gusty winds at the base of steep lee slopes of mountain ranges (American Meteorological Society 2013). Due to the damage often associated with them, downslope windstorms obtained local names in areas experiencing them frequently, including the föhn, bora, chinook, zonda, Santa Ana, and Wasatch (Whiteman 2000; Richner and Hächler 2013). Downslope windstorms of the type discussed in this study have been extensively investigated, and arise when a layer of air is forced over a terrain barrier and sandwiched between the barrier and a strongly-stable layer aloft (Markowski and Richardson 2010).

The Wasatch windstorm of 1 December 2011 caused over $75 million damage in a 3–5-km-wide, 50-km-long swath primarily in Davis County and extending northward into Weber County (O'Donoghue 2012). Some damage was experienced to the south in Salt Lake County. The urban–suburban corridor, from Utah County in the south to Weber County in the north, comprises most of what is referred to locally as the Wasatch Front (Figure 1.1). The narrow damage zone (yellow box in Figure 1.1) affected the suburban cities (from north to south) of Ogden (Weber County), Layton, Farmington (Figure 1.2), Centerville, and Bountiful (all Davis County). The impacts included the following: rail traffic was halted along the Wasatch Front; as many as 70,000 trees were uprooted or damaged; and power was lost in many communities after over 22 transformers were damaged and 1.5 km of power lines required maintenance. In addition, Interstate 15 was closed to large vehicles after many were blown over on the freeway. Subsequently, several trucks blew over on the adjacent frontage road to which they were detoured. A disaster declaration for this event was issued by the President of the United States on 1 February 2012.

This study focuses on this extreme example of a Wasatch windstorm and builds on prior climatological work and a case study of a modest event by Holland (2002). Data

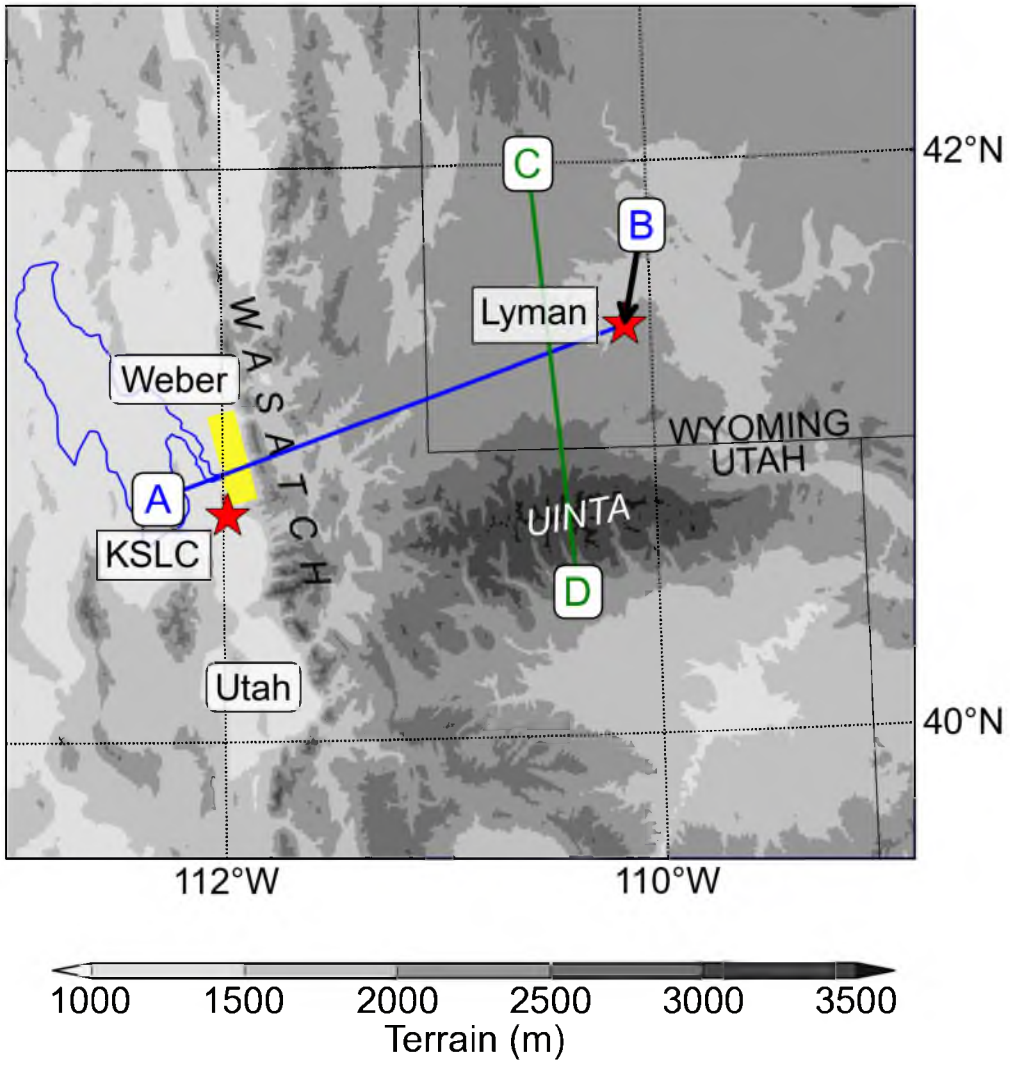

Figure 1.1: Terrain elevation in northern Utah and western Wyoming (shading). Locations, state names, mountain ranges, and cross-section paths mentioned in the text are also shown. The Wasatch Front is the low-lying region paralleling the west slopes of the Wasatch. Centerville (Davis County) lies at the intersection of the blue A–B cross-section and the Wasatch Front. KSLC is Salt Lake International Airport in Salt Lake County. Yellow shading along the Wasatch Front shows the approximate damage swath on 1 December 2011.

Figure 1.2: Damage sustained during the downslope windstorm of 1 December 2011 at a construction site near Station Park Mall in Farmington, UT. (Photo: John Horel)

and methods used are presented in Chapter 2 while details of the windstorm's anatomy, including its synoptic environment, are presented in Chapter 3.

An anemometer sited by Union Pacific Railroad in Centerville, UT, along a stretch of rail line prone to high winds during downslope windstorms, recorded a maximum gust of $45\,\mathrm{m\,s^{-1}}$ (102 mph) at ~1600 UTC [1] 1 December 2011 (Figure 1.3). Strong winds were not only observed along the Wasatch Front on this day, but also in other localized areas across the western United States; for example, southern California experienced one of its strongest Santa Ana events in recent years (Welch and Rice 2011; Abatzoglou et al. 2013).

As discussed by Richner and Hächler (2013), the general synoptic features associated with localized downslope windstorms are well understood and reasonably well predicted. However, operational numerical weather prediction models do not necessarily capture details regarding their timing and intensity. Forecasting the occurrence of downslope windstorms has long been recognized to require several critical ingredients (Smith 1985;

[1] Local time in Utah is 7 h earlier than UTC during winter.

Figure 1.3: Anemometers installed in Centerville, UT by Union Pacific Railroad (MesoWest identifier: CENWWS; foreground) and Utah Department of Transportation (MesoWest identifier: CEN; background) where the peak winds were observed during the 1 December 2011 windstorm. (Photo: John Horel)

Markowski and Richardson 2010, pp. 327–352). First, the terrain barrier must be: (1) quasi-two-dimensional so that air cannot simply flow around it, and (2) asymmetrical with a more gentle windward slope combined with a steep lee slope. However, no single terrain characteristic is tied to strong-windstorm environments. As shown in Table 1.1, there is no obvious dependence on the downstream valley-to-crest vertical distance. In addition, the lee-side slope gradient is variable; windstorms have been documented in the lee of crests that rise only 200–300 m above the downstream valley (Marriott 1886; Mobbs et al. 2005; Decker and Robinson 2011). Figure 1.3 depicts the steep profile along the Wasatch Front, near Centerville, UT. Here, the flat base of elevation 1280 m above mean sea-level (MSL) rises eastward towards the crest of the Wasatch mountains (2500–2750 m in this region).

Second, a sufficiently-strong cross-barrier wind ($>15\,\mathrm{m\,s^{-1}}$) must impinge on the barrier; a wind direction orthogonal to a two-dimensional barrier will maximize mountain-wave excitation in the same direction downstream (Jiang 2002). Third, the vertical profiles of temperature, moisture, and wind should be conducive to amplifying the development of mountain lee waves. This typically requires one or more of the following characteristics:

Table 1.1: Approximate characteristic linear slopes upstream of some documented downslope-windstorm locations estimated using Google Earth software.

	Crest–base horiz. distance	**Crest–base vertical distance**	**Slope**	**Reference**
Wasatch Front, UT, USA	5.9 km	1.3 km	22%	Horel et al. (2002a)
(Wasatch Front in WRF)	(6.5 km)	(1.1 km)	(17%)	(30-s WRF terrain)
Owens Valley, CA, USA	11 km	2.5 km	22%	Grubišić and Billings (2008)
High Point, NJ, USA	1.2 km	0.2 km	19%	Decker and Robinson (2011)
Juneau, AK, USA	7.4 km	1.1 km	15%	Colman and Dierking (1992)
East Falkland, Falkland Is.	3.3 km	0.4 km	13%	Mobbs et al. (2005)
Senj, Croatia	8.7 km	1.0 km	11%	Smith and Sun (1987)
Helm Wind, UK	5.3 km	0.6 km	11%	Manley (1945)
Boulder, CO, USA	39 km	2.3 km	6%	Lilly and Zipser (1972)
Mendoza, Argentina	116 km	5.0 km	2%	Norte et al. (2008)

(1) a strongly-stable layer upstream of and above the crest level (Vosper 2004); (2) an environmental *critical level* above crest level, where the cross-wind component decreases to zero and/or reverses direction; (3) a *wave-induced critical level* (Peltier and Clark 1979), where wave-breaking itself generates a wind reversal above crest level that is not found in upstream wind profiles; and (4) the synoptic environment should favor subsidence aloft, but not favor the development of a deep cold-air pool in the lee of the range that might inhibit penetration of strong winds to the surface.

National Weather Service (NWS) forecasts issued by the Salt Lake City Forecast Office for the 1 December 2011 Wasatch windstorm were ample for public and private contingency planning in terms of spatial and temporal accuracy, forecast lead time, and wind speed magnitude. The first Area Forecast Discussion (AFD) to mention a potential for strong winds along the Wasatch Front on 1 December was issued at 1712 UTC 27 November (90 h before the onset of the windstorm) and the matter was discussed in the subsequent Hazardous Weather Outlook (HWO). All further AFDs and HWOs issued by the Salt Lake City Forecast Office mentioned the chance for high winds, with increasing confidence as the event drew closer. The potential for high winds was cited in many AFDs to be based on: (1) the similarity between the developing synoptic situation and situations typically observed during Wasatch windstorms, and (2) confidence in both the numerical model guidance from operational forecast models and a higher-resolution model run locally at the Forecast Office [2].

In addition to NWS forecasts, the public received substantial warning through the media of the impending storm, particularly on 30 November, and through freeway message signs alerting travelers to high winds the next day (Figure 1.4). On 30 November, Utah Department of Transportation (UDOT) personnel sited a portable weather station in a high-wind-prone location to obtain additional observations for nowcasting purposes, in addition to three portable weather stations placed in key locations by a University of Utah (UoU) team. A UoU research plan was quickly drawn up on 30 November to collect additional

[2]Weather Research and Forecasting mesoscale model runs were made four times a day with boundary conditions based on the prior Global Forecast System model. The regional domain was 12 km, and nested down to 4 km across Utah. Each run produced hourly guidance through 60 forecast hours. This was the first major downslope windstorm where forecasters had access to high-resolution forecast guidance in their operational office environment (Randy Graham and Steve Rogowski, 2012, personal communication).

Figure 1.4: Utah Department of Transportation message sign in Davis County on 30 November 2011, highlighting the conditions expected the next day. (Photo: John Horel)

observations the next day using portable rawinsonde systems and vehicle-mounted sensors. Since there had not been a major Wasatch windstorm in many years, there was interest in collecting as much data as possible to supplement the automated observations in the region. While a major downslope windstorm was deemed likely by forecasters, and supported by high-resolution deterministic model output, UoU team confidence was not particularly high regarding the specific details (timing, location, and intensity) of the high-resolution numerical guidance provided by the NWS. This concern was in part motivated by the existence of strong winds far west into the Great Salt Lake in the 4-km-domain model output, ultimately an incorrect prognosis.

The accuracy of forecast-model guidance and 24–48-h NWS forecasts for the damaging winds of 1 December 2011 helped motivate this study to examine this apparent enhanced predictability. For example, two weaker Wasatch windstorms in April and May 2013 occurred with much shorter warning times, despite reliance on comparable operational and local high-resolution model guidance and forecaster expertise. Strong easterly winds across a similar swath seen in this study occurred overnight 4–5 May 2013; wind reached $12\,\mathrm{m\,s^{-1}}$ sustained and $20\,\mathrm{m\,s^{-1}}$ gusts at Hill Air Force Base (KHIF). While this does not match this study's definition of a Wasatch windstorm, and winds elsewhere in Davis County

were slightly below High Wind Warning criteria (i.e., 1 h of 18 m s^{-1} sustained winds), the magnitude of winds were underestimated in previous AFDs by over a factor of two. The possibility of strong winds had been discussed in previous AFDs, but had ultimately been judged to be unlikely; in this case, the underestimation in wind speed was most likely related to shortcomings in numerical model output (Steenburgh 2013).

Predictability theory would suggest forecasts of mesoscale phenomena on spatial scales of 10–40 km could only be successful up to 1–2 h lead times (Lorenz 1969). Reinecke and Durran (2009) evaluated ensemble forecasts of downslope windstorms in the lee of the Sierra Mountains of California and estimated predictability timescales of O(12 h) for their two case studies. As summarized by Doyle et al. (2013), numerous studies have suggested that error growth might be reduced, and predictability enhanced, for mesoscale phenomena such as downslope windstorms as a result of terrain–flow interactions. Furthermore, events that are strongly coupled with larger-scale (i.e., typically more-predictable) phenomena may inherit some predictability from the larger scales (Palmer 1993, e.g.,). Predictability (dealing with uncertainties arising from numerical-model and initial-condition errors) and forecast skill (dealing with the accuracy of a particular model forecast) are not synonymous (Silver 2012, p. 14). Success of downslope windstorm forecasts should be judged using accuracy of the wind speed magnitudes, locations of strongest winds, and onset and cessation times. We address predictability, and the simulation of this windstorm in numerical models, in Chapter 4.

The objective of this study is to examine the 1 December 2011 Wasatch downslope windstorm from several distinct perspectives. The specific questions to be addressed, and the means by which those questions are addressed, are summarized as follows:

1. **How does this downslope wind storm compare to previous ones?** ERA-Interim reanalyses are used to examine the synoptic setting for this and 12 other Wasatch windstorms since 1979.

2. **What were the local characteristics of this event?** When did it start and end? Where were the winds the strongest? What was the vertical structure of the atmosphere upstream and downwind of the Wasatch Mountains? Local observations from conventional sources, and those collected specifically during a small field campaign,

are used to discuss the spatial extent, timing, and intensity of the surface winds, and the windstorm's vertical structure.

3. **To what extent can a high-resolution model simulation capture temporal and spatial evolution of mesoscale and local features of the event?** A nested control model simulation of the windstorm, using lateral boundaries updated every 6 h from North American Mesoscale (NAM) model analyses, is used to diagnose its overall evolution.

4. **What are the impacts of upstream mountain ranges that may deflect the flow traveling towards the Wasatch Mountains?** The Uinta Mountains (a west–east oriented mountain range located upstream of the Wasatch when the prevailing flow is from the east, see Figure 1.1) are flattened in a model simulation, and the resulting modified wind and thermodynamic profiles are compared to those in the control simulation.

5. **Is the enhanced forecast skill for this windstorm evident in an ensemble reforecast?** An 11-member ensemble from the Global Ensemble Forecast System Reforecast, Version 2 (GEFS/R2, Hamill et al. 2013) of the National Oceanographic and Atmospheric Administration (NOAA) is used to force high-resolution mesoscale model forecasts. The resulting spread in the intensity and timing of the strongest downslope winds among the ensembles members is then examined.

We evaluate the findings prompted by these questions in Chapter 5, and summarize future work that may follow from this study.

CHAPTER 2

DATA AND MODEL SETUP

2.1 Reanalysis and observational data

European Centre for Medium-Range Weather Forecasts (ECMWF) Re-Analysis (ERA)-Interim data (Dee et al. 2011) are used in this study to diagnose the synoptic-scale evolution associated with the downslope windstorm. The ERA-Interim uses a four-dimensional variational data-assimilation system that ingests observations within a 12-hr window around the analysis time. The postprocessed data used in this study are available at 6-hr intervals (00, 06, 12, 18 UTC); fields on pressure surfaces were bi-interpolated from their native grid (0.75°-by-0.75°) to a 1°-by-1° grid.

Surface observations of meteorological and other environmental parameters were obtained from the MesoWest archive (Horel et al. 2002b). Reports from over 280 automated reporting stations were available within 80 km (50 mi) of Centerville, UT, the location of strongest winds on 1 December 2011. There are substantive differences in the siting, equipment, and reporting characteristics of the automated observations available in MesoWest. Wind observations were manually evaluated to identify the time and intensity of the strongest observed winds.

An ad hoc UoU team of staff and students assembled during the morning of 30 November 2011 to determine where additional observations would best improve evaluation of the expected windstorm. Decisions were made and implemented that afternoon to deploy three automated weather stations: (1) near Morgan, UT, east of the Wasatch Range, to monitor upstream conditions; (2) east of Bountiful, UT, ∼500 m in elevation above the foot of the slope and as far up as it was practical to drive given the weather and mountain road conditions; and (3) Glover's Lane in Farmington, UT, ∼1.5 km west of the base of the Wasatch (Figure 2.1). Two mobile Graw rawinsonde systems were prepared for the next day: one to be sited where the portable automated weather station was deployed near

(a)

(b)

Figure 2.1: Two of the three temporary weather stations deployed for the 1 December 2011 windstorm at (a) Bountiful Bench (UFD05), Bountiful, UT, and (b) Glover's Lane (UFD04), Farmington, UT. (Photos: John Horel)

Morgan, UT (upstream of the Wasatch Mountains); the other to be deployed as needed in the lee of the range based on how the conditions evolved. Two vehicles were also equipped with roof-mounted GPS, wind, temperature, humidity, and pressure sensors. However, one of the roof-mounted racks was destroyed early the next day in the high winds.

2.2 Model setup

Boundary conditions for higher-resolution model simulations were provided by six-hourly NAM reanalyses, run by the National Centers for Environmental Prediction (NCEP). For the purpose of predictability experiments, we obtained GEFS/R2 datasets (Hamill et al. 2013), hosted at `ftp://ftp.cdc.noaa.gov/Projects/Reforecast2/`. These reforecasts (i.e., hindcasts that are made with reanalyses) consisted of a lower-resolution control run, generated from Climate Forecast System Reanalysis data, and 10 ensemble members, each with perturbed initial conditions generated via the ensemble transform technique with rescaling (ETR, Wei et al. 2008).

Numerical simulations were performed with the Weather Research and Forecasting (WRF) model using the Advanced Research WRF dynamical core (WRF-ARM). All runs comprised three nested domains of grid size 12, 4, and 1.3 km (Figure 2.2), whose boundary conditions were provided every 6 h by the NAM or GEFS/R2 as applicable. The domains allowed two-way feedback; high-frequency waves were damped with sixth-order diffusion on the largest domain. Topography was interpolated from datasets at a resolution of 10 min for the 12-km domain, and 30 s for the 4- and 1.33-km domains, to the WRF-model grids. To avoid Courant-Friedrichs-Lewy criterion violation in regions of active mountain-wave breaking, vertical resolution was limited to 40 vertical levels. WRF output was interpolated onto a pressure-coordinate grid using the National Center for Atmospheric Research (NCAR) tool *p_interp*. Further details and parametrization options are listed in Table 2.1.

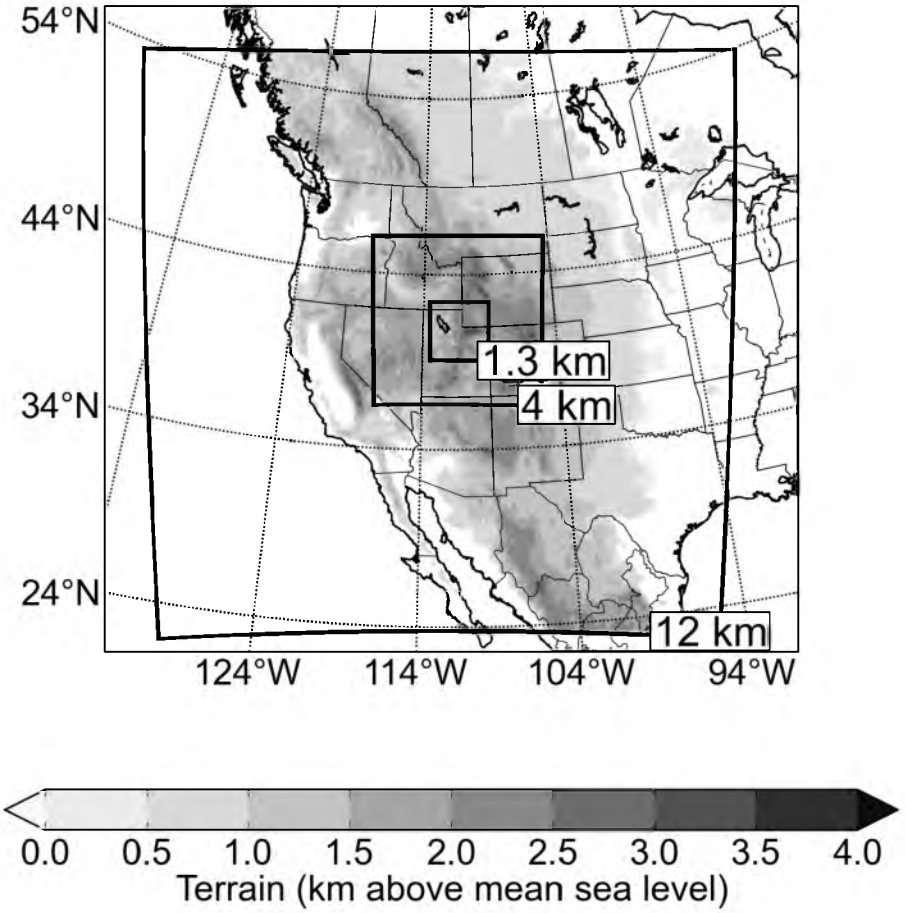

Figure 2.2: Domain areas for the 12-, 4-, and 1.3-km domains in the Weather Research and Forecasting model. Terrain is from the 12-km domain at 10-min resolution.

Table 2.1: Parameterization schemes used in numerical modeling configuration.

	Parameterization name
Microphysics	WRF Single-Moment 3-class Scheme
Longwave Radiation	RRTM Scheme
Shortwave Radiation	Dudhia Scheme
Surface Layer	MM5 Similarity
Land Surface	Noah Land Surface Model (with snow effect)
Urban Surface	Switched off
Planetary Boundary Layer	Yonsei University Scheme
Cumulus Parameterization	Kain-Fritsch Scheme (12-km, 4-km domains only)
Latent/Sensible Heat Flux	Allowed
Vertical Velocity Damping	Switched off
6th-Order Horizontal Diffusion	Simple (12-km domain only)

CHAPTER 3

OBSERVATIONAL RESULTS

3.1 Climatology

Windstorms along the Wasatch Front (Figure 1.1) occur in climatologically-anomalous easterly flow at crest level (Holland 2002), and hence are rarer than those that occur on lee slopes downwind of prevailing midlatitude westerly flows. As discussed by Holland, few meteorological surface stations in the vicinity of the Wasatch Mountains are located in appropriate locations or have extensive enough records to develop climatologies of Wasatch windstorms. For example, Salt Lake International Airport (KSLC) is too far west of the range and does not experience strong downslope winds during these events (see Figure 1.1).

Following Holland (2002), observations from KHIF in Layton, UT (northern Davis County) are used to examine the occurrence of strong downslope winds between 1 October 1979 and 30 April 2012 (the period for which the ERA-Interim reanalyses are available). Due to its position downwind of Weber Canyon, KHIF frequently experiences easterly drainage flows in addition to occasional downslope windstorms. Holland (2002) found easterly wind gusts $>23\,\mathrm{m\,s^{-1}}$ about 1.5 times per year during the period 1953–1999, with more events observed in the earlier years than the later ones. The lower frequency of events in these later years may partially result from increased sensor exposure on the Base, and surrounding suburban development. However, there has been little change in obstructions during the data period used in this study. The strongest wind gust recorded at KHIF was $45\,\mathrm{m\,s^{-1}}$ on 4 April 1983. Holland (2002) derived composites of geopotential height on standard pressure levels for 79 strong easterly wind events using coarse-resolution (2.5° latitude/longitude grid) NCEP/NCAR reanalyses. Consistent with synoptic experience and forecasting practices at that time, the dominant composite signal described in that study was the development of a closed geopotential-height low on the 700-hPa surface, southwest of the Wasatch Mountains and centered near Las Vegas, NV. Receiving less attention in that

study, but nonetheless evaluated as equally statistically significant, was the development to the north of the Wasatch Mountains of an anticylonic geopotential-height ridge at 700 hPa, which extended from coastal Washington state, curving through Montana, to Wyoming. This cyclone–anticyclone structure is consistent with the life-cycle 1 (LC1) type of Rossby-wave breaking, i.e., anticyclonic Rossby wave breaking (ARWB) that features a narrow potential vorticity (PV) tongue tilted in the west- and equatorward direction (Thorncroft et al. 1993).

A more conservative definition for strong Wasatch windstorms than that applied by Holland (2002) is used in this study. A high wind event between October and April inclusive must satisfy the following criteria: (1) at least one KHIF observation with greater than 15 m s^{-1} sustained winds from an easterly direction between 45° and 135°; and (2) that time's upper-tropospheric pressure and potential-temperature data must indicate a Rossby-wave-breaking pattern (either anticylonic as described above, or cyclonic LC2 type with a trough or closed low tilting in the east- and poleward direction, Thorncroft et al. 1993). One high-easterly-wind event at KHIF met criterion (1), but not (2), and was ignored. In addition, multiday events were reduced to a single day if they were associated with the same upper-level wave-breaking event. These criteria led to identification of 13 distinct downslope windstorms between 1 October 1979 and 30 April 2012 inclusive. Table 3.1 shows their dates and sustained speeds and wind gusts.

The list of dates in Table 3.1 and the time series of their occurrence during 1979–2012 (Figure 3.1) suggests that major downslope windstorms occurred once or twice every few years until 1999. Subsequently, no major downslope windstorm occurred until the 1 December 2011 event investigated here. The intermittency of Wasatch windstorms, particularly the lack of windstorms in the first decade of this century, begs the question of whether their occurrence is determined by fewer Rossby-wave breaking events over western North America, or more fundamentally, by fewer crest-level easterly wind periods during the winter-half of the year. Strong and Magnusdottir (2008) developed an objective detection algorithm that generated a worldwide Rossby-wave-breaking climatology. Since their criteria allowed for weak and localized wave-breaking events, examination of their data as part of this study did not yield any apparent linkage to the occurrence of Wasatch windstorms. Figure 3.1 also shows the frequency of easterly (between 45° and 135°)

Table 3.1: Downslope windstorm events at KHIF as defined by this study.

	Time of max. wind, UTC	**Maximum wind speed, m s^{-1} (mph)**	**Maximum wind gust, m s^{-1} (mph)**
9 October 1979	1500	15 (34)	21 (48)
19 January 1980	1200	15 (34)	22 (49)
4 April 1983	1700	21 (46)	31 (70)
30 March 1984	1200	15 (34)	18 (41)
16 January 1987	1740	15 (34)	20 (44)
24 December 1987	0700	15 (34)	21 (46)
15 December 1988	1200	16 (36)	23 (51)
30 January 1993	1700	18 (41)	21 (48)
12 January 1997	1100	17 (38)	23 (52)
24 February 1997	1700	18 (40)	23 (51)
2 April 1997	1600	15 (34)	24 (53)
23 April 1999	1755	18 (40)	24 (53)
1 December 2011	1655	20 (45)	30 (67)

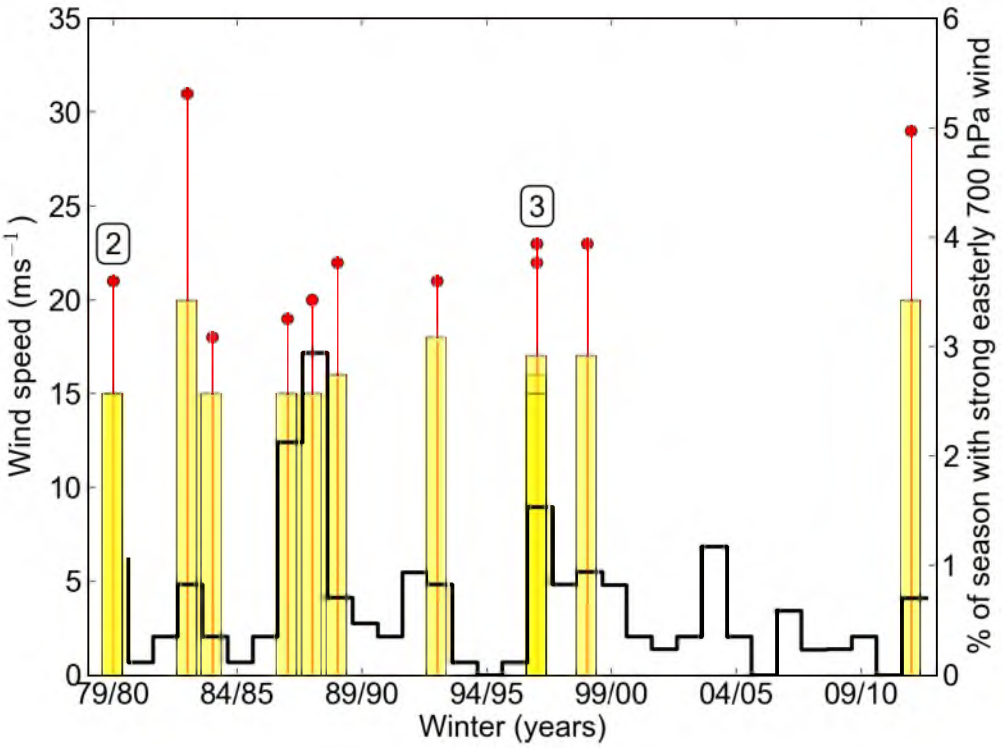

Figure 3.1: Sustained and gust wind speeds associated with downslope windstorms as a function of winter season at KHIF, and percent of season with strong crest-level winds from easterly direction. Wind speed indicated by yellow bars according to the scale on left. Red stems indicate the maximum gust associated with that windstorm. Percent of season with strong 700 hPa winds from easterly direction in ERA-Interim Reanalysis data marked by black line (according to scale on the right). Box above year indicates that year has more than one event (number of events denoted by number). Two events in the winter of 1979/80 have almost identical values and hence overlap on the chart.

crest-level (700 hPa) winds over $10\,\mathrm{m\,s^{-1}}$ during each winter season (Oct–April inclusive) from the ERA Interim Reanalyses. Since crest-level strong-easterly-wind periods do occur in the years that downslope windstorms were absent, the seasonal frequency of easterly winds is not a good predictor for the rare occurrences of downslope windstorms within those seasons. Hence, major Wasatch downslope windstorms require coincidence of a number of synoptic-scale and mesoscale factors (Markowski and Richardson 2010).

Following McIntyre and Palmer (1984), the gradient of potential temperature on the dynamic tropopause ($\nabla\theta_{DT}$) is calculated from ERA-Interim reanalyses to highlight the 'surf zone' of breaking Rossby waves. The dynamic tropopause is defined as the surface on which potential vorticity is equal to 2 PVU ($1\,\mathrm{PVU} = 10^{-6} m^2 s^{-1} K kg^{-1}$). As shown in Figure 3.2, a deep trough is evident in the 13-member composite of high wind events, marked by high pressure on the dynamic tropopause centered over southern Nevada [1]. This deep trough is ringed by high $\nabla\theta_{DT}$, with the largest values associated with the exit region of the upper-level polar jet, downstream of the Rossby-wave trough axis. A second band of high $\nabla\theta_{DT}$ is evident near 25°N that results from the position of the subtropical jet during some, but not all, of these windstorm events (not shown).

In our climatology of major windstorms (Table 3.1), the hour of peak wind at KHIF varies from 0700 UTC to 1800 UTC. In general, the peak in widespread downslope winds along the Wasatch Front tend to occur near sunrise (~1200 UTC), since the dynamical forcing associated with the downslope winds is in phase at that time with thermally-forced drainage flows down slopes and valleys (and out of phase with thermally-forced upslope and upvalley winds in the afternoon). Hence, similar to Holland (2002), we show in Figure 3.3 composites of 700-hPa geopotential height, assuming that the peak downslope wind occurs near 1200 UTC, and then composite conditions from 12 h earlier (0000 UTC) to 6 h after (1800 UTC). Southwestward extension of the anticyclonic 'surf zone' to the north of the Wasatch Front (e.g., Figure 3.3, 0600 UTC) marks the ARWB event, while the associated closed low deepens from 0000 to 1200 UTC following by filling. The strongest easterly gradient winds across the Wasatch Front are evident at 1200 UTC.

---

[1] Equatorward protrusions of high pressure on the dynamic tropopause are referred to as troughs, due to their correspondence to geopotential-height minima (Hoskins et al. 1985, p. 890).

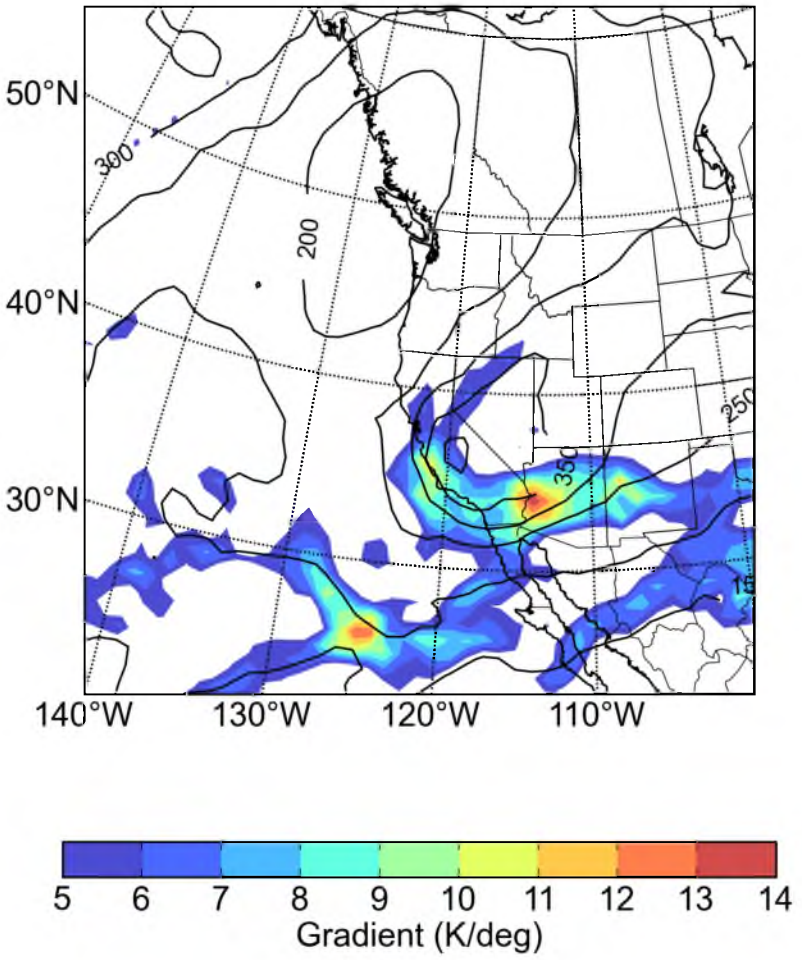

Figure 3.2: Thirteen-event composite of the magnitude of potential temperature gradient on the dynamic tropopause from ERA-Interim reanalysis data, valid at 1200 UTC for each cas. Shading according to the scale at the bottom. The gradient computation assumes, for simplicity, that one degree of latitude is approximately one degree of longitude across the plot domain. Composite-mean pressure of the dynamic tropopause surface contoured every 50 hPa.

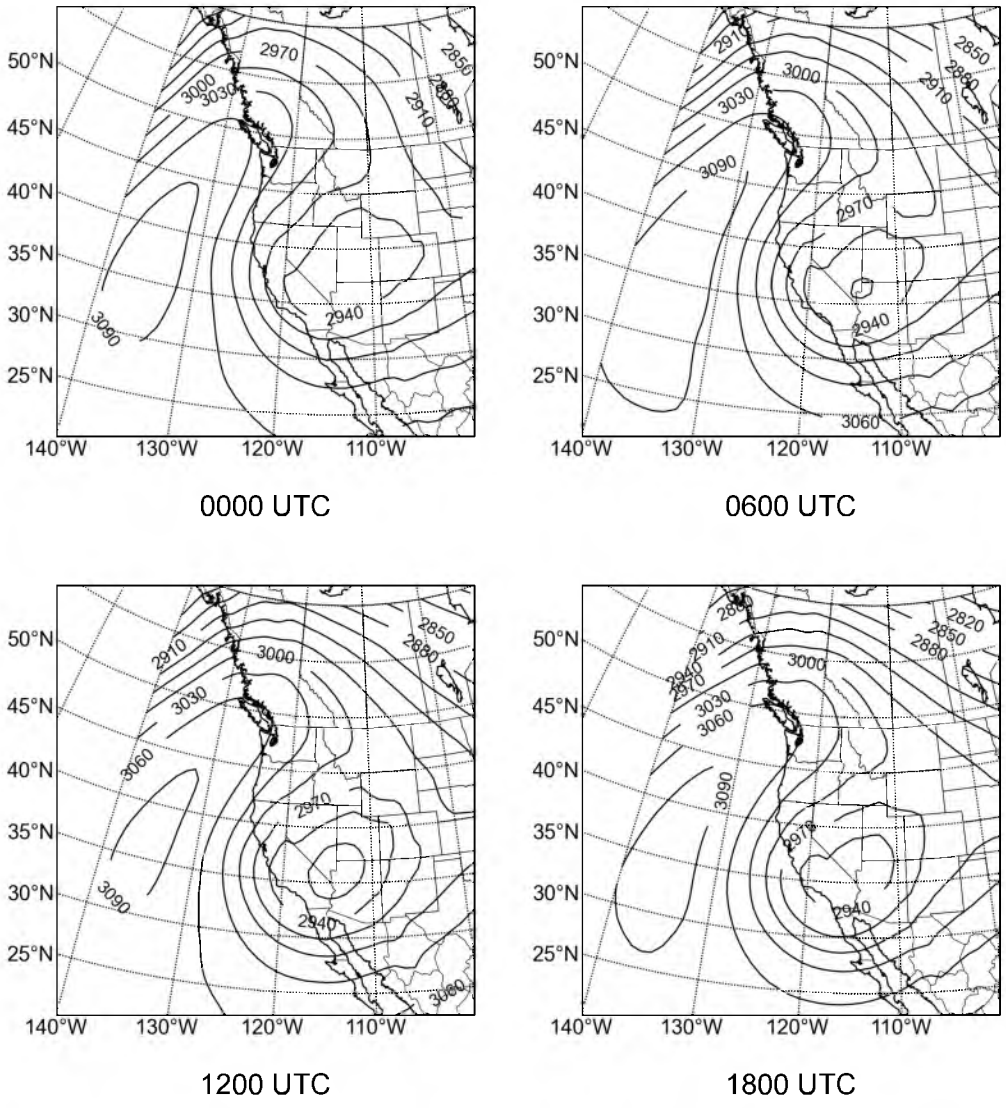

Figure 3.3: Evolution of thirteen-event composite ERA-Interim 700-hPa geopotential height, contoured at 30-m intervals, at 0000, 0600, 1200, and 1800 UTC on 1 December 2011.

3.2 1 December 2011 windstorm

The Wasatch windstorm of 1 December 2011 was one of the most powerful windstorms ever recorded along the Wasatch Front. As discussed in the Introduction, damage estimates were in excess of $75 million and wind gusts reached 46 m s^{-1} (89 kt, 102 mph). Wasatch windstorms are typically associated with ARWB in the mid-to-upper troposphere. We highlight this wave-breaking pattern in Figure 3.4, which presents the horizontal $\nabla\theta_{DT}$ field at 6-h intervals during 0000–1800 UTC 1 December. The positively-tilted trough and ridge structure is reminiscent of Life Cycle 1 (LC1) for baroclinic waves (Thorncroft et al. 1993, their Figure 12). Note the clockwise, pivoting rotation of the northwestern segment of the breaking wave, which corresponds to an increasing easterly component of wind at the tropopause level over much of the western United States. As the base of the trough slowly moves southeast, $\nabla\theta_{DT}$ increases downstream of the trough axis, particularly between 0000 and 0600 UTC. This period is associated with strong surface cyclogenesis around the Nevada–Arizona border (not shown). Reported wind gusts over 25 m s^{-1} increase in number across the western United States during this period; their locations are shown by stars in Figure 3.4. Strong wind-gust reports spread across northern Utah and northeastern Nevada as the trough axis passes overhead around 1200 UTC. In Southern California, widespread strong wind gusts accompanying a Santa Ana event occurred on the upstream side of the trough axis.

More directly relevant to the Wasatch Front windstorm, the breaking-wave pattern is evident in the 700-hPa geopotential-height field (Figure 3.5). A small southwest-moving wave in the height field, accompanied by a jet maximum, moves faster than the mean flow towards the base of the trough between 0000 and 1200 UTC. The transport of cyclonic vorticity into the trough axis may contribute to the deepening of the closed low over the Nevada–Utah–Arizona borders: 700-hPa heights drop 60 m between 0000 and 0600 UTC, and fall another 30 m between 0600 and 1200 UTC. Lower-tropospheric cyclogenesis is often seen with LC1 baroclinic waves as the closed maximum of PV detaches from its reservoir (Thorncroft et al. 1993). The closed-low center does not move far while its central height falls and the anticyclonic ridge breaks to the north. This clockwise pivoting of the breaking wave, and its slow southeastward progression, sustained a belt of 25m s^{-1} easterly winds on the northwestern quadrant of the low-height center. By 1200 UTC, the crest of

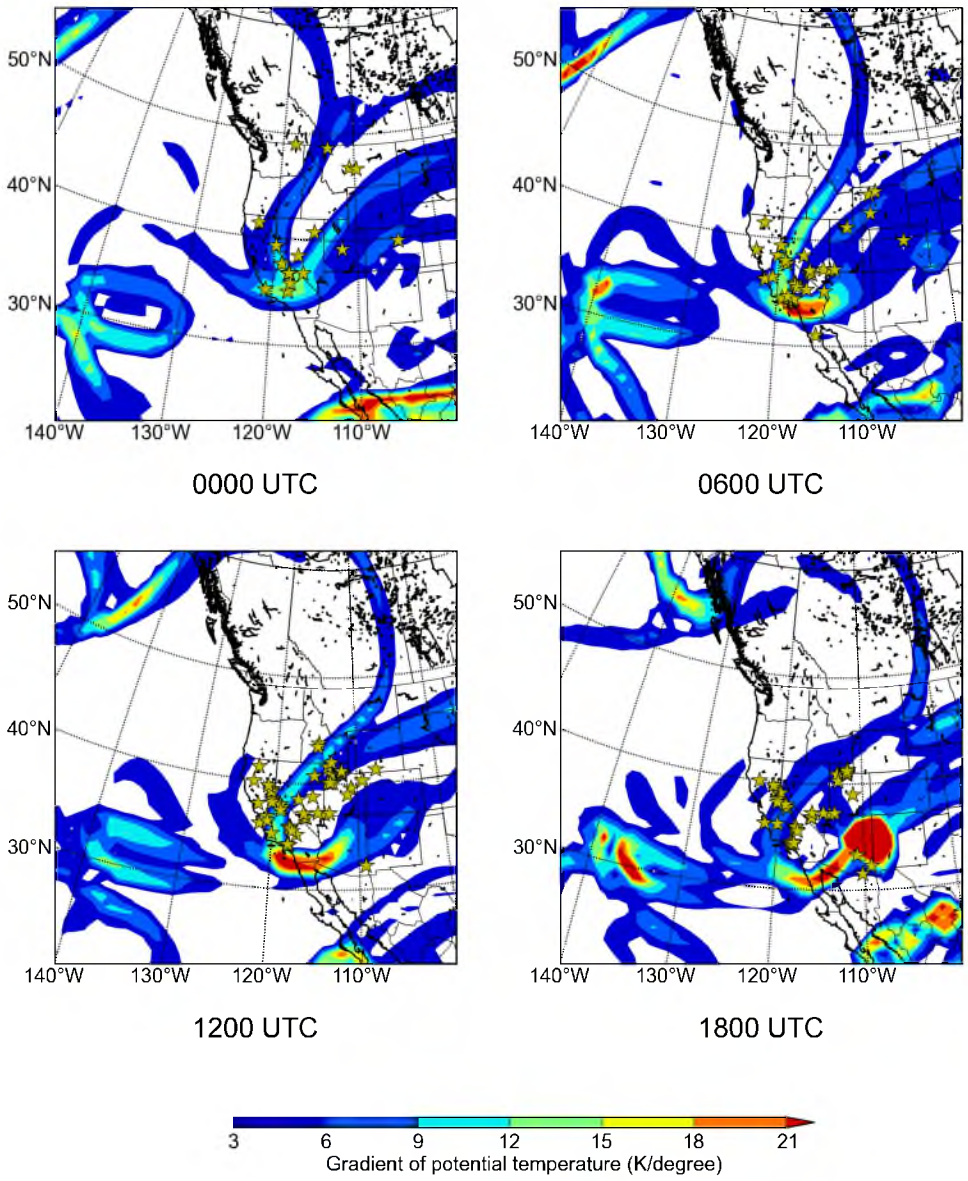

Figure 3.4: Anticyclonic Rossby-wave breaking in relation to surface winds on 1 December 2011. Strong gradient in potential temperature on the dynamic (PV = 2 PVU) tropopause (shading, see scale) are shown. Yellow stars indicate where surface gusts were measured in excess of 25 m s^{-1}, within 30 min of each plot time.

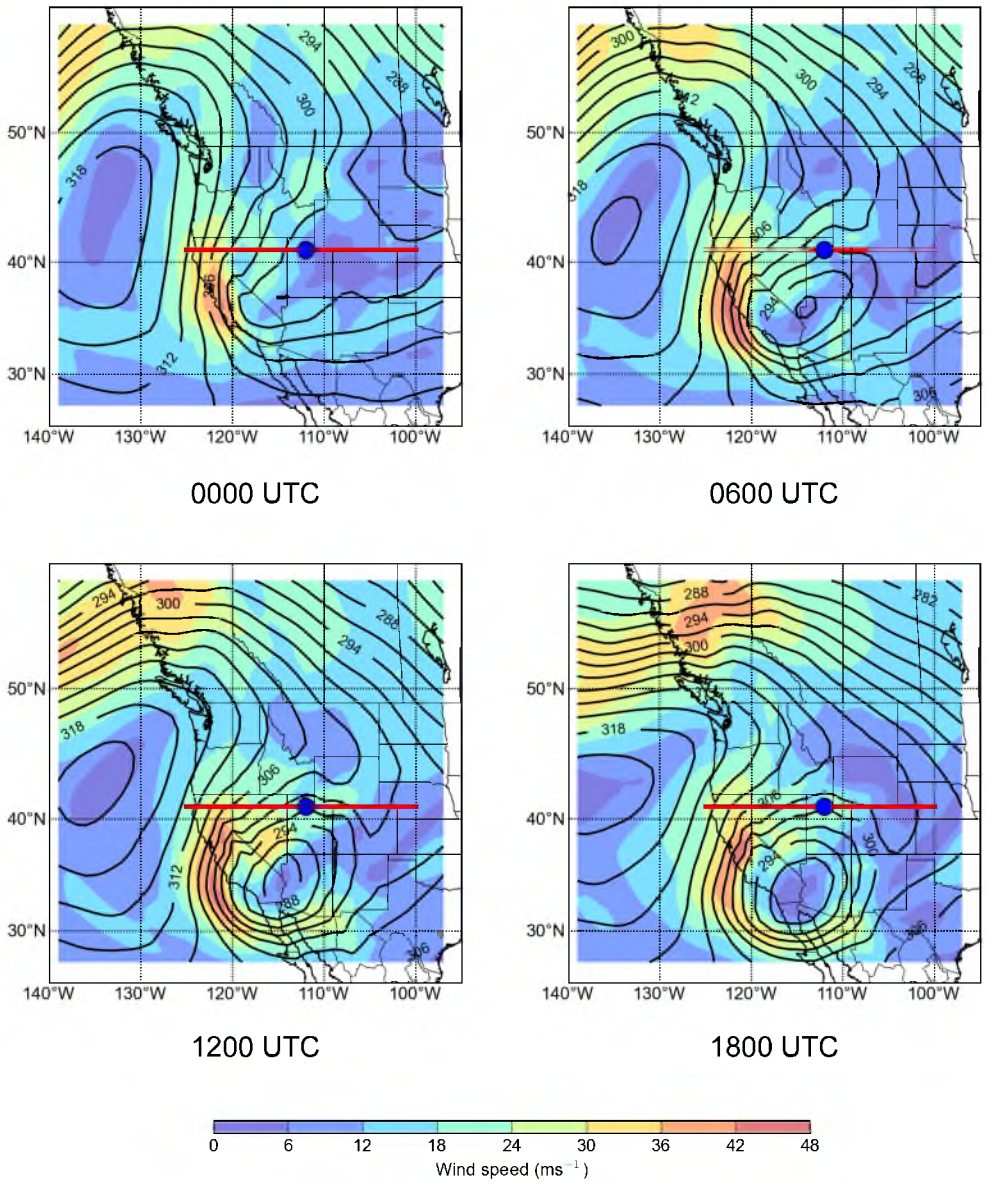

Figure 3.5: Evolution of ERA-Interim 700-hPa geopotential height (contours at 3-decameter intervals) and wind speed (shading according to scale) on 1 December 2011.

the Wasatch Front (~700 hPa; marked with a dot) lies downstream of this jet.

A longitude–pressure cross-section of zonal wind and potential temperature (Figure 3.6), taken on a slice along the red line in Figure 3.5 at 1200 UTC, shows the northeasterly (entrance) and southwesterly (exit) jets encircling the deep cyclone. Based on ERA-Interim reanalysis data, a low-level easterly jet is surmounted by a statically-stable layer to the east of the Wasatch Front (the Wasatch Front's position is marked by the vertical line) and, further aloft, cross-barrier flow reversal. As mentioned in the Introduction, this elevated stable layer and flow reversal are conducive to initiation and amplification of mountain waves.

Pressure and storm-relative wind on the 292.5-K isentropic surface are shown in Figure 3.7 for 1200 UTC. The fast-moving trough exiting Montana is evident, as is the dome of cold air extending southward from Nevada into southern California associated with the upper-level closed low. In a Lagrangian (parcel-following) framework, unsaturated parcels ascend as they ride up the isentropic surface towards lower pressure. Assuming the isentropic surface is stationary and that the air remains unsaturated, air parcels carried from Wyoming towards Utah in the easterly flow within the 600–700 hPa layer would tend to descend sharply as they approach the Wasatch Front and then ascend as they enter Nevada. In other words, the trough entering Wyoming is lifting the air parcels on the isentropic surface to the east of the Wasatch at this time. However, since the 292.5-K surface is itself moving in this area due to the passage of the upper level trough, the surface's speed is estimated crudely as equivalent to the southeasterly movement of the midtropospheric trough crossing the Rockies. This constant speed is subtracted from the winds interpolated to the 292.5-K isentropic surface as shown in Figure 3.7. Thus, the storm-relative motion in Figure 3.7 is even more easterly and associated with sharp descent across the Wasatch Front. Later, as the pressure trough advanced farther east away from the Wasatch Front, the isentropic surface descends, leading to further subsidence aloft (not shown). Together, adiabatic warming through this two-fold descent contributes to the sloping stable layer evident in Figure 3.6. Although the use of the storm-relative motion of the upper-level trough crossing Wyoming is not appropriate for southern California, the steep north-south descent of the pressure surfaces on the 292.5-K surface hints at the strong subsidence taking place across that region, which contributes to the Santa Ana conditions there.

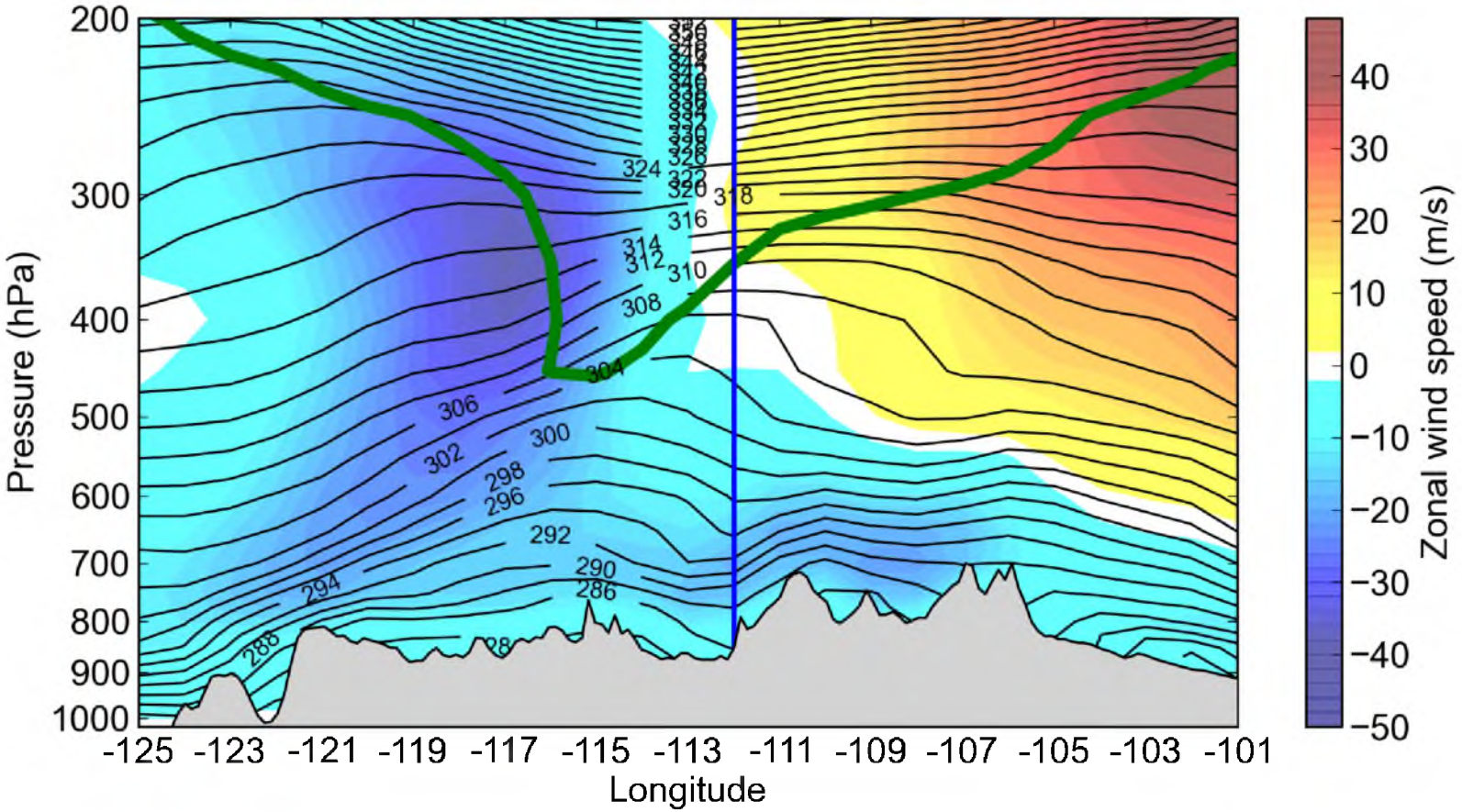

Figure 3.6: West–east cross-section of ERA-Interim reanalysis potential temperature (contours at 2-K interval) and zonal wind (shading according to the scale on the right) at 1200 UTC 1 December 2011. Cross-section path is marked by red lines in Figure 3.5. Green contour denotes pressure of dynamic tropopause (i.e., where potential vorticity = 2 PVU), for comparison with Figure 3.4.

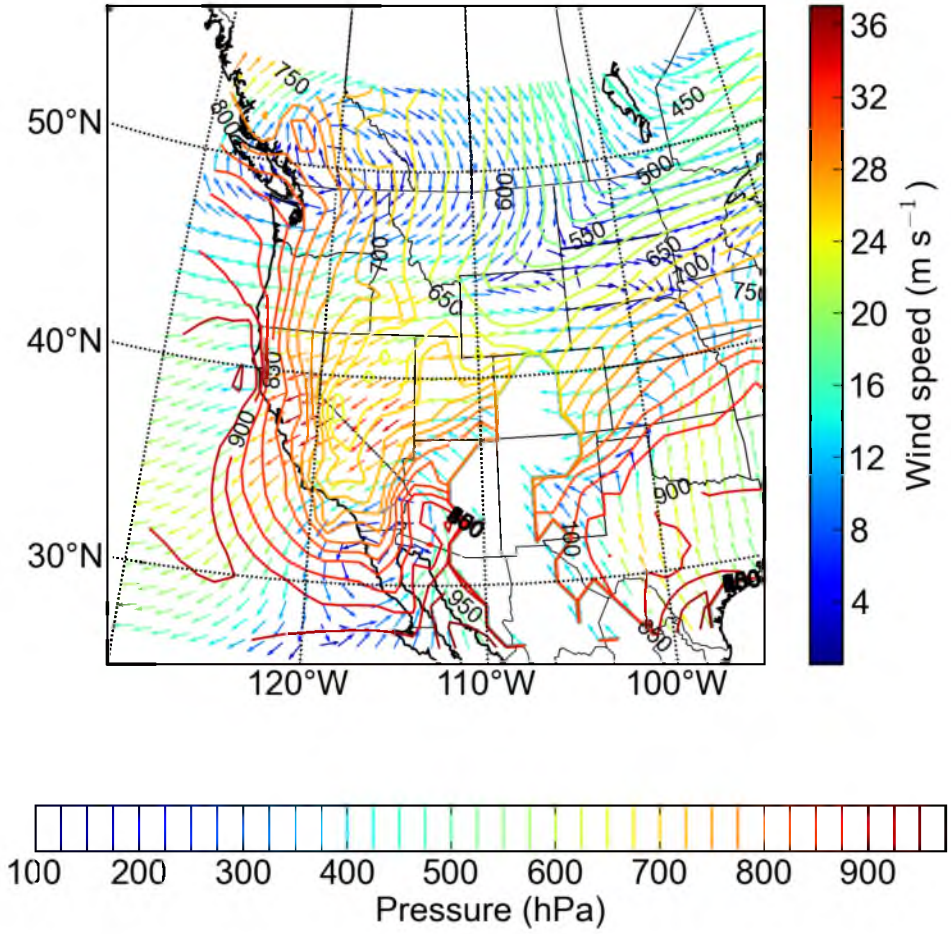

Figure 3.7: Pressure (colored contours at 25-hPa intervals) of the 292.5-K isentropic surface. Vectors estimate the magnitude (colors) and direction of the motion of unsaturated air relative to the movement of the surface. The movement of the 292.5-K surface is estimated from the speed and direction of the trough traveling across Wyoming, Montana, and North Dakota.

Figure 3.8a shows the time series of surface winds at KHIF on 1 December 2011 with most observations reported at hourly intervals. The strongest downslope winds were observed at this location during 1500–1800 UTC, preceded by a brief period of strong winds at 1200 UTC. Figure 3.8b shows wind speed and direction at Glover's Lane (UFD04), a station installed temporarily in Farmington, UT the previous evening by the UoU team and located 1.5 km from the base of the Wasatch. The observations of wind speed and direction at 1-min intervals capture the sudden onset and cessation of the downslope windstorm at 0900 and 1900 UTC respectively, and show winds reaching their peak intensity at this location ~1500–1600 UTC. In contrast to the sudden onset and cessation of downslope winds in the valley, winds at the crest of the Wasatch as measured at Ogden Peak (OGP, Figure 3.8c) show a persistent easterly flow with winds increasing in intensity until late afternoon. Similar features were observed at another nearby crest-level station at the Snowbasin Ski Resort (not shown).

The high-frequency variability at UFD04 emphasizes the turbulent nature of the downslope winds. The 1-min sampling interval at UFD04 provides opportunity to check for, and estimate periodicity of, Kelvin-Helmholtz wave-breaking in the downslope flow (Peltier and Scinocca 1990) during periods when the winds were at least 15m s^{-1} (0900–1800 UTC). A second-order Butterworth low-pass filter was applied, forward and backward, with a 60-min cutoff frequency. Power spectral density (PSD) periodograms were then produced with the *psd* function in the Python package *matplotlib*. To contrast the data against a null hypothesis of non-zero-memory noise, a red-noise time series was computed. The resulting plots of power spectral density reveal pulsations in wind speed on the time scale of 7–13 min. The pressure (8 min) and temperature (10–12 min) pulsations have similar periodicity. Positive covariance between wind speed and temperature, and negative covariance between pressure and wind speed, indicates air reached the surface through mechanical turbulent mixing (not shown). As mountain waves break on the lee side, they advect air of higher potential temperature and lower pressure down to the valley floor, measured during a wind gust. Through the windstorm, the temperature slowly decreased with cold air advected in from the east. This cooling effect is seen in Bora windstorms (Smith and Sun 1987), where upstream air is so cold that temperatures do not rise on the lee side, in contrast to so-called 'snoweater' Föhn windstorms whose compressional warming and

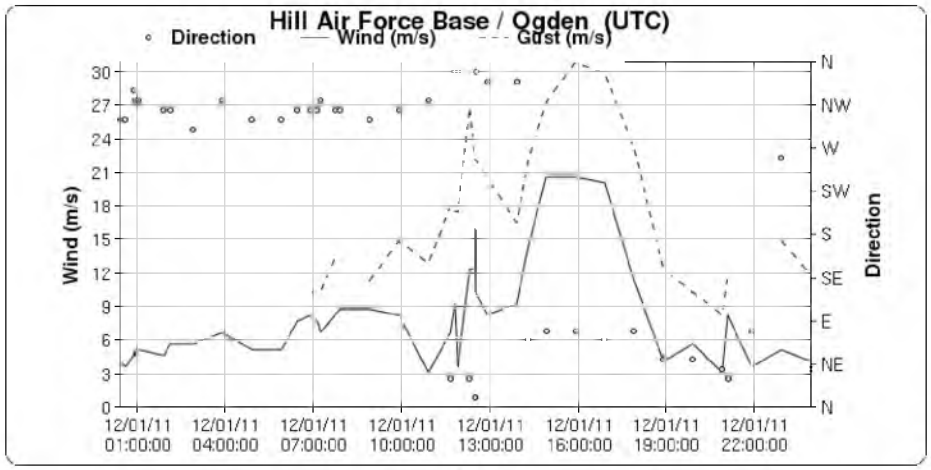

(a)

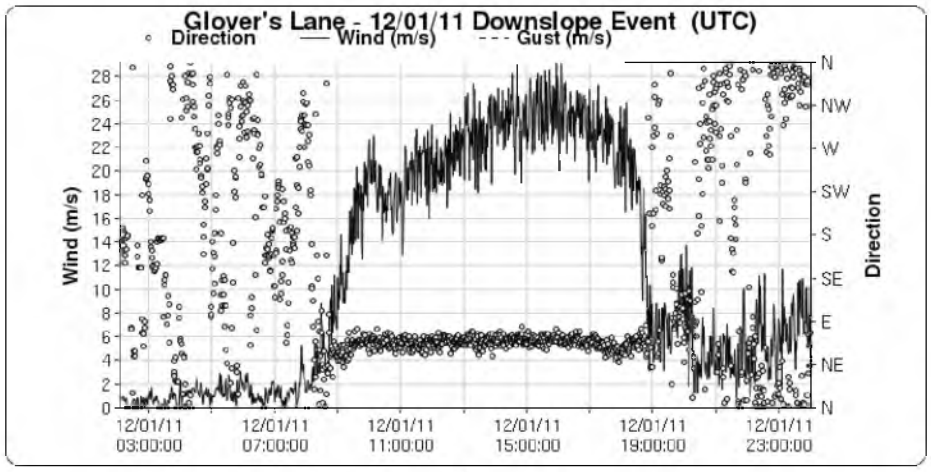

(b)

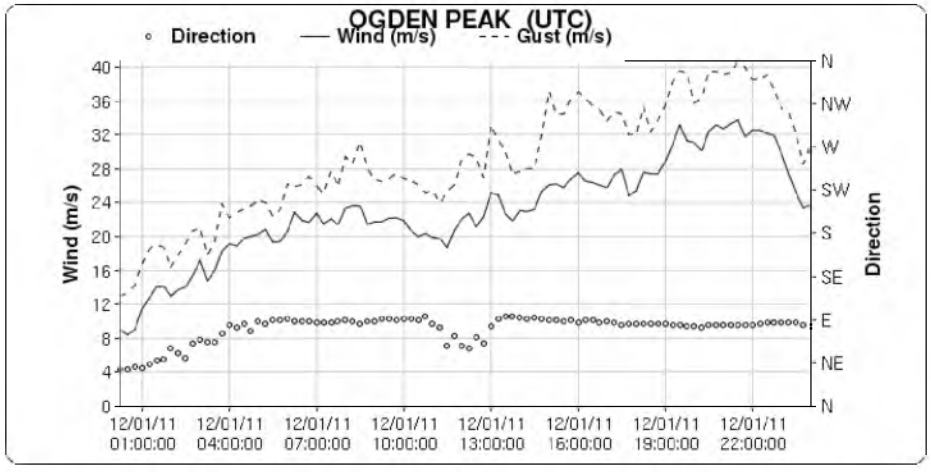

(c)

Figure 3.8: Surface wind observations at (a) Hill Air Force Base (KHIF), (b) Glover's Lane (UFD04), and (c) Ogden Peak (OGP) on 1 December 2011. Wind speed, wind gust, and wind direction shown by solid lines, dashed lines, and open circles, respectively.

latent heat release modifies air of previously equal temperature downstream and upstream of the crest, respectively (Whiteman 2000).

A snapshot of the spatial variability in wind, temperature, and moisture at 1200 UTC 1 December is shown in Figure 3.9. This display from data archived in MesoWest shows wind barbs and values of wind gusts at all available stations, as well as wind speed, direction, gusts, temperature, and dewpoint temperature at selected stations. For example, the extreme gustiness of the winds at KHIF at this time is evident. The core location for the windstorm at this time is in the Farmington (UFD04) and Centerville (CEN) areas. In the Weber River Valley upstream (east) of the Wasatch Mountains, wind is light near the surface (Morgan, UFD06) and some flow channelling is evident near the exit of the the Weber River Canyon (Power Plant, PWR). Crest-level winds at OGP are quite strong, with slightly lower winds on the lee slope of the range (Bountiful Bench, UFD05). Westerly winds associated with rotor return flows are measured in some locations (UTLGP) while the prevailing strong northerly synoptic-scale flow is evident over the Great Salt Lake far away from the Wasatch range (Hat Island, HATUT). Winds are much lighter at KSLC slightly south of the domain plotted in Figure 3.9. Bursts of strong winds leading to uprooted trees were observed beginning at 1100 UTC in northeastern portions of Salt Lake City (e.g., the University of Utah campus) where the terrain is favorable for downslope flow from the northeast (not shown). Dry-bulb temperatures are in the 1–4°C range in most valley locations, and dewpoint temperatures are low (-7 to -12°C). Over the next 6 h, dry-bulb and dewpoint temperatures dropped as a result of the continued push of colder, drier air into the region (Figure 3.10). Strong downslope-wind conditions now extend from Bountiful north to Ogden, encompassing KHIF. Winds upstream (UFD06) remain light, in contrast to strong winds at the crest (OGP), near the exit of the Weber River canyon (PWR), and along the lee slope (UFD05). Surface manifestations of rotors aloft are evident by the westerly winds observed near Woods Cross (AU031).

Figure 3.11 shows the locations of sensors that reported greater than 15m s^{-1} sustained wind during 1 December 2011. Strong valley winds (left panel) were confined close to the base of the lee slopes of the Wasatch Mountains, with the strongest values occurring near Centerville in Davis County (see also Figures 3.9 and 3.10). The crest-top station at OGP (at the extreme north of the panel) sampled the cross-barrier easterly flow evident

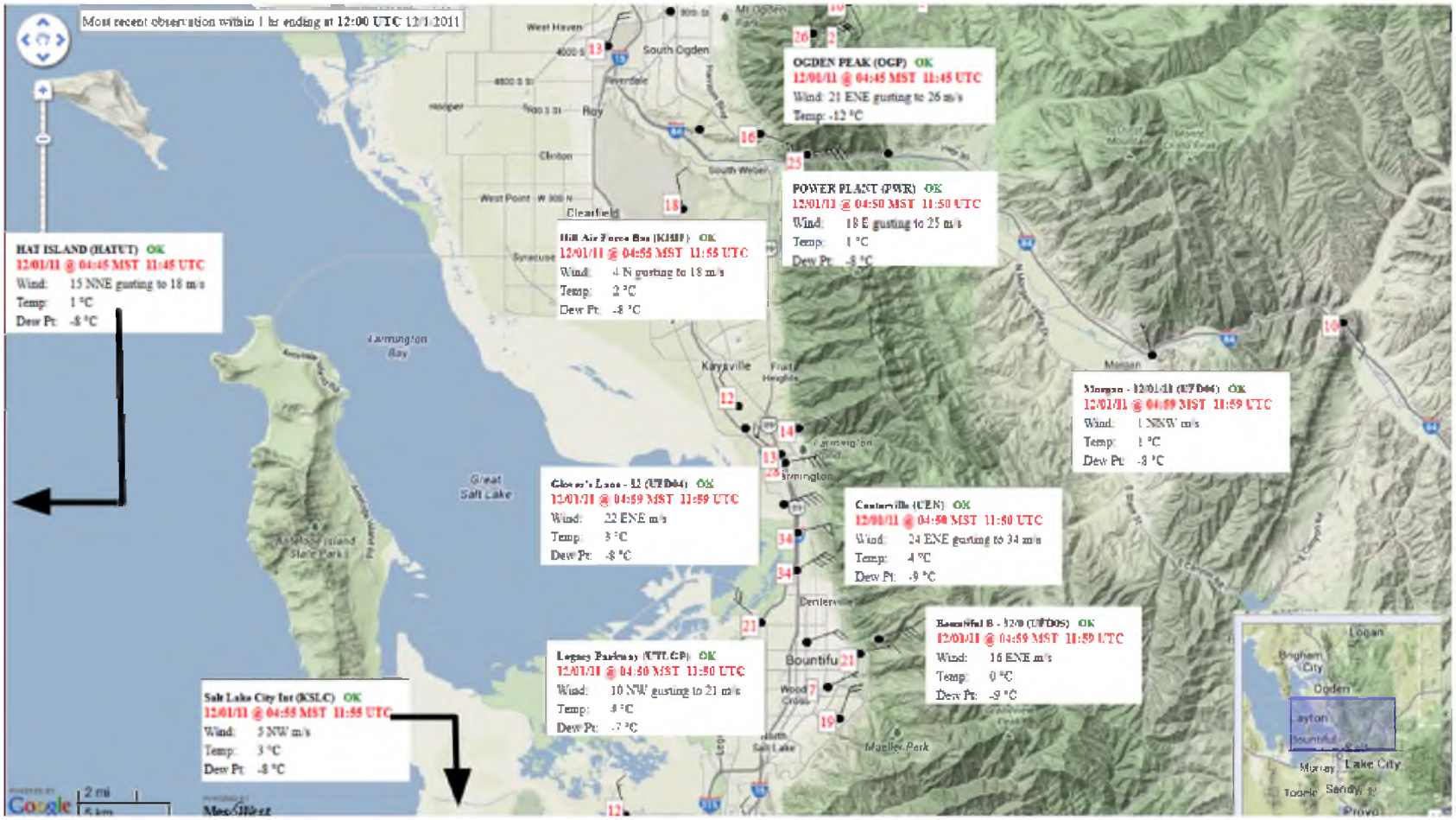

Figure 3.9: Surface observations in northern Utah at 1200 UTC 1 December 2011. Wind speed denoted by barbs (full barb 5 m s^{-1}) and wind gusts in m s^{-1} labeled where available. Wind, dry-bulb temperature, and dewpoint temperature at selected stations shown for selected stations.

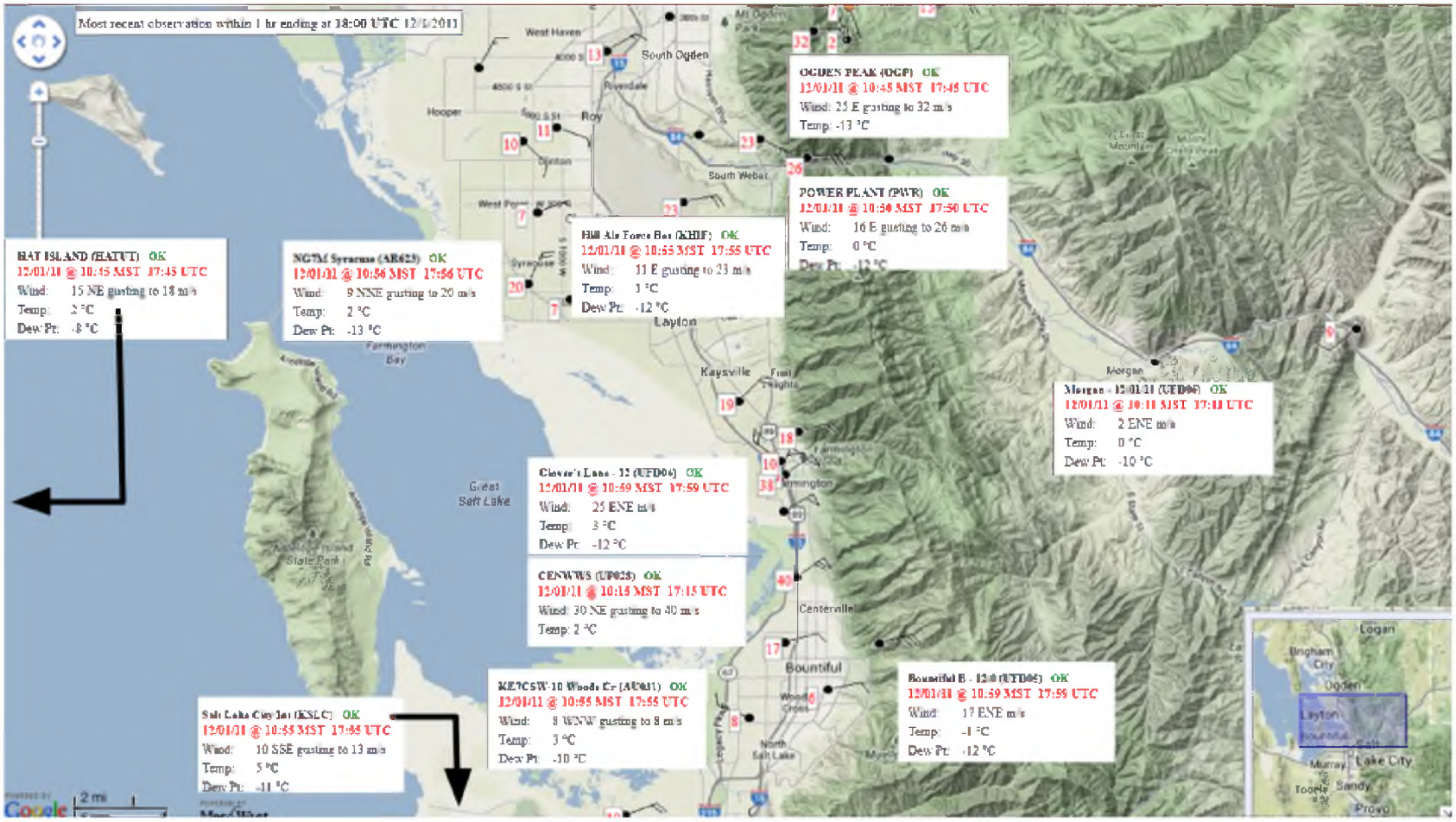

Figure 3.10: As in Figure 3.9, but for 1800 UTC.

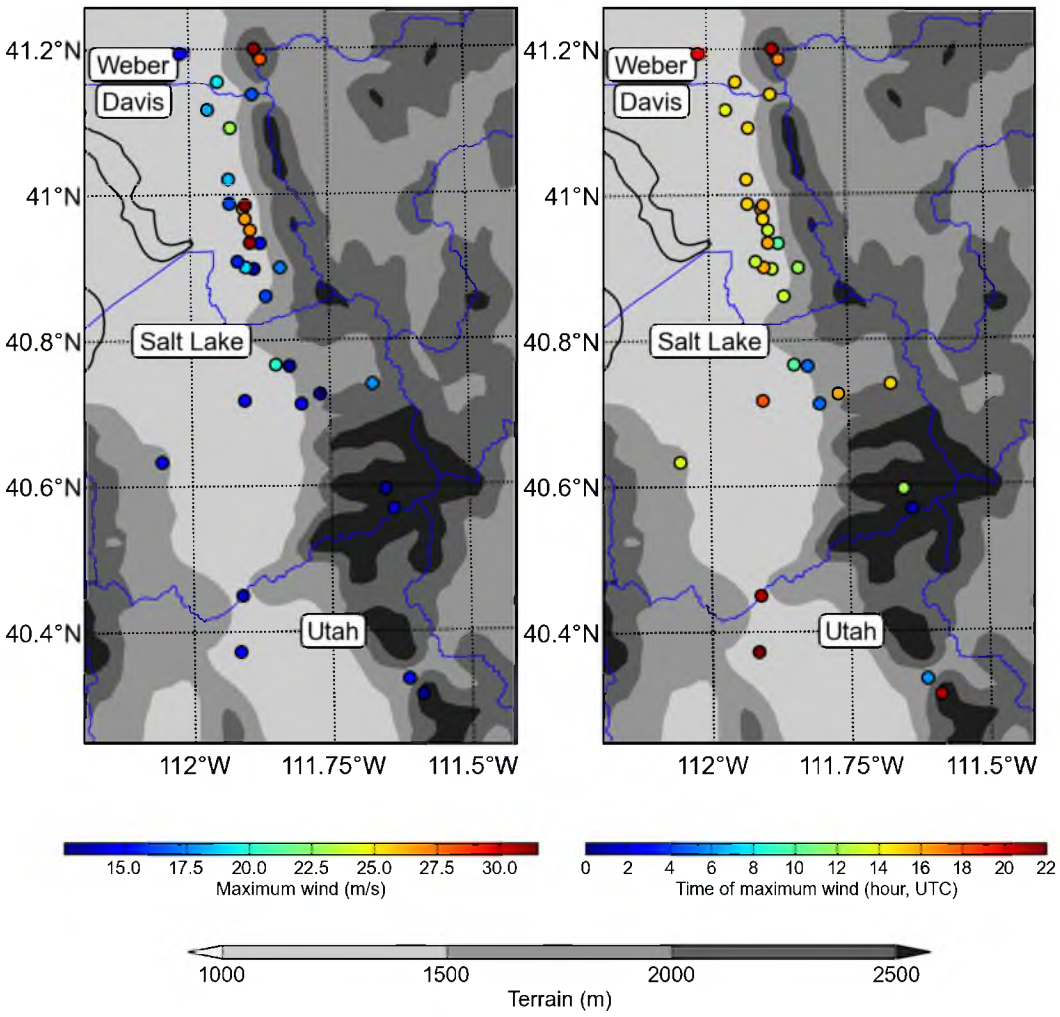

Figure 3.11: Maximum sustained wind gusts greater than 15 m s^{-1}, near the Wasatch Front on 1 December 2011 (left) and their time (UTC) of occurrence (right).

in previous figures with the strongest cross-barrier flows later in the day. The times of the valley stations' maximum wind speed (right panel) suggest that the peak winds shifted northward through the day for stations close to the base of the lee slopes of the Wasatch Range. This progression is likely related to evolution of synoptic-scale flow: as the Rossby wave broke, cross-barrier flow rotated from the northeast to east from early morning to the afternoon, respectively. Times for peak winds for the stations away from the base of the Wasatch are a function more of the large-scale northerly wind, and are independent of the downslope windstorm *per se*.

In addition to fixed observation sites, vehicle-mounted sensors were driven along primarily north–south transects throughout the morning. In addition, east–west extensions into the Weber Canyon were performed to sample the canyon flows past PWR. Another east–west transect traversed to UFD05 to observe the flows along the lower slopes of the Wasatch. The first northward transect along the Wasatch Front (between 0915 and 1015 UTC) captured the sudden onset of the strongest winds (Figure 3.12). Note the eddy-like structure of the wind field around the prominence in the Wasatch Front, where the wind is northwesterly. Peak winds were observed at the western mouth of the Weber River Canyon and extended up-canyon past PWR; thereafter, winds dropped off substantially during travel farther east up the canyon. Union Pacific Railroad halted all train traffic at the eastern mouth of Weber Canyon, the end of the mobile-sensor transects in Figure 3.12. Temperature and pressure observations collected by the vehicle-mounted sensors exhibited near-uniform potential temperature at the base of the Wasatch Front; lower potential temperatures in the Weber River Canyon indicated the contribution of thermally-driven canyon flows to wind speed in this area (not shown).

An additional asset available to examine the vertical structure of the near-surface flows during this windstorm was a 50-m tower located at the mouth of Weber River Canyon (Chrust et al. 2013). This tower was installed to evaluate the wind energy potential from the frequent persistent nocturnal thermally-driven flows found at this valley exit-jet location. As shown in Figure 3.13, sensors at 3, 10, 30, and 50 m indicate that mean wind speeds generally increase with sensor height during the period of strongest winds, 1100–1900 UTC. However, due to the turbulent nature of the combined exit and downslope flows, wind gusts are roughly equivalent in the 10–50 m range; notably, 3-m wind gusts are occasionally as

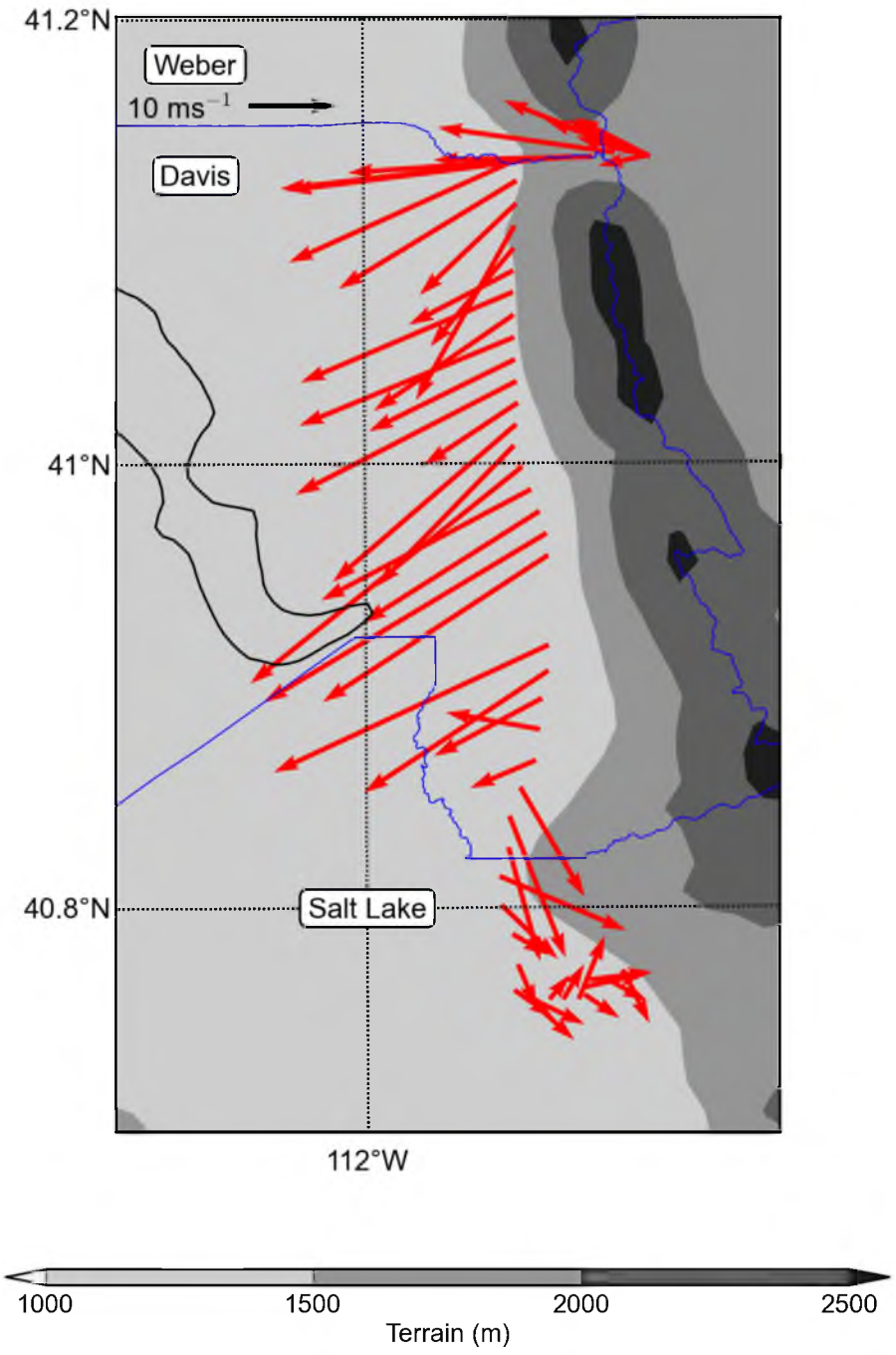

Figure 3.12: Vehicle-mounted weather station data collected 0915–1015 UTC. Vector arrows are relative to scale in top-left. Filled contours indicate terrain.

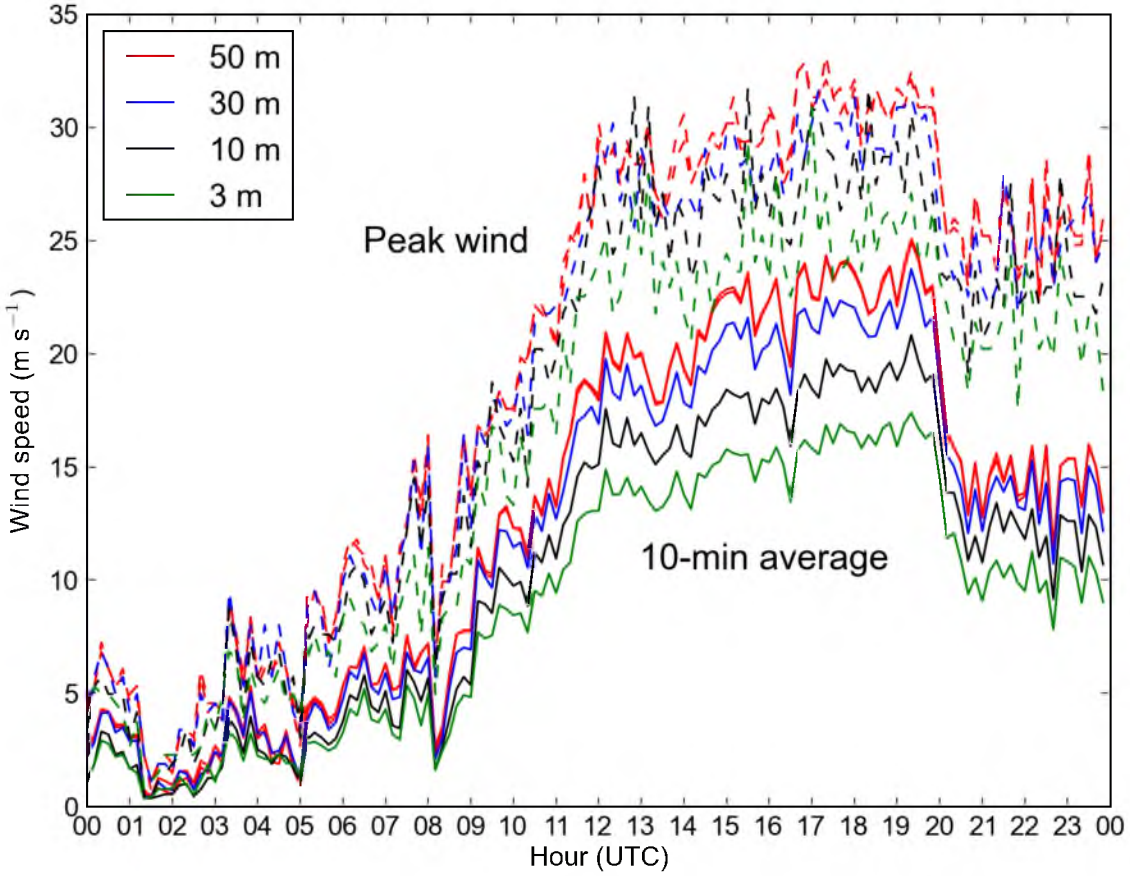

Figure 3.13: 50-m tower observations of wind speed as a function of sensor elevation above ground level at the mouth of Weber Canyon, 1 December 2011.

strong as those much further aloft.

Vertical profiles of wind, temperature, and moisture, collected by rawinsondes launched twice-daily at KSLC during prior windstorms, have exhibited primarily the prevailing synoptic flow combined with complex downstream effects of the flow over the Wasatch Range. Figure 3.14 shows the KSLC sounding launched at ~1100 UTC with a nominal observation time of 1200 UTC. The profile recalls those typically observed at KSLC during a Wasatch windstorm: (1) no indication of downslope winds near the surface (i.e., low-level southerly drainage flow down the Salt Lake Valley towards the Great Salt Lake); (2) strong easterly winds below and extending above crest level (700 hPa); (3) easterly winds weakening aloft with limited cross-barrier flow at 500 hPa; (4) relatively-low dewpoint temperatures throughout the profile; (5) a small surface-based inversion with a well-mixed layer extending upwards to ~750 hPa; (6) evidence of strong turbulence between 750 and 700 hPa with superadiabatic lapse rates; (7) a capping inversion layer near crest (~690 hPa) with adiabatic and stable layers interspersed further aloft.

The previous day, the UoU team planned to launch rawinsondes upstream and downstream of the Wasatch at roughly the same time as the nearby NWS launch at KSLC (~1100 UTC), and then to continue operations as conditions warranted. The additional launches were intended to describe the flows upstream and immediately downstream of the terrain where the strongest winds were expected. Upstream launches at UFD06 were made at the nominal observation times of 1200, 1500, and 1800 UTC (i.e., balloons released at 1100, 1400, and 1700 UTC, respectively). Since short-period communication failures between the radio base station and the 1200 and 1500 UTC sondes at UFD06 created small data gaps of 25–75 hPa in depth, the 1800 UTC profile is shown in Figure 3.15a. The automated algorithms provided by the rawinsonde manufacturer tend to smooth excessively the wind observations, hence the following figures use raw, unsmoothed wind data. At UFD06, the lowest 750 m is well-mixed and nearly adiabatic, below a series of increasingly-stable layers through to 5 km. A particularly strong inversion at ~3250 m, an elevation roughly 500 m above the crest of the Wasatch in this area, caps a layer with higher relative humidity and the strongest easterly winds (~30 m s^{-1}) observed at this time. Above the highest inversion, winds are substantively weaker, and relative humidity is lower. Notably, easterly winds are observed throughout the profile (not shown), in contrast to wind reversals at

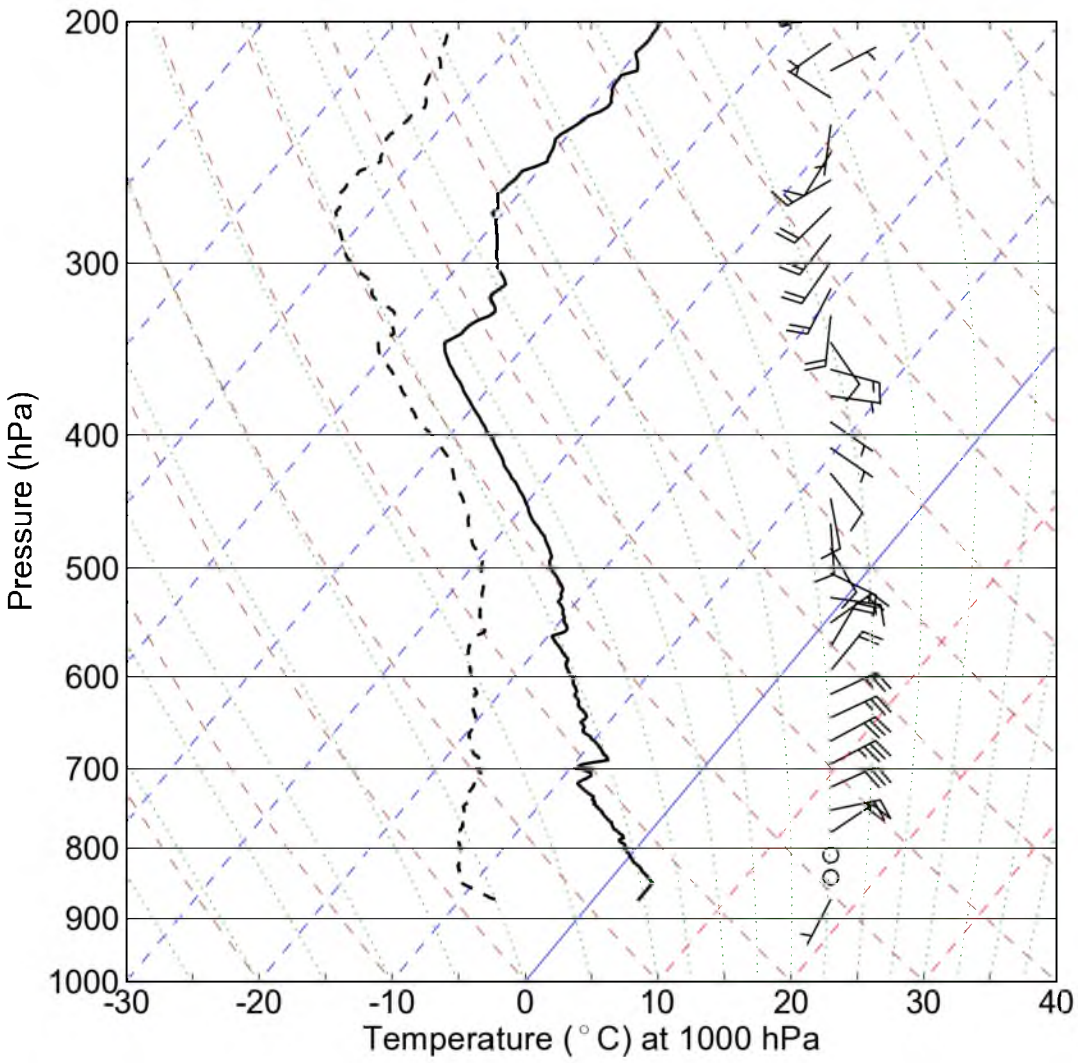

Figure 3.14: Skew-T log-P diagram for 1200 UTC 1 December 2011 at Salt Lake City. Wind speed is plotted in standard convention (barbs are 5 m s^{-1}). Dry-bulb and dewpoint temperatures are solid and dotted lines, respectively.

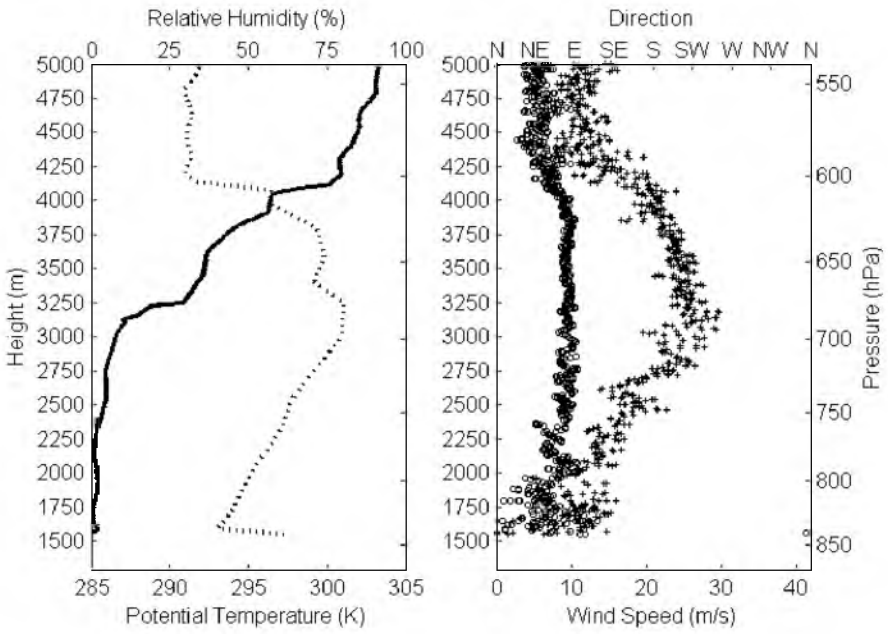

(a)

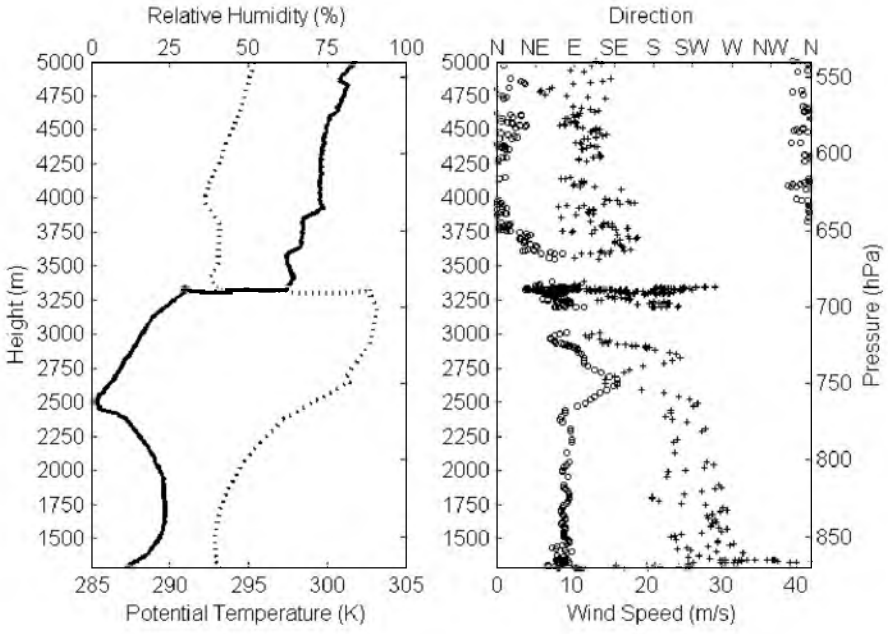

(b)

Figure 3.15: Vertical profiles at Morgan, UT, and Centerville, UT. (a) Potential temperature (solid line), relative humidity (dashed line), wind speed (crosses), and wind direction (open circles) at Morgan, UT (UFD06) at 1800 UTC 1 December 2011 as a function of height. (b) As in (a) except for Centerville, UT at 1200 UTC.

Centerville (discussed below).

The UoU team selected a park in Centerville, UT for a lee-side rawinsonde launch. Ultimately, its position was within the core of strongest wind observed during the event, immediately upwind (~200 m) of the UDOT tower (CEN) and UPR tower (CENWWS), themselves immediately west of the Interstate 15 freeway (see Figure 1.3). Sound-barrier walls east of the freeway bracket the park on its north and south edges and contributed to flow channeling. Several trucks tipped over as they passed northward from the protection of the sound barrier into the unprotected zone on both the freeway and adjacent frontage road. It was under these extremely harsh conditions that the UoU team successfully launch a rawinsonde at 1100 UTC at the park. The balloon initially travelled nearly horizontally towards the freeway, before gaining altitude and clearing trees located at the edge of the frontage road. A later (~1400 UTC) rawinsonde launch from a safer location in Centerville was unsuccessful due to a communication failure between the rawinsonde and radio base station. Vertical profiles of potential temperature, relative humidity, and wind speed and direction from the 1200 UTC Centerville sounding are shown in Figure 3.15b. Two small communication gaps occurred during the ascent: one at 3050–3200 m, and another at 3400–3500 m. The surface layer (lowest 50–60 m) is characterized by lower potential temperature and horizontal winds approaching 40 m s^{-1}, consistent with the nearby surface wind-gust observations of ~36 m s^{-1} at CENWWS at this time. Following Armi and Mayr (2011), this layer is referred to as the "downslope underflow".

A knife-edge inversion (5.7 °C increase in ~3.5 hPa) at 3300 m caps a turbulent layer containing adiabatic, superadiabatic, and weakly stable sublayers between 1700 m and 3300 m. Relative humidity increases to 90% through this depth and falls sharply through the inversion. Winds again increase to over 30 m s^{-1} in the inversion layer, and rotate above the inversion to sharply-reduced cross-barrier flow above 3750 m. This rotation is not evident upstream at UFD06, and may therefore be self-induced. The knife-edge inversion is consistent with the presence of an internal hydraulic jump comprising a moist layer below and dry air above (Armi and Mayr 2011). Hence, there appears to be strong flow separation as the air crosses the Wasatch; the downslope underflow descends steeply along the slope, while another strong easterly current flows outward near crest level (~3300 m). All three sondes at UFD06 detected the strongest winds (25–30 m s^{-1}) at 3100–3200 m, consistent

with the strong crest-level winds observed near the inversion layer above Centerville.

Figure 3.16 contrasts the ascent rates at ~1–2-s intervals of the UFD06 and Centerville rawinsondes. The ascent rate at UFD06, averaged from surface to 3300 m, is 4.8 m s^{-1}, which is roughly the rate expected given the amount of helium used in the balloon (e.g., the 1200 and 1500 UTC sondes had average ascent rates of 4.5 and 5.3 m s^{-1}, respectively). The Centerville rawinsonde, using roughly the same volume of helium, experienced vastly different conditions from the UFD06 launch. Consistent with visual tracking of the sonde until lost in the dark, the buoyancy imparted by the helium was initially negated by descending motions, resulting in a near-horizontal trajectory. Then, the rawinsonde ascended at an increasingly-rapid rate, approaching 25 m s^{-1} through the superadiabatic layer. Vertical speeds then decreased through to 2900 m. At first, the balloon made no headway vertically through the knife-edge inversion, and at times descended in that layer, which led to a large number of observations in this vicinity. Once clear of this layer, the balloon ascended at an average rate of 4.6 m s^{-1}. Subtracting 4–5 m s^{-1} from the observed ascent rate yields a crude estimate of peak vertical velocities O(20 m s^{-1}) upwards and O(7.5 m s^{-1}) downwards.

Violent ascent and descent of the balloon is consistent with visual evidence after sunrise of rotors (low-level vortices with horizontal axes parallel to the ridgeline in the lee of mountain ranges, Doyle and Durran 2002). As shown in the satellite image and photograph in Figures 3.17 and 3.18, respectively, an upstream cloud deck over the Wasatch evaporates in the air descending down the lee slope, with distinctive jump (rotor) clouds west of the slope base. The quasi-uniform horizontal distance from the crest to the jump clouds is ~10 km (3–5 km from the mountain base). The superadiabatic lapse rate in the layer 2000–2500 m may result from the formation of jump clouds and subsequent evaporative cooling of the air when the clouds dissipate. Aircraft, dropsonde, and lidar observations from the Terrain-Induced Rotor Experiment (T-REX) provide more comprehensive depictions of turbulence and rotors in the lee of the Sierra Mountains during downslope windstorms (Armi and Mayr 2011; Kühnlein et al. 2013) that build on glider observations of 10-m s^{-1} ascents during the Sierra Rotor Experiment in the 1950s. For example, aircraft and lidar observations during T-REX detected vertical velocities >10–15 m s^{-1} in the ascending air beneath jump clouds.

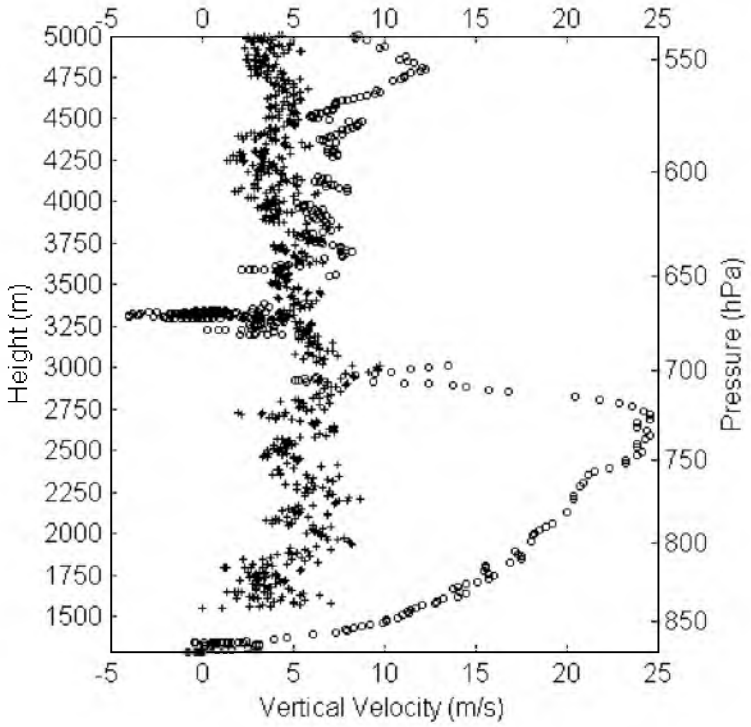

Figure 3.16: Comparison of rawinsonde ascent rates ($m\,s^{-1}$) at Morgan, UT (UFD06; 1800 UTC; crosses) and Centerville (1200 UTC; open circles).

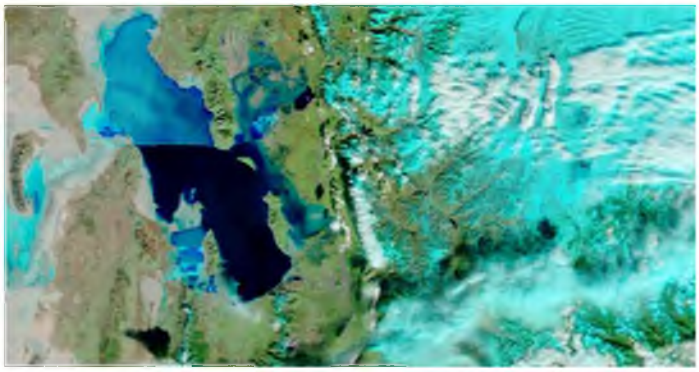

Figure 3.17: Terra satellite image at 1840 UTC 1 December 2011 at 250 m resolution, showing the upstream cloud deck over the crest of the Wasatch Mountains and rotor clouds downnstream.

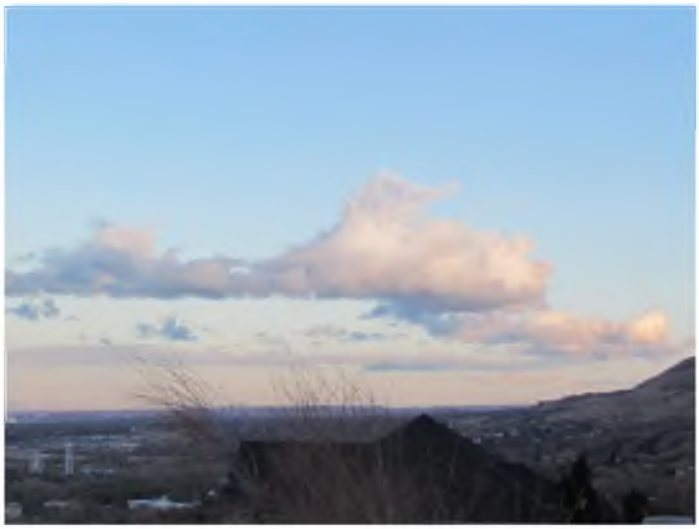

Figure 3.18: Rotor clouds as seen from north of Centerville, UT, looking south, at 1500 UTC. (Photo: John Horel)

CHAPTER 4

SENSITIVITY AND PREDICTABILITY

4.1 WRF-model simulation with NAM initial and boundary conditions (NAM Control)

As introduced in Chapter 2, a numerical simulation was performed with the WRF model initialized from the NAM-model analysis at 0600 UTC 29 November 2011, and forced thereafter on the outermost boundary by NAM analyses updated every 6 h. This configuration is hereby referred to as the *NAM Control* simulation. The model simulation is initialized far enough in advance for mesoscale circulations to develop freely, and continues for 72 h to encompass the entire downslope windstorm event. The simulated 700-hPa geopotential height fields for 0000–1800 UTC 1 December (42–60 h into the simulation) are shown in Figure 4.1, taken from the largest (12-km) domain. The model captures the synoptic-scale structure of this ARWB event, with ridging developing and extending southwestward from northern Idaho into Wyoming, while the cut-off low becomes centered near the southern tip of Nevada. Relative to the 700-hPa circulation depicted in the ERA-Interim reanalyses (Figure 3.3), values of geopotential height simulated by the model are elevated by ~60 m everywhere, but the modeled height gradients are similar to those analyzed, particularly in the vicinity of the Wasatch Front. However, the model simulation is slower in its development of the ARWB event, with the cut-off low-height center deepening through 1800 UTC.

Observed surface wind speeds near the Wasatch Front at 1200 UTC and 2100 UTC are superimposed on the surface wind fields simulated by the model in Figure 4.2. The simulated winds are comparable to those observed near the base of the lee slopes of the Wasatch Mountains at 1200ÜTC, including the localized maximum in Davis County near Centerville. By later in the day (2100 UTC), the model has shifted the strongest winds further north, but the winds in Davis County are overdone. The winds along the crest

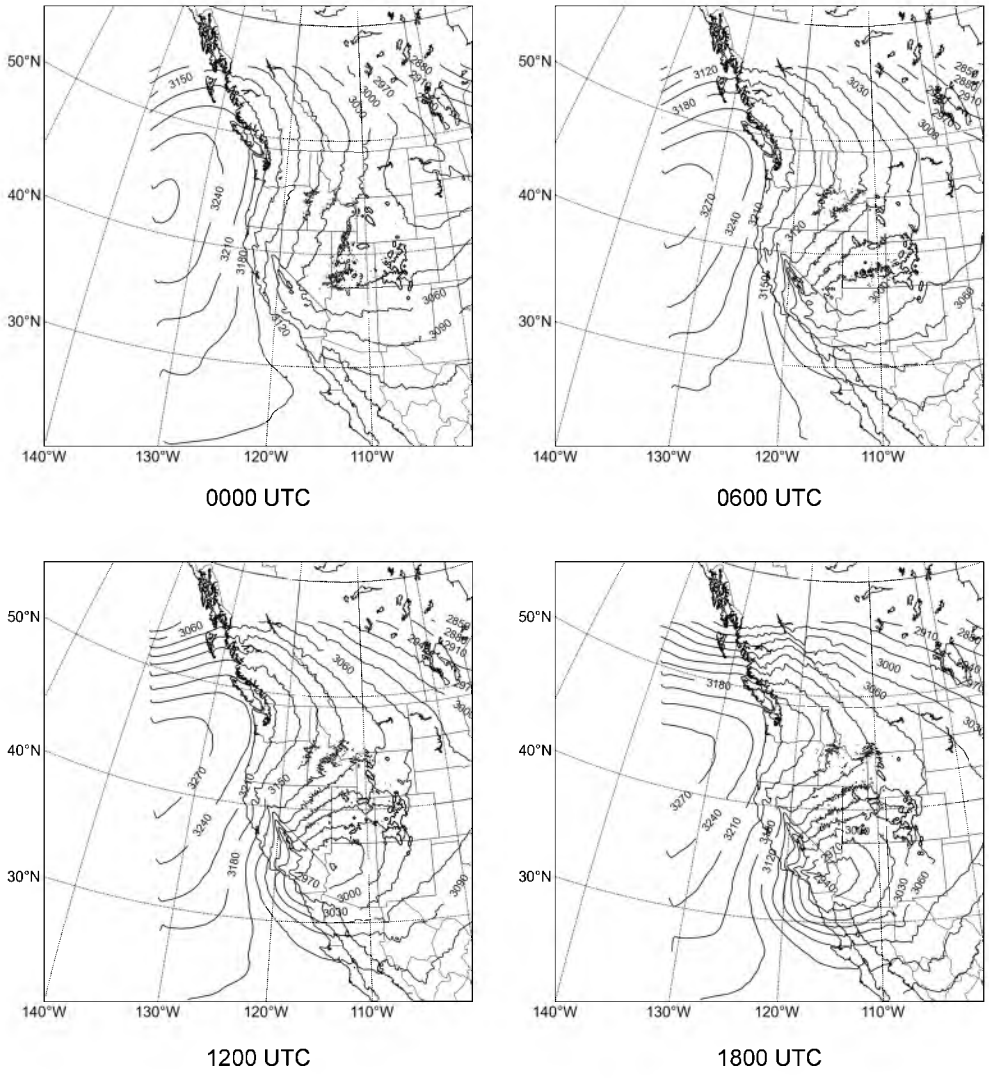

Figure 4.1: NAM-Control 700-hPa geopotential-height field (contoured at 30-m interval), every 6 h between 0000 and 1800 UTC 1 December 2011. Noisy contours result from the 700-hPa surface intersecting the model terrain.

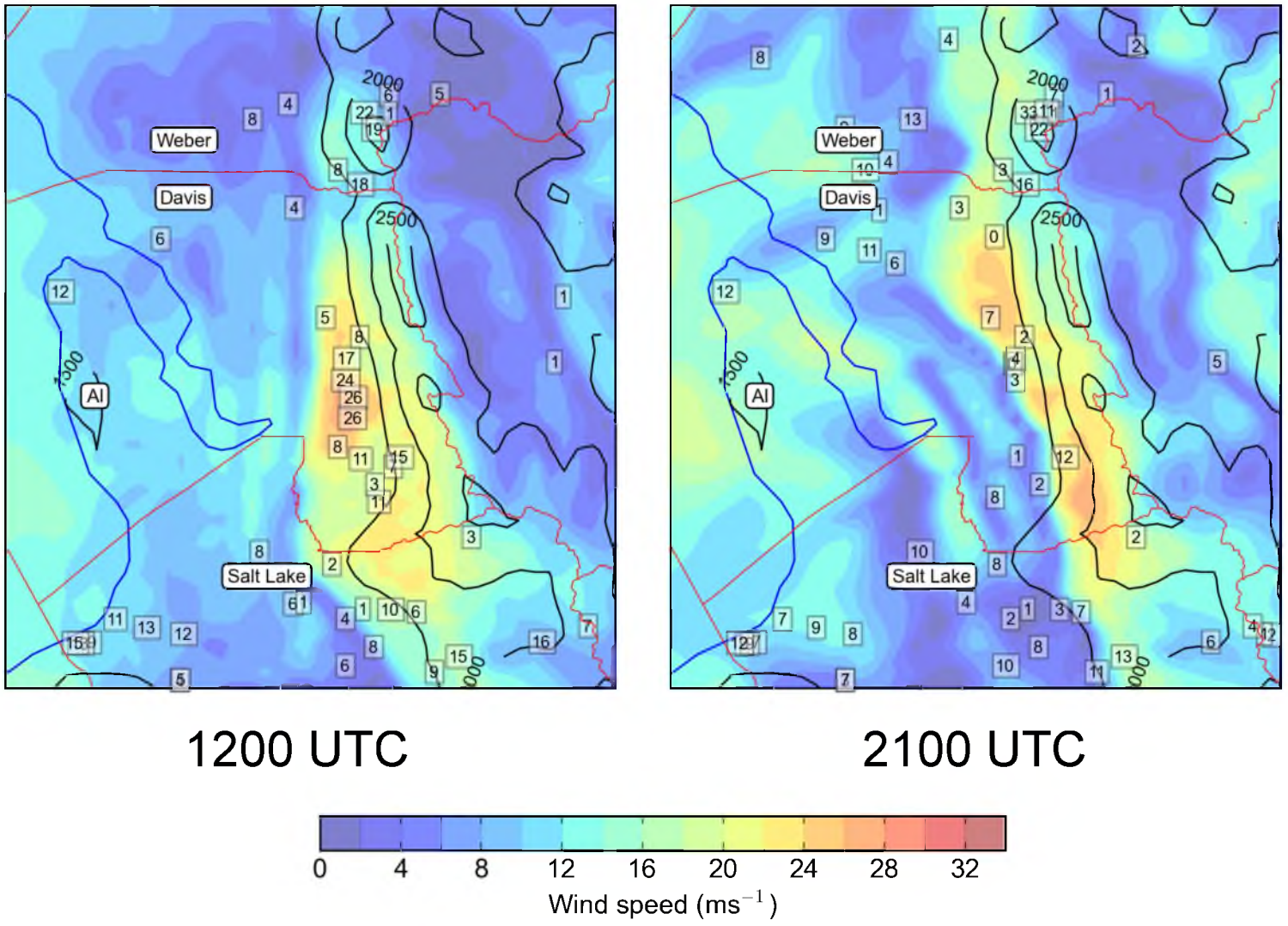

Figure 4.2: Comparison of observed surface wind speeds (boxed numbers) versus model surface wind speeds (shading according to scale at bottom) on 1 December 2011 at 1200 and 2100 UTC. Terrain is contoured every 500 m for guidance. Counties are labeled and their boundaries are drawn in red. Great Salt Lake drawn in blue.

in the model are lower than those observed; for example, simulated wind speeds were 10–15 m s^{-1}, while the winds observed at OGP and the crest-level station at Snowbasin Ski Resort were greater than 20 m s^{-1} (Figure 3.8c). As will be shown in greater detail later, the model tends to accelerate the flow down the slopes of the Wasatch Mountains more strongly than is likely taking place. The WRF model develops rotors/trapped waves and these phenomena appear in the valley surface winds at 2100 UTC as bands of increased and decreased winds in corn row patterns oriented parallel to the upstream terrain. In this 1.3-km domain simulation, strong winds do not extend out over the Great Salt Lake, whereas operational NWS 4-km WRF model forecasts (not shown) suggested a westward extension of 25–30 m s^{-1} gusts as far west as Antelope Island (point AI in Figure 4.2).

The time evolution of the simulated downslope windstorm is now related to that observed near UFD04 in Bountiful (near the location of strongest observed wind speeds). The NAM Control simulation shows remarkable agreement with the observations regarding the timing and general evolution of the intensity of the surface winds (Figure 4.3). However, the NAM-Control simulated windstorm continues for around 2 h longer than that observed.

The vertical profiles of temperature, moisture, and wind at KSLC at 1200 UTC from the NAM-Control simulation, presented in Figure 4.4, are contrasted to those observed and shown previously in Figure 3.14. The model captures the basic vertical structure, but the simulated vertical profiles differ from those observed in several key respects: (1) surface westerly return flow rather than decoupled down-valley winds; (2) peak easterly flow near the base of a stable layer at 775 hPa relative to that observed near 700 hPa; (3) deep well-mixed layer between 750–550 hPa with near-zero cross-barrier flow at 600 hPa, in contrast to more stable conditions and weak cross-barrier flow observed above ~475 hPa; and (4) generally lower dewpoint temperature throughout the troposphere.

The NAM-Control vertical profiles taken at 1200 UTC of potential temperature, relative humidity, and wind speed and direction across the Wasatch Mountains are shown in Figures 4.5–4.8; these are contrasted with the profiles observed upstream and downstream of the Wasatch, at UFD06 and Centerville, respectively (Figure 3.15). We can trace the likely westward path of unsaturated fluid parcels traveling in the core of the easterly jet assuming they experience adiabatic motion. The simulated easterly winds peak near 730 hPa (~286 K) near UFD06, with acceleration and ascent to 720 hPa of the wind speed

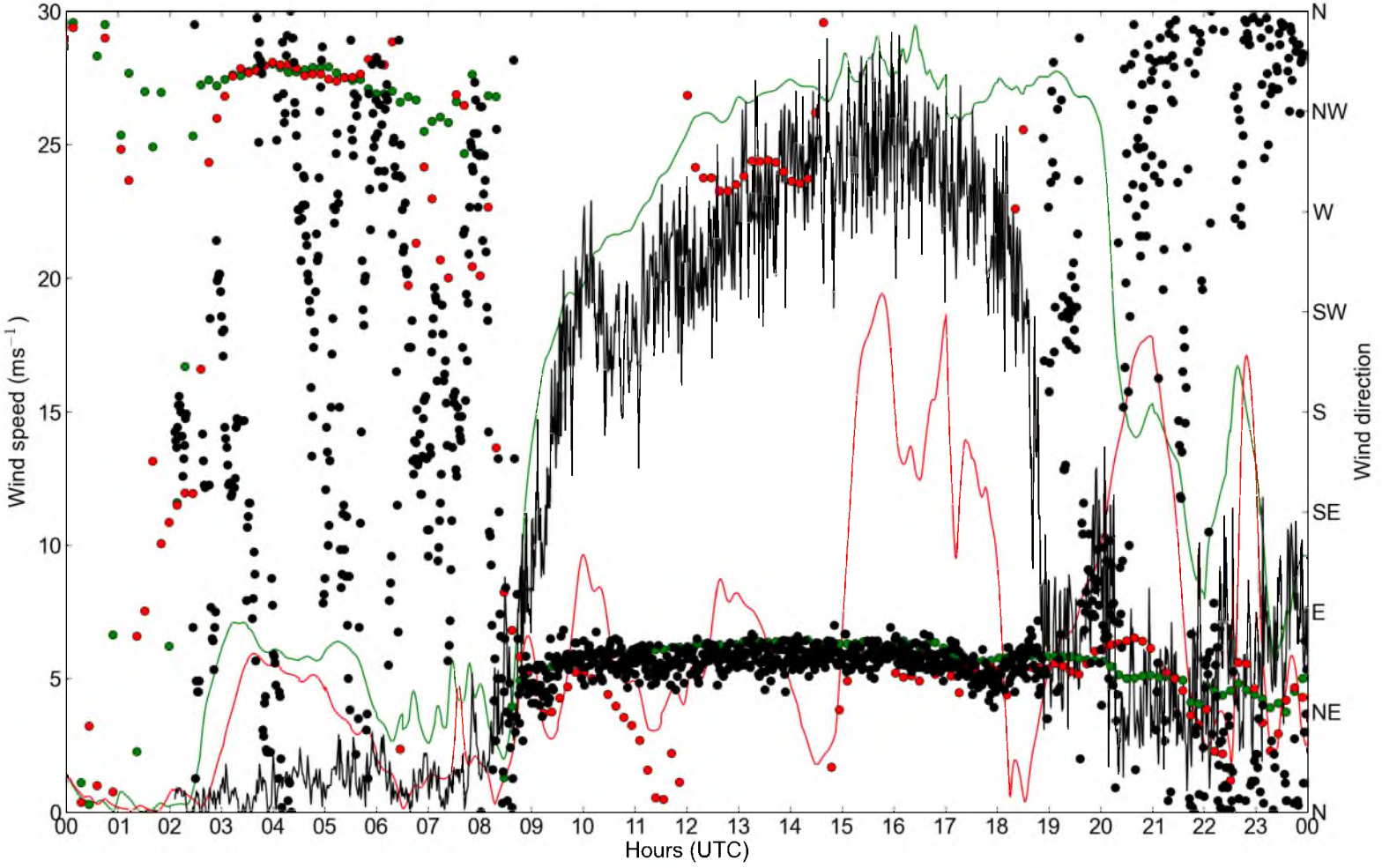

Figure 4.3: Observed and simulated surface winds in Glover's Lane, Bountiful, UT on 1 December 2011. Observed wind speeds and wind directions from UFD04 are denoted by black solid lines and filled circles, respectively. Simulated surface wind speeds and directions from the NAM Control (NAM no-Uinta) are shown by the green (red) solid lines and filled circles, respectively.

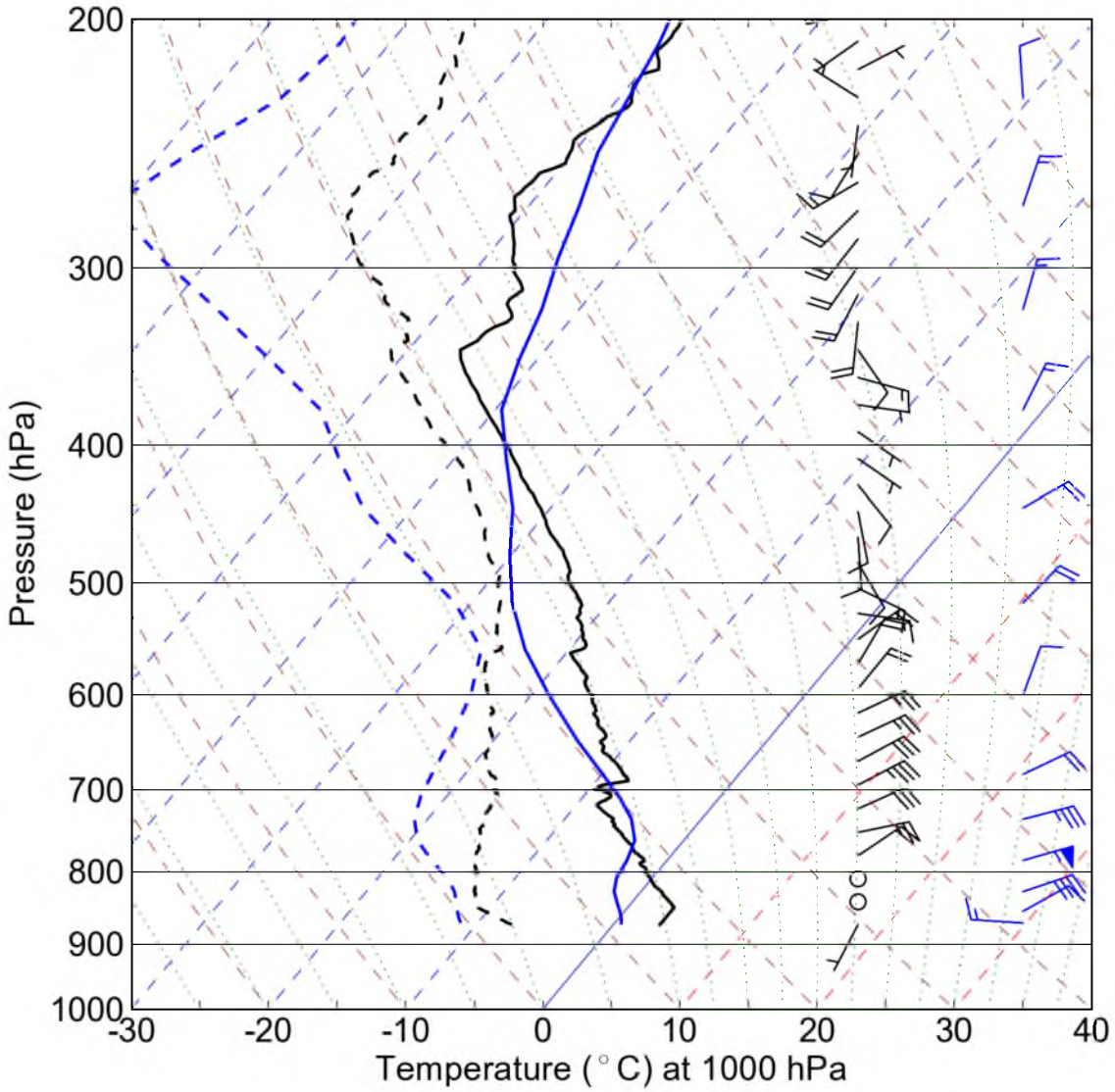

Figure 4.4: NAM-Control Skew-T log-P diagram of dry-bulb temperature (blue solid line), dewpoint temperature (blue dashed line), and wind (blue barbs; full barb 5 m s^{-1}) at KSLC for 1200 UTC 1 December 2011. Contrast with observed data (in black; same legend as Figure 3.14).

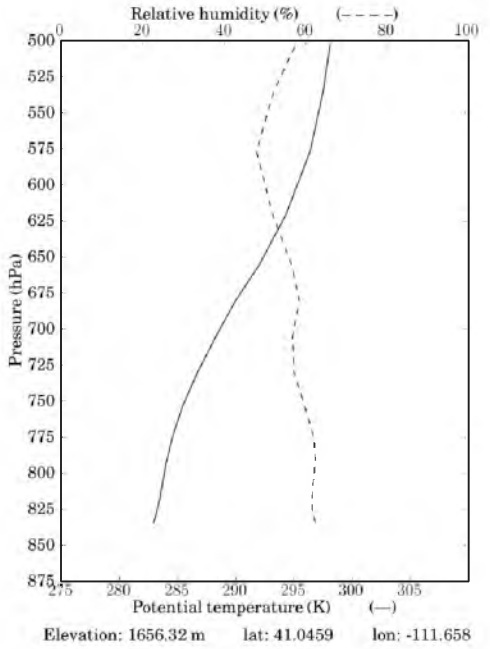

(a)

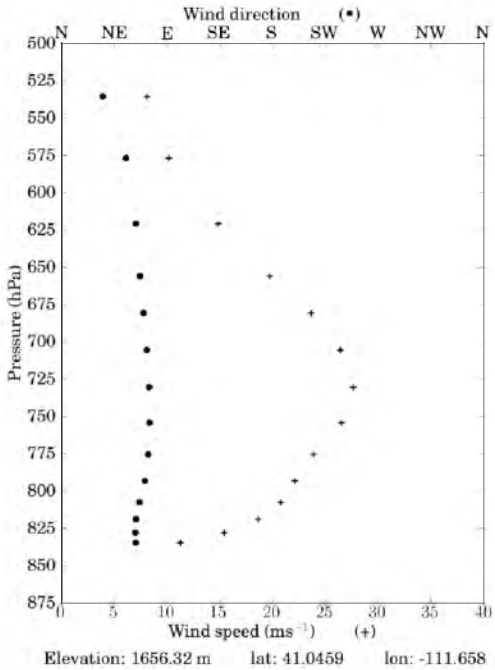

(b)

Figure 4.5: NAM-Control profiles at Morgan, UT, of (a) potential temperature and relative humidity, and (b) wind speed and direction, at 1200 UTC 1 December 2011.

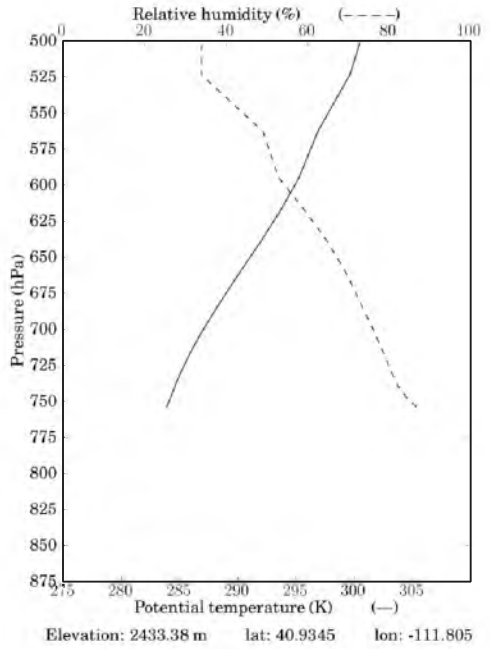

(a)

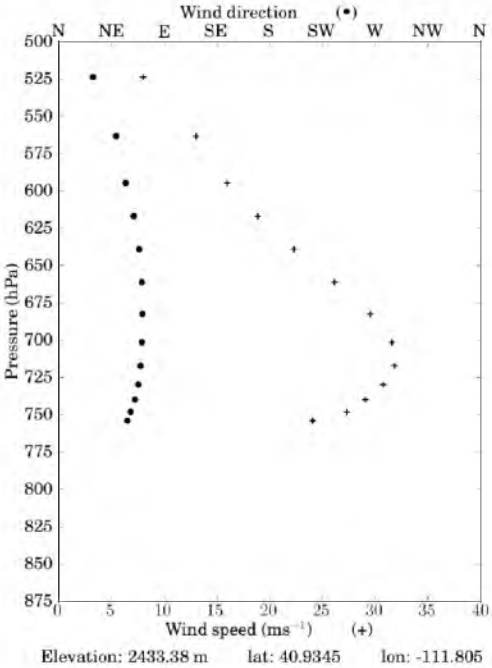

(b)

Figure 4.6: As in Figure 4.5, but at crest level east of Centerville, UT.

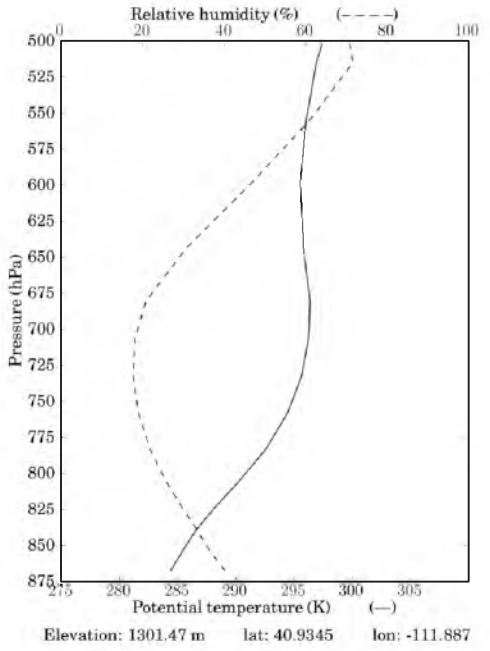

(a)

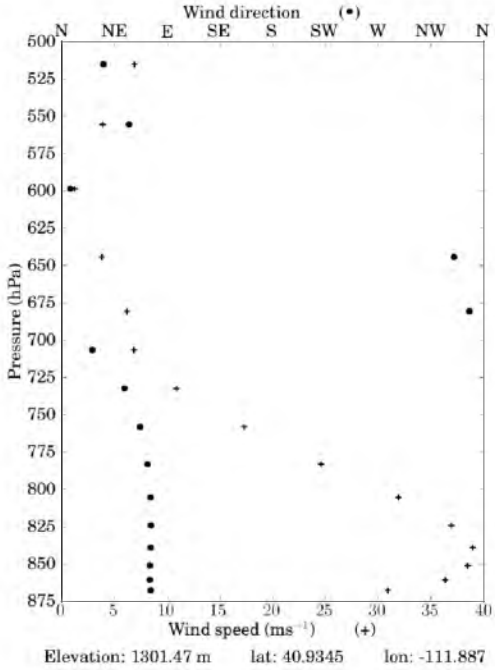

(b)

Figure 4.7: As in Figure 4.5, but at Centerville, UT.

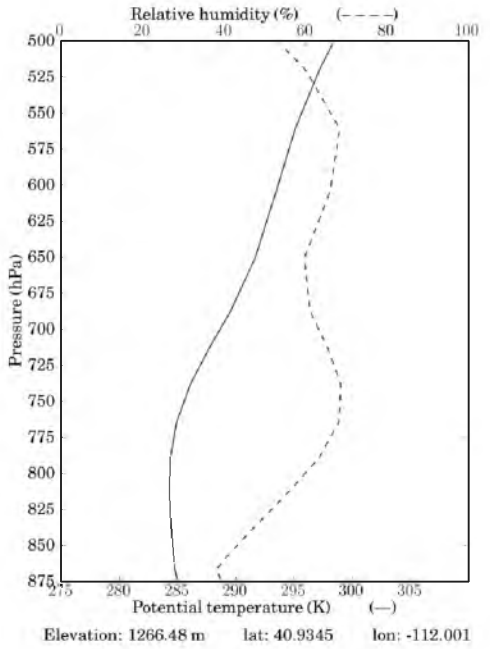

(a)

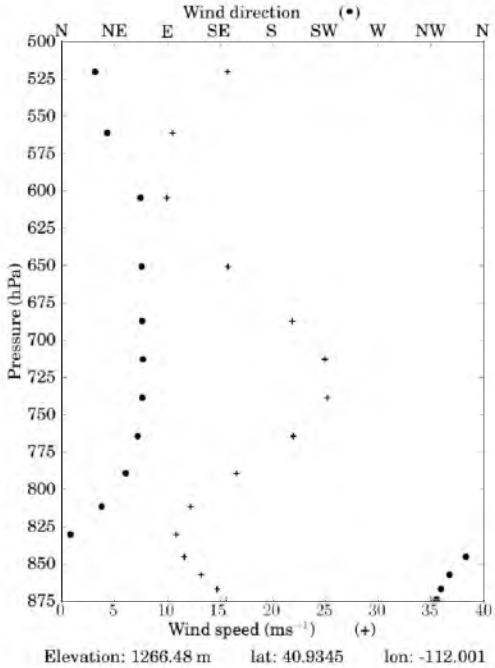

(b)

Figure 4.8: As in Figure 4.5, but 10 km west of Centerville, UT.

maximum as the jet crosses the Wasatch. The simulated flow then plunges and accelerates down the slope past Centerville. The wind speeds reach their peak at Centerville near 835 hPa and exhibit the same potential temperature (286 K) as that of the jet above UFD06. Similarly to observed data, winds rotate counterclockwise of north, and speeds reduce to near zero, at 600–650 hPa. This critical layer is not evident upstream at UFD06, and may be self-induced. Further west of Centerville, a surface return flow is evident with an adiabatic layer below 800 hPa. The peak easterly winds lift to 740 hPa, which is also the height of the 286 K isentropic surface associated with the simulated jet core. Relative to the observed profiles, the model atmosphere tends to be drier and cooler.

An advantage of the model simulations is the ability to create spatially- and temporally-superior cross-sections of potential temperature and horizontal wind relative to the small sample of soundings available for this study. We first present one cross-section along the southwest–northeast transect (A–B) shown in Figure 1.1 from the Great Salt Lake, through Centerville, to Lyman, WY (Figure 4.9). The zonal and meridional wind components from the WRF model, u and v, are rotated $\sim 20^{\circ}$ counterclockwise to create plane-parallel winds at all levels. Note that the terrain height is lower in the model than that observed. For example, the actual level of the Great Salt Lake is $\sim$1280 m, but 1260 m in model data. This discrepency across the 1.3-km domain appears to arise from multiple smoothing processing scripts within the WRF Processing System (despite 30-s resolution elevation data input), and its apparent use of surface elevation under the Great Salt Lake, rather than the elevation of the lake's surface. More importantly, the model's Wasatch Range is smoothed such that it is $\sim$250 m lower than the actual terrain.

At 1200 UTC, in Figure 4.9, 20 m s^{-1} flow from the northeast (right to left in the figure) approaches the Wasatch Front, and then plunges sharply into the valley as a downslope windstorm. Note how the colder air (lower potential temperature) pools in the upstream valley, effectively creating an unobstructed horizontal pathway for the low-level easterly jet. Downstream of the Wasatch crest, strong winds continue for less than 10 km along the valley floor before forming a hydraulic jump. In doing so, some kinetic energy is converted to potential energy, evidenced by lower wind speeds west of the jump. Under this first rotor, 5–10 m s^{-1} westerly wind oppose the windstorm easterlies. This hydraulic jump is broader than observed, i.e., observations suggest the rotor clouds and return flow begin

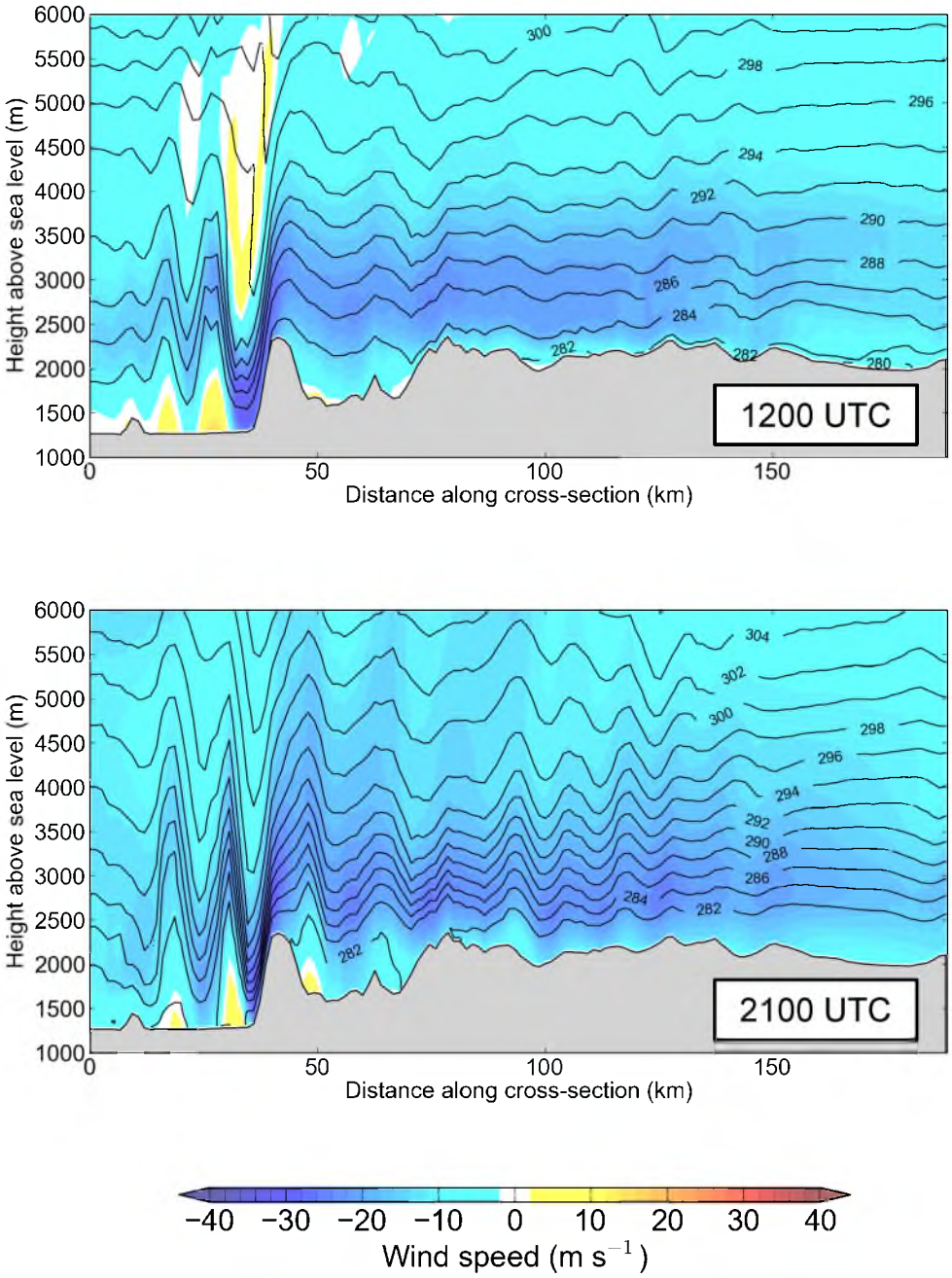

Figure 4.9: West–east (A–B) cross-section from 1.3-km NAM-Control domain as shown in Figure 1.1 at 1200 UTC (top) and 2100 UTC (bottom), 1 December 2011. Shading denotes plane-parallel wind component according to the scale, while potential temperature is contoured at an interval of 2 K.

roughly 10 km from the crest while the model shifts that farther west (see also Figure 4.8). Later, at 2100 UTC, the upstream stable layer has intensified as a result of both terresterial heating and continued cold advection in the planetary boundary layer at ~3000 m. This enhances the formation of mountain waves above the upstream terrain. The hydraulic jump at this time occurs closer to the crest, though it is important to note that these images are merely snapshots; the locations of the hydraulic jump and mountain waves shift with time as a result of dynamical and turbulent processes (e.g., Hertenstein 2009).

As seen in the Skew-T diagram for KSLC and vertical profiles across the Wasatch in Figures 4.4–4.8, the model's upstream winds tend to be at a lower height over the terrain than observed. This may explain the model's tendency to confine flow to follow the terrain slope more closely than observed, i.e., the elevated flow extending westward away from the crest in the observed internal hydraulic jump zone is missing from the model. Note also that the winds immediately above the Wasatch crest are weak (see also Figure 4.2), which contributes to flow not being able to travel laterally away from the crest but rather obtains a steeper angle of descent associated with the lee waves. The model also does not capture the strong capping inversion above the rotor observed near Centerville.

Cross-sections of vertical motion are shown in Figure 4.10 along the same transect (A–B) and at the same times as those for along-section wind. At 1200 UTC, ascent within the hydraulic jump is computed as 20–30 m s^{-1}, which is broadly consistent with the ascent rate estimated from Centerville rawinsonde at this time. However, the overall structure of the simulated downslope windstorm may be too intense, relative to that inferred from the Centerville sounding and other observational evidence. The strong subsidence, 2-km plunging of the isentropes, and extreme drying in the lee of the mountains is not likely to have taken place during this event, and is instead reminiscent of the strongest downslope wind storms experienced in the Boulder, CO area (Lilly and Zipser 1972). The lee waves continue to amplify through the time of the later cross-section (2100 UTC).

Cross-sections perpendicular to the upstream flow (i.e., roughly north–south across a swath of lower terrain in Wyoming and extending into the Uinta mountains, C–D in Figure 1.1) are generated by rotating the wind components 5° counterclockwise (Figure 4.11). This slight rotation hence increases the orthogonality of the cross-section to the prevailing flow. At 1200 UTC, the simulation generates a barrier-jet core of 15–20 m s^{-1} easterly

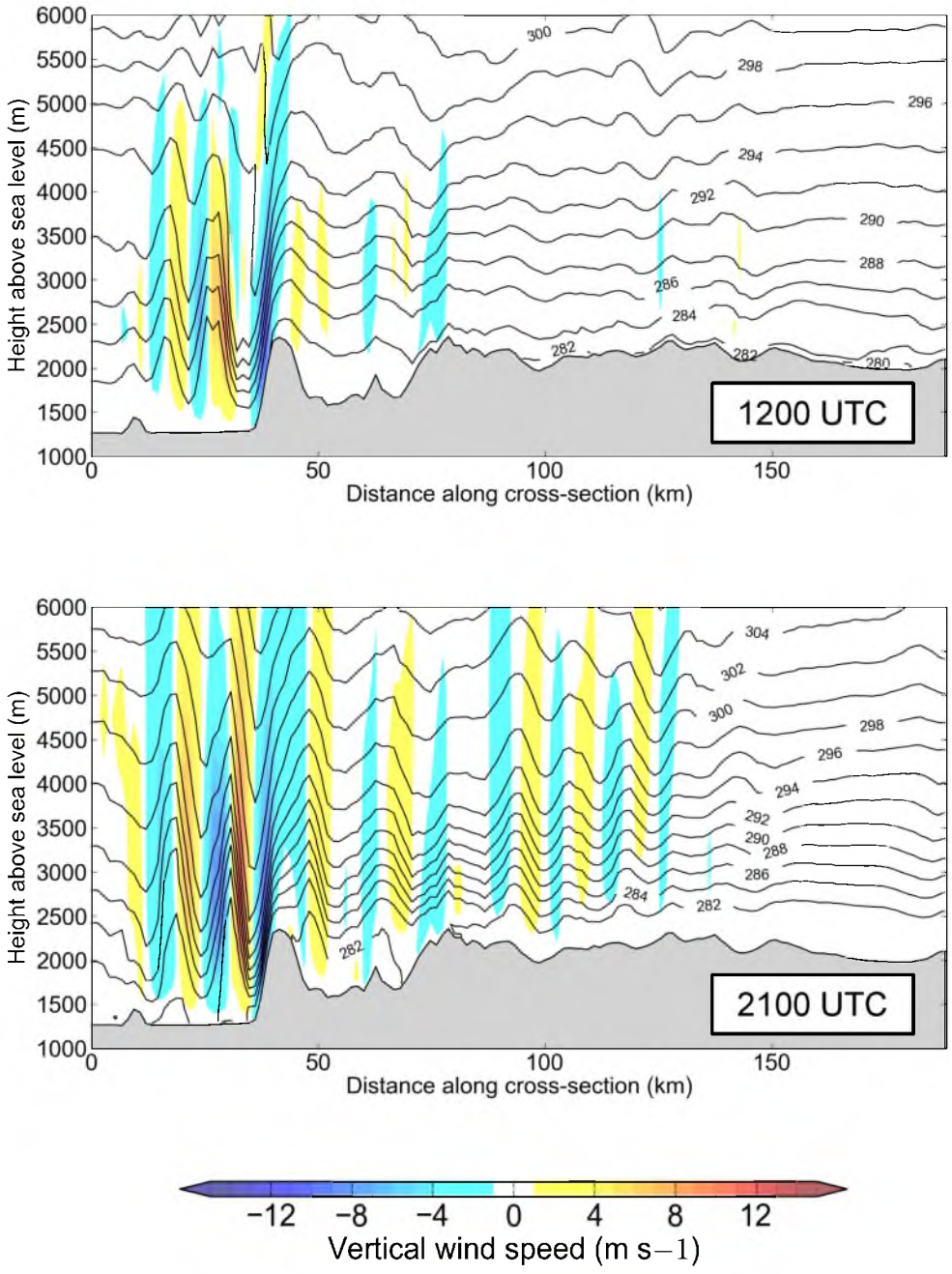

Figure 4.10: As in Figure 4.9, but the shading indicates vertical wind.

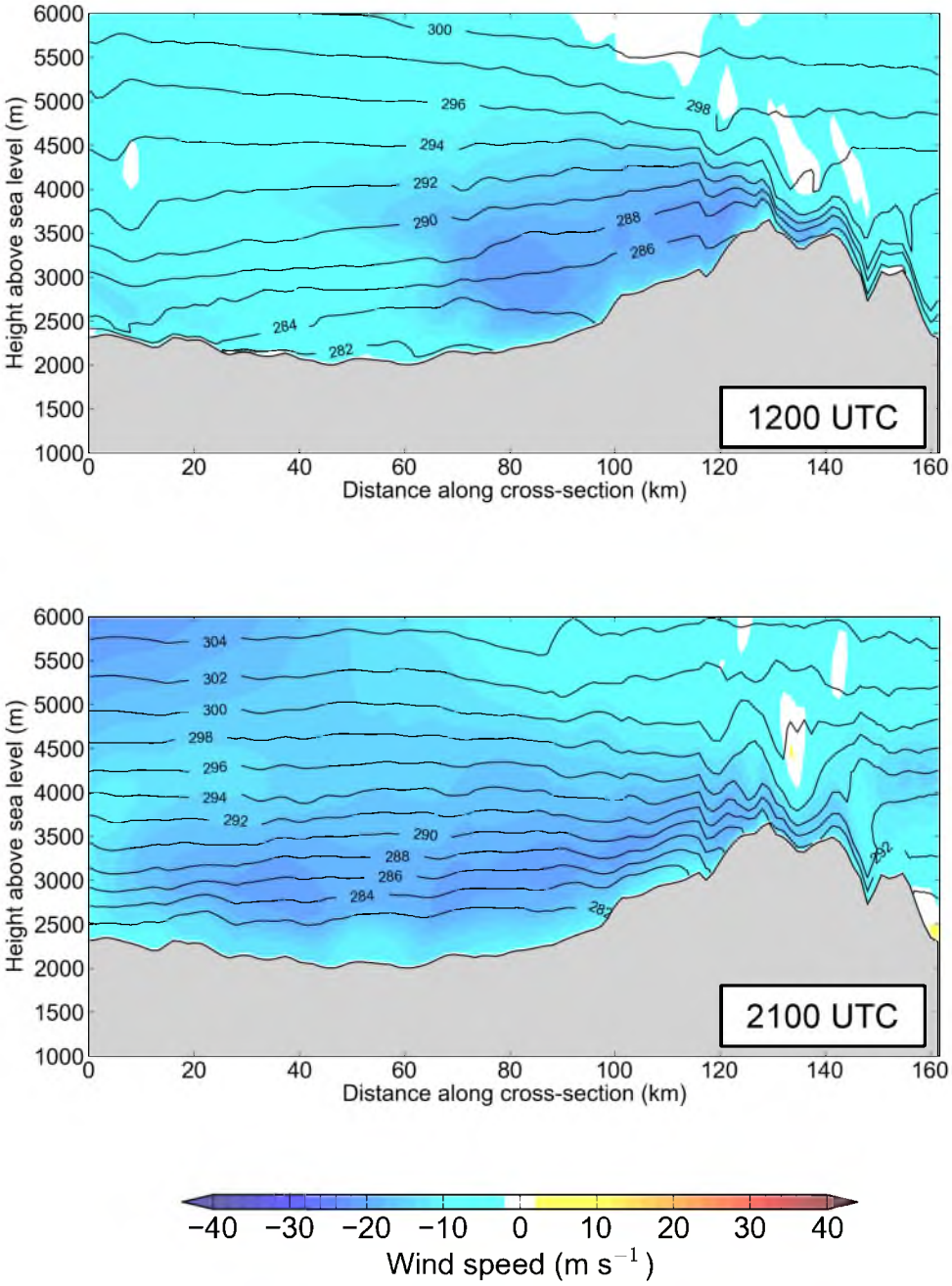

Figure 4.11: Roughly north–south (C–D) cross-section from 1.3-km NAM-Control domain through Lyman to the southern slopes of the Uintas (right edge) as shown in Figure 1.1 at 1200 UTC (top) and 2100 UTC (bottom), 1 December 2011. Shading denotes wind component out of the page (predominantly easterly) according to the scale; potential temperature is contoured at an interval of 2 K.

winds to the north of the Uinta mountains. By 2100 UTC, the strong easterly flow has extended farther north, as the cut-off low reaches a position directly south of the Wasatch Front. This may explain in part the observed northward progression of strong winds from Davis to Weber County, as a result of the more windstorm-favorable barrier-jet easterlies extending further north later in the day.

4.2 Sensitivity to Uinta Mountains

The Uinta Mountains are a substantive barrier and have the distinction of being the highest mountain range (defined as a crest line above 3000 m) in the contiguous United States oriented in the east–west direction. Their location south of the open expanses of western Wyoming (at a mean elevation of ~2000 m) may contribute to channeling easterly winds towards the Wasatch Mountains. Following similar WRF-terrain modifications by West and Steenburgh (2011), and Alcott and Steenburgh (2013), the impact of the Uinta Mountains on the 1 December 2011 Wasatch downslope windstorm is investigated by completing a simulation in which the terrain height of the Uintas above 2300 m is lowered to that elevation on the 4- and 1.3-km domains (the Uintas remain unchanged on the 12-km domain to minimize discontinuities on the largest scales). This has two additional impacts: (1) the resultant void is replaced by a volume of standard-atmosphere air, and (2) soil temperatures are replaced with the deep-soil values in places where the upper soil layers have been removed. Due to the strong dynamical forcing of this event, these two changes are unlikely to greatly affect the simulation in comparison to the changes arising from the altered terrain. The use of two-way feedback between the nested domains implies that the Uintas' presence in the outer domain may still be felt to some extent on the inner domains, i.e., the impact of their removal may be underestimated here. All other characteristics of the model simulations remain the same as that presented in the previous section. This configuration is named the *NAM no-Uinta* simulation.

Figure 4.12 shows the zonal wind difference (NAM No-uinta minus NAM Control) after reducing the height of the Uinta mountains. At 1200 UTC, there is a strong increase–decrease dipole centered near Salt Lake City downtown (marked by SLC). North of this point in Davis County, easterly winds have been markedly reduced by the removal of the Uinta Mountains (whose former location is contoured in red). The decreased easterly

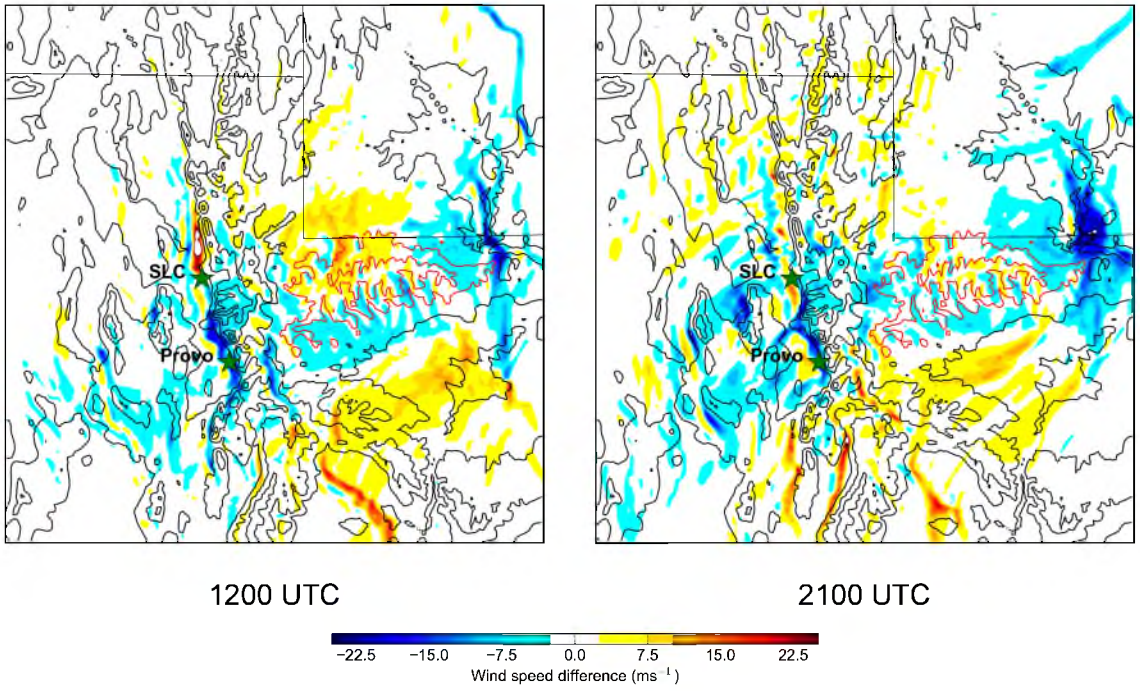

Figure 4.12: Zonal wind difference (NAM no-Uinta minus NAM Control), shaded according to the scale, at 1200 UTC (left) and 2100 UTC (right), 1 December 2011. Black (red) contours at 500-m intervals denote the elevation of the terrain used in both the Control and No-Uinta (Control only) simulations. Blue indicates an increase in easterly wind in this location as a result of removing the Uinta mountains.

flow north of the Uinta mountains' former position supports the hypothesis that the Uintas obstruct southward flow and create a barrier jet towards Davis County. Conversely, easterly winds have strengthened to the south of Salt Lake City, particularly around the city of Provo (marked), in Utah County. The north-easterly flow from Wyoming, without the Uintas, has an unimpeded route towards Utah County, and plunges over the Wasatch farther south as a downslope windstorm in that region.

Later at 2100 UTC—with or without the Uinta mountains—there are strong easterly winds in Davis County, confirming the importance of the orientation of large-scale mid-tropospheric winds; i.e., when the large-scale flow becomes more easterly, the impact of the blocking by the Uintas is lessened. The reduced elevation of the Uintas allows the windstorm to continue in Utah County at this time. Overall, an increased easterly component better initiates mountain waves along the north–south section in Salt Lake and Davis Counties, which creates damaging downslope winds. In contrast, the presence of the Uintas likely shields Utah County from damaging winds on many occasions. The time series of simulated surface wind at Centerville with (green) and without (red) the Uintas shown in Figure 4.3 corroborate the sensitivity to the orientation of the large-scale flow. Without the Uintas, the downslope easterly flow is weaker until the model's synoptic-scale flow becomes more easterly after 1500 UTC.

Cross-sections are now shown as before, but with the Uinta mountains reduced in elevation. While the stability is comparable, a weaker jet of plane-parallel wind crosses the Wasatch crest at 1200 UTC (Figure 4.13). This results in a weaker breaking mountain wave, which does not penetrate to the floor of the Wasatch Front. At 2100 UTC, wind speeds are still slightly weaker than the NAM-Control run, though strong winds now reach the valley floor. A comparison of vertical wind speed (Figure 4.14) highlights the weaker mountain wave pattern downstream of the Wasatch crest at both times. The north–south NAM No-Uinta cross-section (Figure 4.15) maintains a core of strong easterlies at 1200 UTC from the control run, though this core is more elongated than the NAM Control. The persistence of the barrier-jet-like feature, despite removal of the Uintas in the 1.3- and 4-km domains, may relate to the existence of the Uintas in the outer domain.

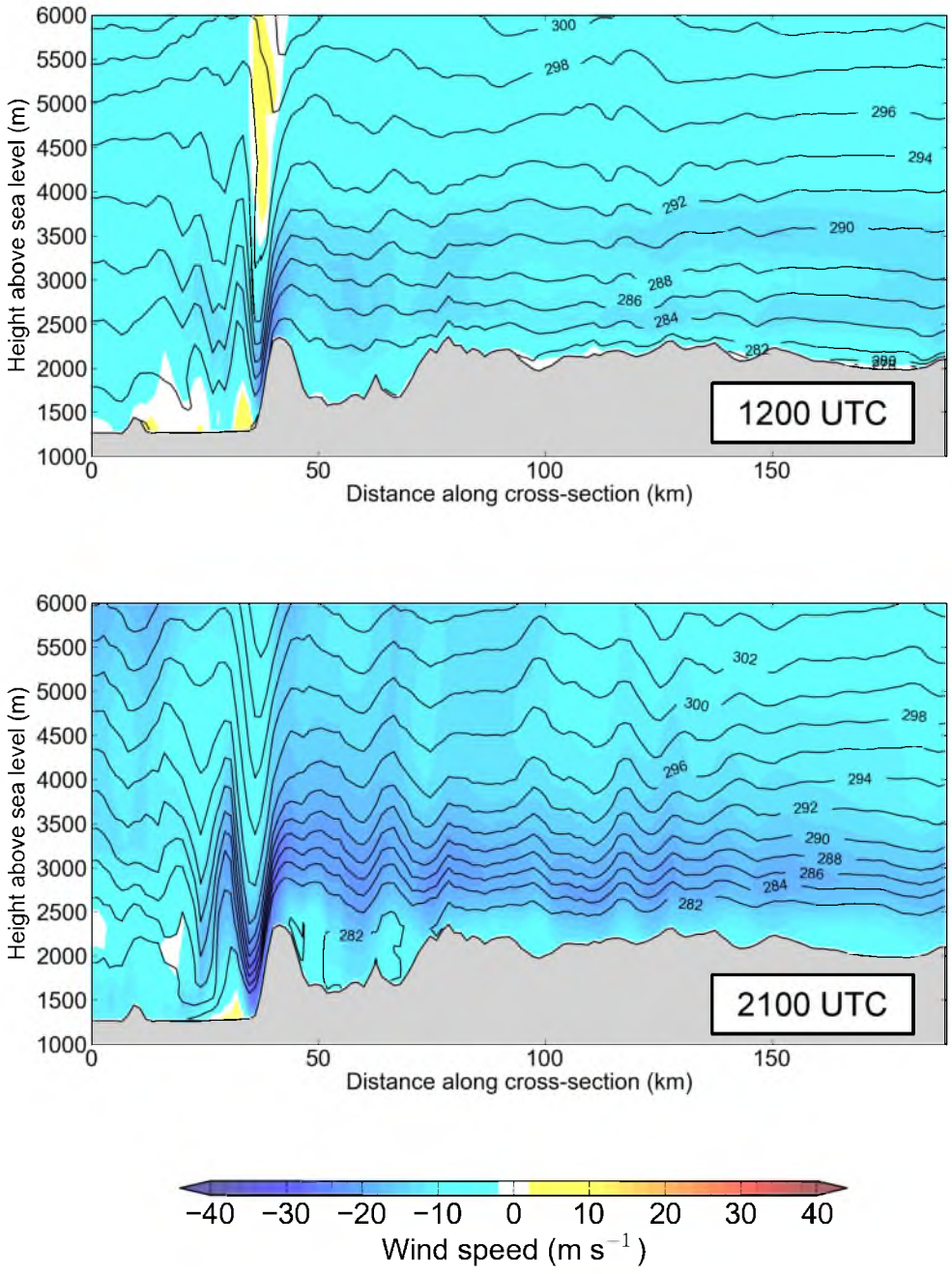

Figure 4.13: As in Figure 4.9, but without the Uinta mountains.

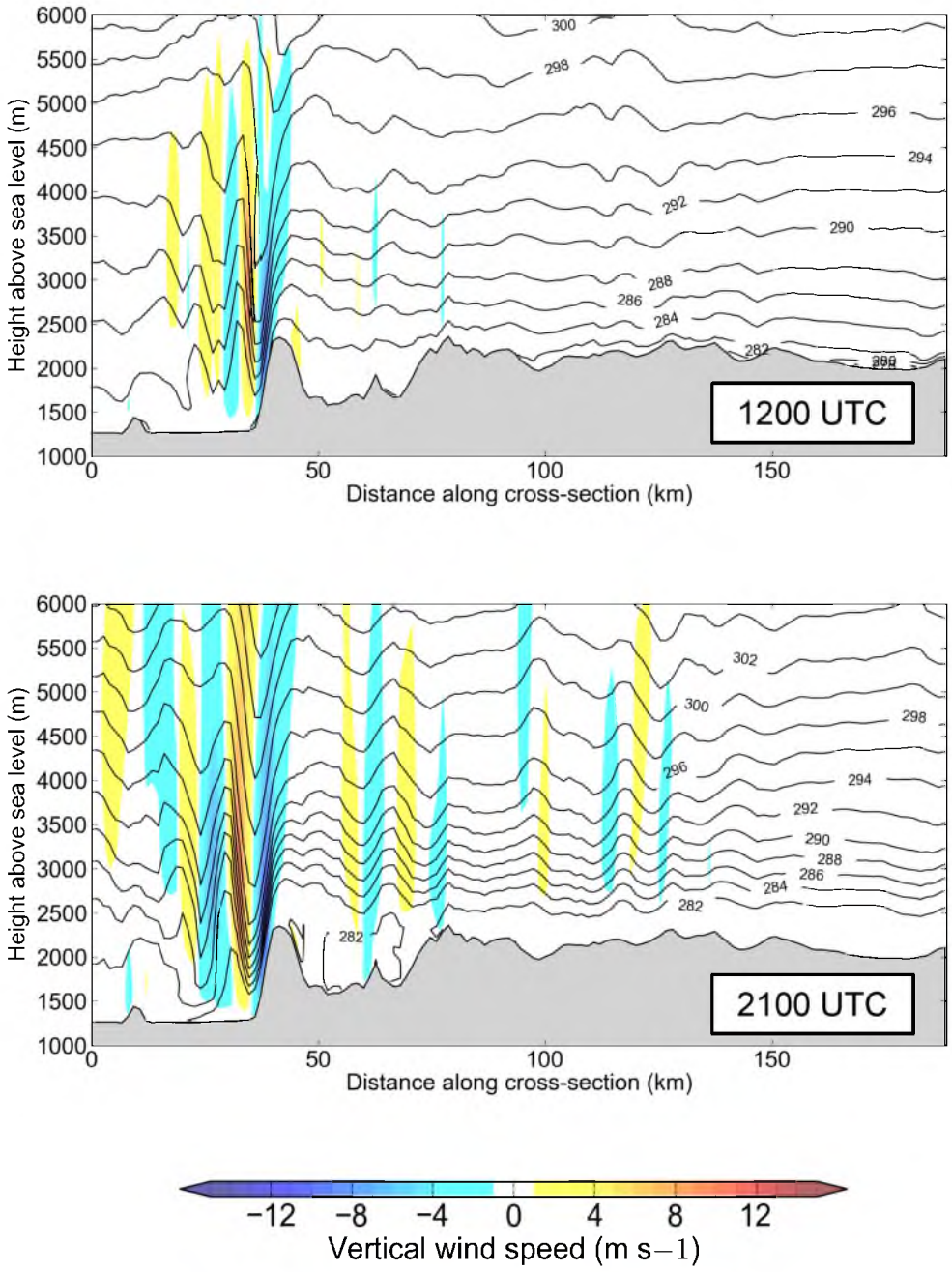

Figure 4.14: As in Figure 4.10, but without the Uinta mountains.

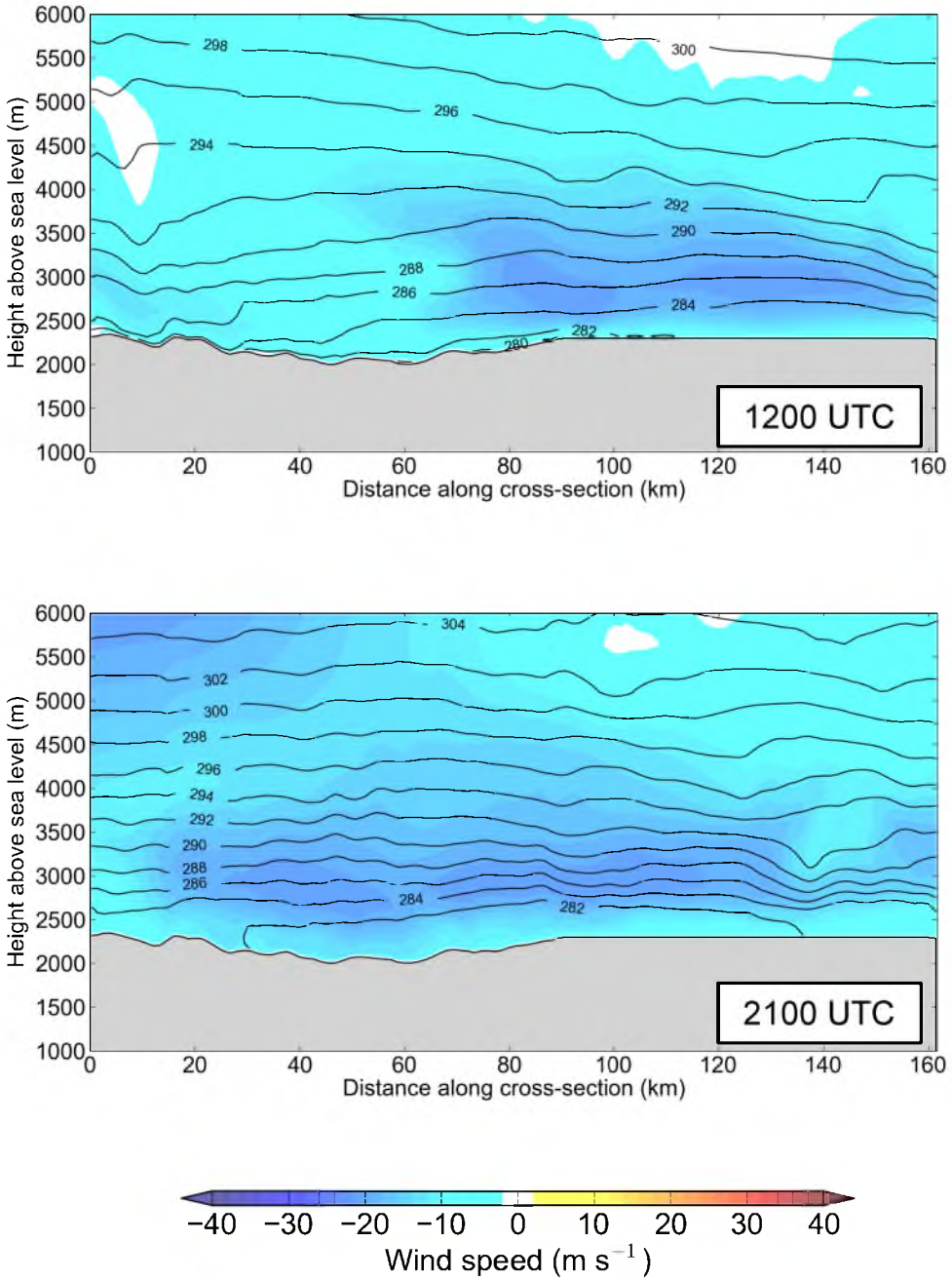

Figure 4.15: As in Figure 4.11, but without the Uinta mountains.

4.3 Predictability

To investigate the predictability of the 1 December 2011 windstorm, an ensemble of 72-h WRF simulations were initialized from 0000 UTC 29 November 2011 initial conditions from the GEFS/R2 reforecasts, and forced thereafter on the domain boundaries every six (re)forecast hours. These reforecasts are available each day from 1985 to the present for an 11-member ensemble that is approximately consistent with the operational 0000 UTC cycle of the 2012 NOAA GEFS (e.g., ~½° grid spacing and 42 levels). Due to the lack of soil data in the GEFS output files, soil boundary conditions in each GEFS member were specified from soil data from the same group of Global Forecast System reanalyses over the 72 h forecast period. This configuration is referred to as *GEFS/WRF*; the GEFS/WRF control member is *C00*; the ten perturbation ensemble members are named *E1–E10*.

The 11 GEFS/WRF model runs (C00 plus E1–E10) were initialized with identical settings as the NAM Control simulations, but with corresponding GEFS/R2 ensemble member reforecast fields providing six-hourly boundary conditions. The 700-hPa geopotential-height ensemble means are shown in Figure 4.16, which are derived from the ten perturbation ensemble members (E1–E10) during 0000–1800 UTC December 2011 (forecast lead times of 48–66 h). The ensemble means capture the general features of the evolution of this ARWB event with the ridging spreading southwestward into Wyoming during the day. However, the ensemble-mean cut-off low develops slightly east of the cut-off low observed and simulated in the NAM Control. The ensemble spread is displayed in terms of the standard deviation of the individual ensemble members about the ensemble mean. Less (more) variability within the ensemble is evident near where ridging (troughing) is present. The greatest uncertainty is found to the west of the cut-off low at 1200 and 1800 UTC. Along the Wasatch crest, flow is arriving from areas (i.e., Wyoming) experiencing reduced ensemble spread. Hence, this may contribute to enhanced predictability for the downslope windstorm, since the synoptic-scale conditions tend to be similar upstream between ensemble members.

The 700-hPa geopotential-height fields for each member of the ensemble at 1200 UTC as well as the ECMWF ERA-Interim field at the same time (i.e., 'truth') are shown in Figure 4.17. This figure allows visual evaluation of the spread within the GEFS/WRF runs at the forecast time of 60 h. Specifically, we assess (1) the depth of the cut-off low, (2)

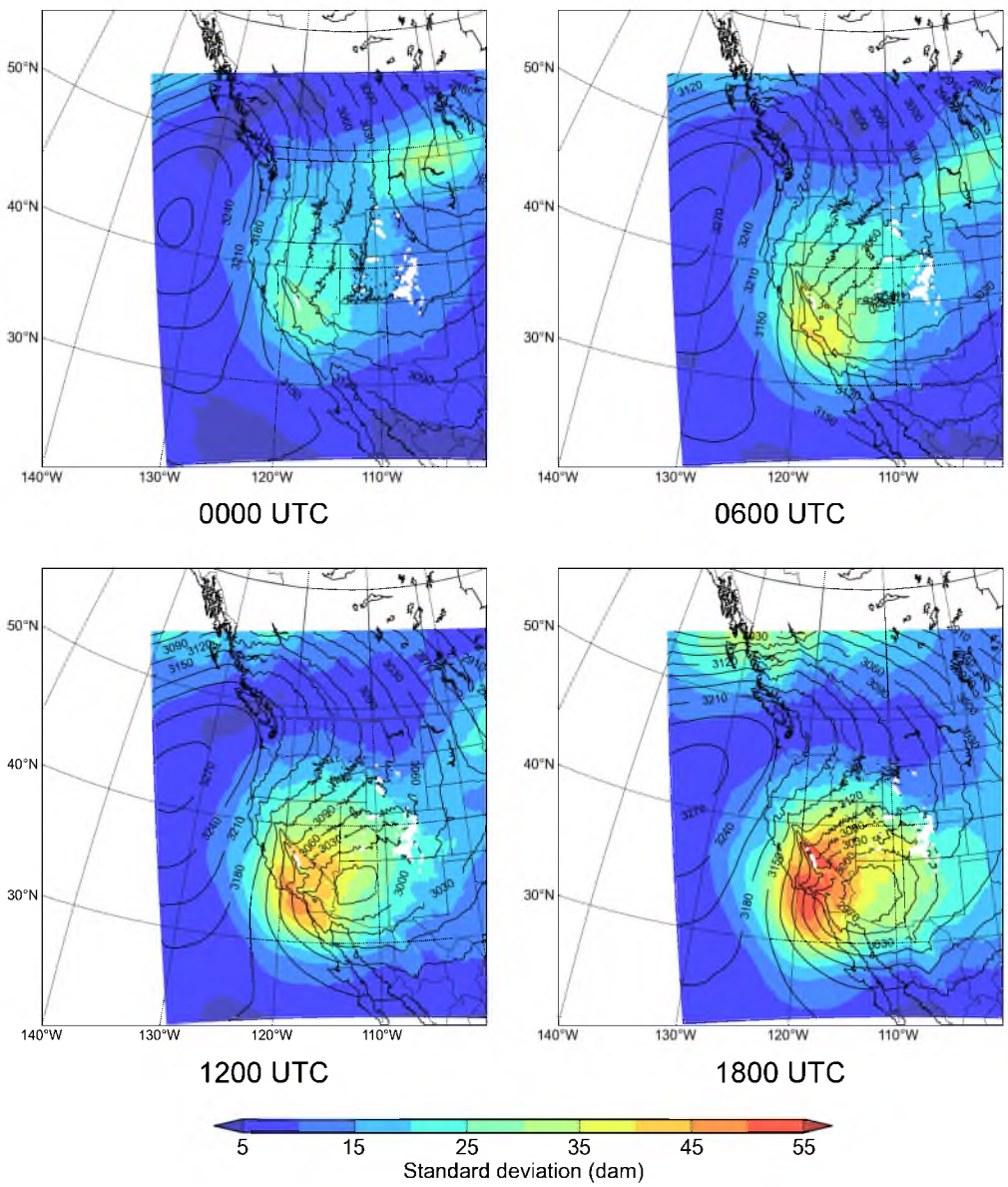

Figure 4.16: GEFS/WRF ensemble-mean 700-hPa geopotential height (contours at 30-m intervals) and ensemble standard deviation (shading according to the scale) at 6-h intervals on 1 December 2011.

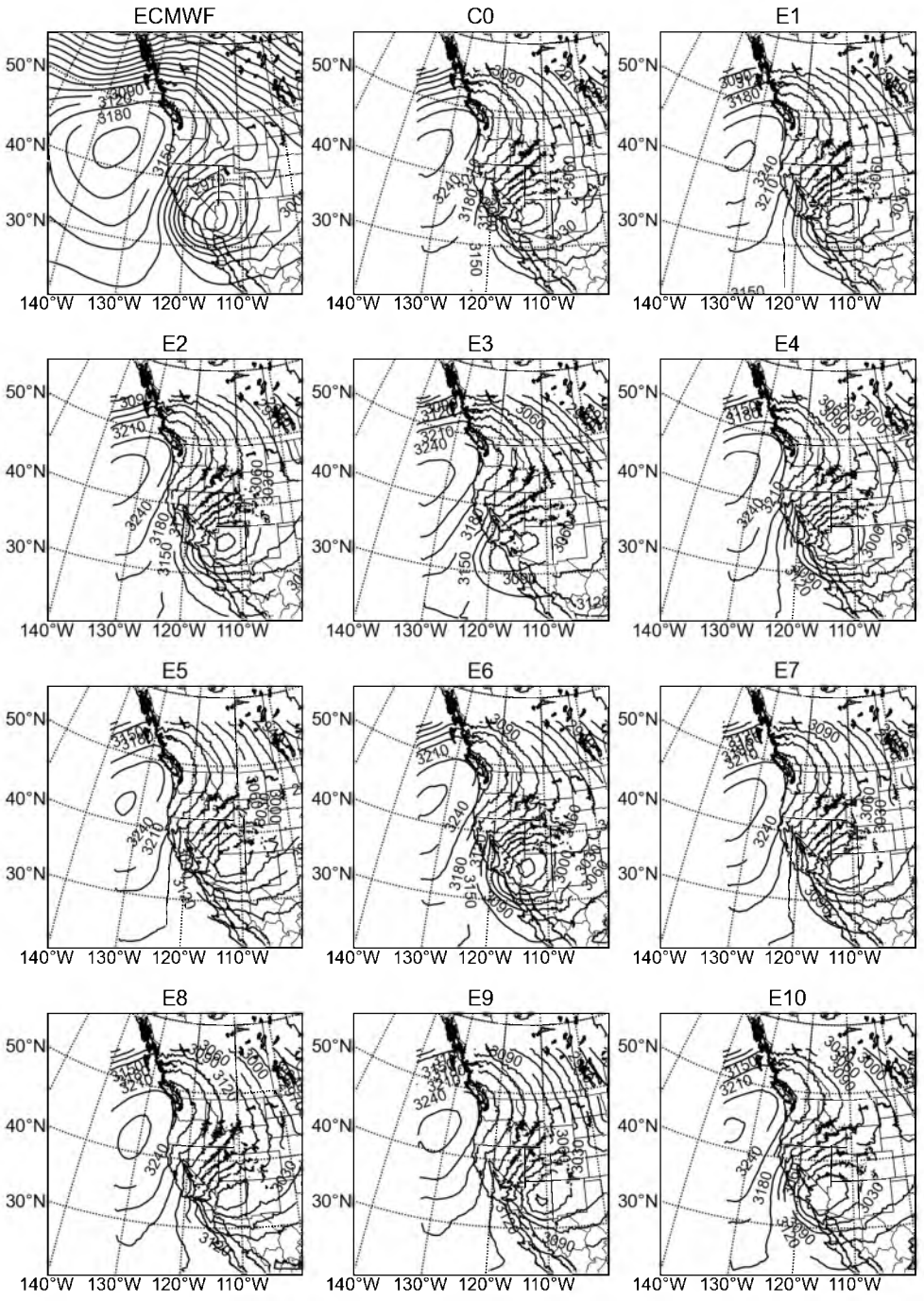

Figure 4.17: Twelve 700-hPa geopotential-height fields at 1200 UTC, 1 December 2011: ERA-Interim (upper left panel), and each of the eleven ensemble members from the GEFS/WRF runs (60 h forecast lead time). Height is contoured at 30-m intervals.

the angle of wind over the Wasatch Front (roughly crest-level flow at this level), which is related to the location of the cut-off low, and (3) the rate of cyclogenesis associated with the cut-off low. Note first that all members have the anticyclone center west of Oregon and Washington encircled by the 3270-dam contour. This is 60 dam higher than the ECMWF ERA-Interim reanalysis at the same time (first panel, Figure 4.17). This systematic bias is present throughout the 700-hPa field for the two NAM-based simulations as well as the GEFS/WRF runs (see Figure 4.1).

The lowest-contoured isohypse associated with the cut-off low ranges from 2910 dam in E6 to 3030 dam in E3. Considering the consistency in the heights associated with the anticyclone to the north, the height gradient—and the easterly gradient wind—across the Wasatch Front is largely controlled by the cut-off low's depth. The direction of the gradient wind above the Wasatch Front at 700 hPa at 1200 UTC is roughly northeasterly across all ensemble members. For a majority of ensemble members (C00, E1–E7, and E10) this flow is more easterly than northerly (i.e., clockwise of 45°), while the two exceptions, E8 and E9, have a larger northerly component and weaker and farther-eastward position of their low centers.

The evolution of the depth of the cut-off low in each ensemble member is used as a proxy for cyclogenesis. The ERA-Reanalysis low center deepens 30 dam between 0000 and 0600 UTC, and another 30 dam over the next 6 h, reaching its deepest value at 1200 UTC before then increasing by 30 dam at 1800 UTC. However, the NAM-based simulations and all GEFS/WRF ensemble members have their lowest or joint-lowest values at 1800 UTC; no cyclogenesis occurs after this time. This ~6-h delay appears to be related in GEFS/WRF runs to a lag of the ARWB event in the GEFS/WRF Control (C00) compared to 'truth'. This delay does not fundamentally affect the simulated windstorms among those ensemble members who develop one; i.e., they all appear to be delayed a similar amount. Total height falls between 0000 and 1800 UTC range from 30 dam in E3 to 150 dam in E6, which likely explains why those two are the shallowest and deepest cut-off lows, respectively.

Figure 4.18 shows maximum wind speeds near the Wasatch Front between 0000 UTC 1 December and 0000 UTC 2 December for each GEFS/WRF member, as well as for the NAM-Control simulation. Eight of the 11 GEFS/WRF develop strong windstorms (winds $>15\,\mathrm{m\,s^{-1}}$) along the Wasatch Front on this day with the peak winds centered in

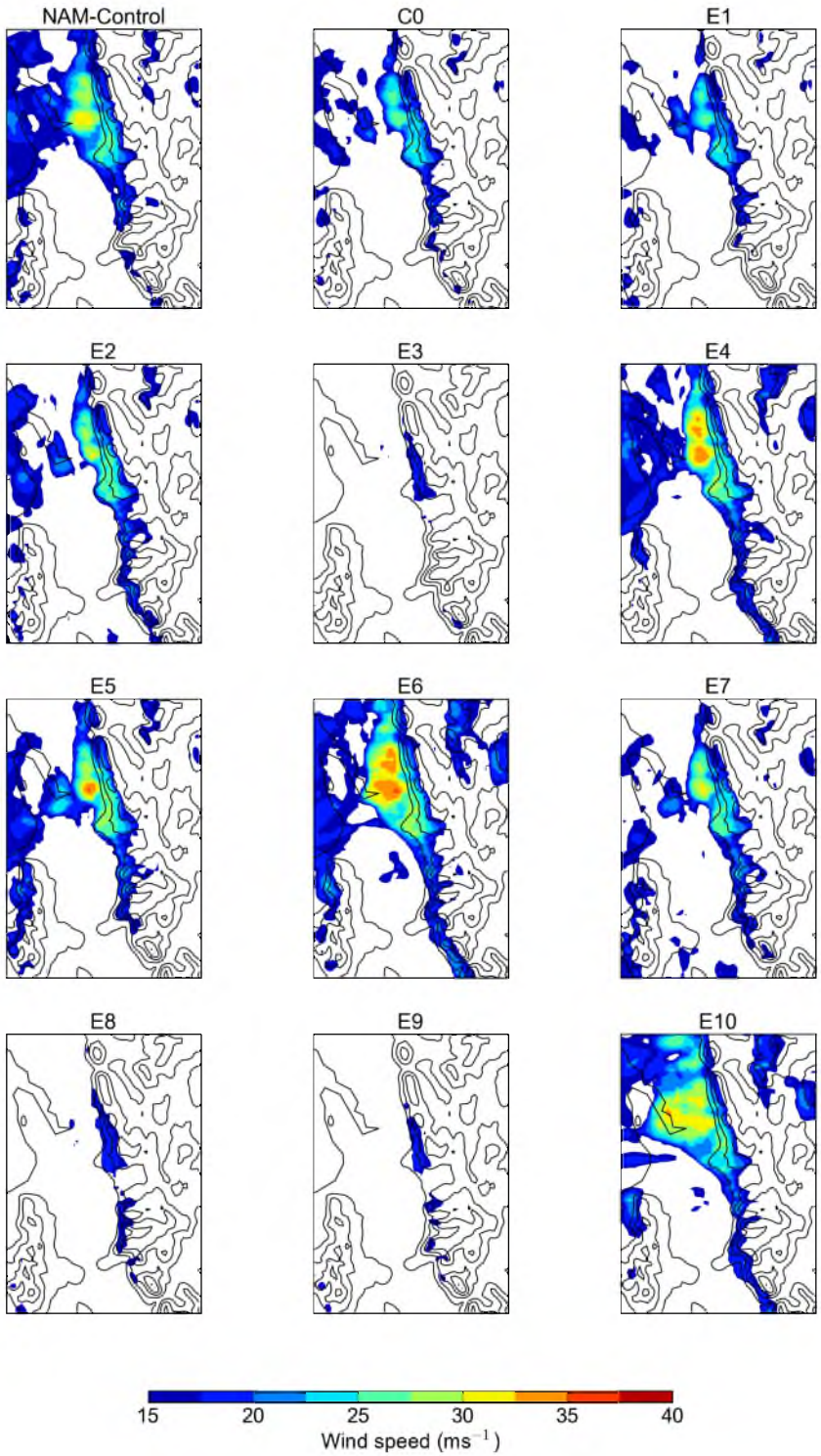

Figure 4.18: Maximum magnitude of surface wind between 0000 UTC 1 December and 0000 UTC 2 December, for the NAM-Control simulation and each GEFS-WRF ensemble forecast member. Shading according to the scale at the bottom.

Davis County. Considering these are reforecasts with lead times of 48–66 h, this result is quite remarkable. Some of the synoptic-scale features evident in Figure 4.17 appear to explain common features leading to downslope windstorms in this case. The strongest (E6) and joint-weakest (E3) winds along the Wasatch Front occur with the deepest and shallowest 700-hPa geopotential-height lows at 1200 UTC, respectively. Furthermore, the three weakest cut-off lows at 1200 UTC all are associated with a lack of strong winds along the Front (E3, E8, and E9). We note that two of the three members in which windstorms do not initiate (E7 and E8) have more northerly 700-hPa gradient wind associated with cut-off lows located farther east. Finally, while an ensemble member without a windstorm (E3) also has the lowest rate of deepening (30 dam over 18 h), the strongest-wind member (E6) sees only average deepening compared with all members (90 dam over 18 h). Moreover, the two members with the most deepening over 18 h, E4 (150 dam) and E7 (120 dam), do not reach the same high wind intensity as E6. Hence, it is more likely that the intensity, location, and orientation of the cut-off low is more critical than its rate of deepening.

Based on Figure 4.18, the GEFS/WRF perturbation members can be subjectively divided into two clusters: (1) the seven perturbed ensemble members with strong winds along the Wasatch Front (broadly similar to those observed as well as simulated in the NAM-Control and GEFS/WRF control) are grouped as Cluster-W (E1, E2, E4–E7, E10) and (2) those perturbed members that do not generate a windstorm are grouped as Cluster-N (E3, E8, and E9). By averaging the fields from the members that belong to each cluster, and differencing the two averages, we gain more insight into the conditions that lead to Wasatch windstorms than from examining ensemble means that blur the features of the two dominant clusters (Ancell 2013). Figure 4.19 shows the differences in potential temperature and wind speed at 1800 UTC between Cluster-W and Cluster-N, along the same cross-sections used earlier in Figures 4.9 and 4.11. 1800 UTC is shown rather than 1200 UTC since, as discussed previously, the GEFS/WRF members initialized at 0000 UTC 29 November tend to delay the windstorms by ~6 h. As shown in Figure 4.19, Cluster-W members tend to have stronger easterly wind, but little difference in stability, evident in both cross-sections. The blocking of northeasterly flow across Wyoming by the Uintas and the development of a barrier-jet-like feature across Wyoming towards the Wasatch Mountains may contribute to enhancing the predictability of the windstorms; i.e., subtle shifts in the

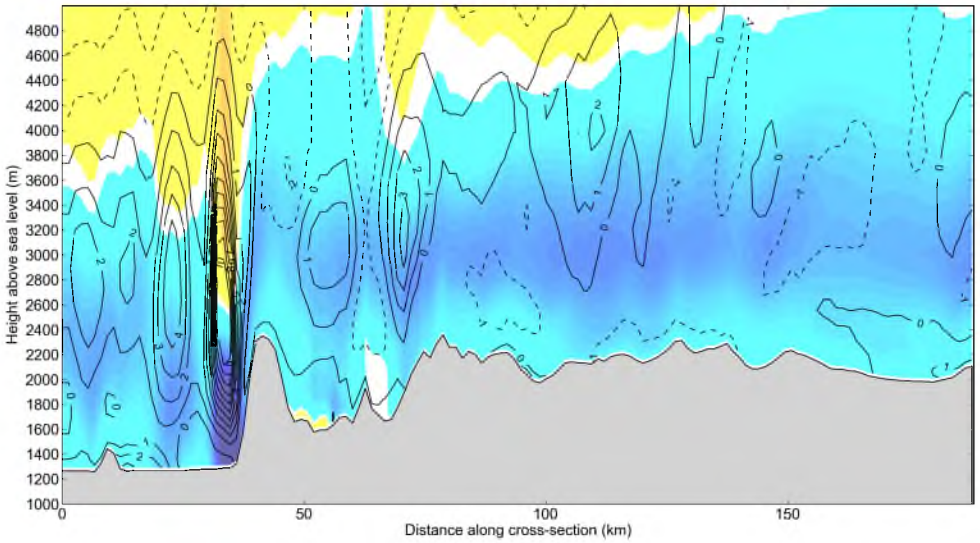

(a)

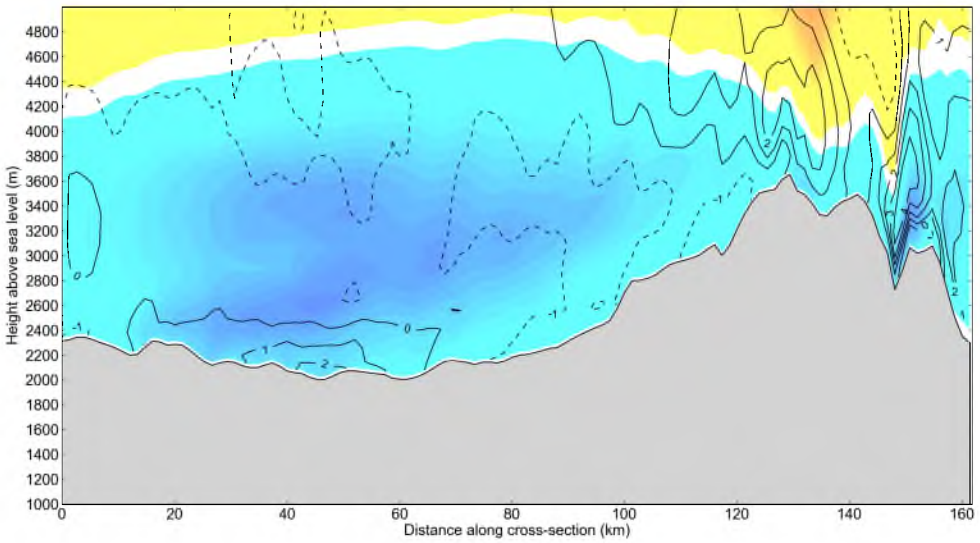

(b)

(c)

Figure 4.19: Difference at 1800 UTC, 1 December 2011, in the GEFS/WRF composite means (seven high-surface-wind cases minus three low-surface-wind cases) of potential temperature (contours at 1-K intervals) and wind (shading according to the scale at the bottom) along the (a) southwest–northeast (A–B) and (b) north–south (C–D) cross-sections shown in Figure 1.1.

orientation of the crest-level flow may be less important within this confluent airstream.

At the surface, high-temporal-resolution time series of wind speed were created from each ensemble member at many locations including Centerville, Ogden Peak, and KSLC (Figure 4.20). The onset of the downslope windstorms in the C00 simulation and seven of the ensemble members is evident between 66 h (E6) and 76 h (E7) into the simulation with their demise between 72 h (E1) and 84 h (E6). The similarities among some of the ensemble members regarding the overall temporal signature of the windstorm at Centerville is quite remarkable. The three outliers that do not develop windstorms have conspicuously-low wind speeds (E3, E8, and E9). Three ensemble members (E4, E6, and E10) begin the windstorm before or close to the time it was observed (0900 UTC) and continue slightly beyond the observed cessation time. Three others (C00, E1 and E2) delay the onset of the windstorm until after 1200 UTC, while the remaining two members (E5 and E7) delay the onset until after 1500 UTC. From Figure 4.17, it is clear that the synoptic-scale flow in the E4, E6, and E10 members was favorable by 1200 UTC for crest-level easterly flow. Further, the simulated easterly winds at Ogden Peak in these ensemble members were strong sooner (Figure 4.20b). However, differences in cross-barrier flow between many other ensemble members were small; E5 and E7 differed in consistent fashion as their crest-level peak winds occurred later. The lack of predictability away from the downslope windstorm during this period is evident at many locations, including the chaotic wind speeds observed at Salt Lake City, for example (Figure 4.20c).

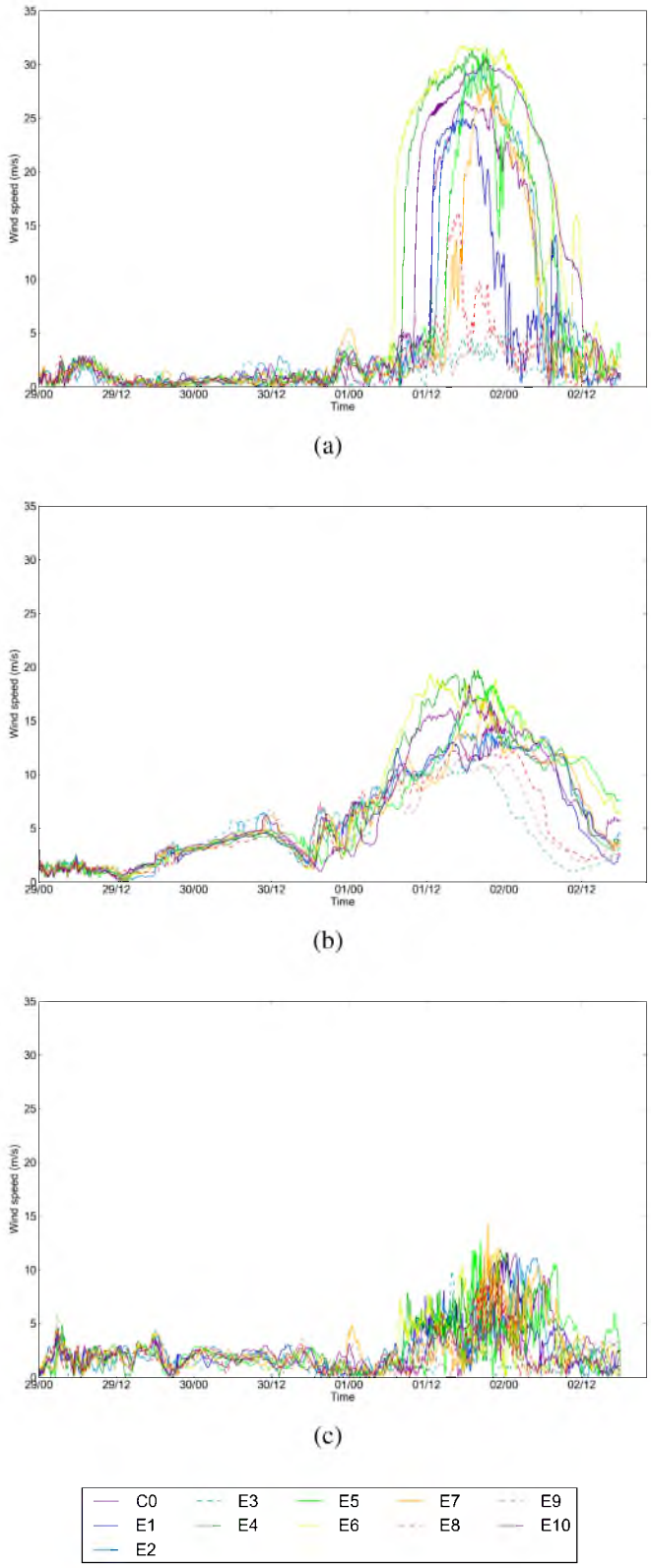

Figure 4.20: Surface wind speeds from the eleven GEFS/WRF ensemble members at: (a) Centerville, (b) Ogden Peak, and (c) Salt Lake City.

CHAPTER 5

SUMMARY

This study documented a severe downslope windstorm in northern Utah, which caused over $75 m damage along a narrow swath along the Wasatch Front on 1 December 2011. Planning for this study began the day before it happened and was motivated by a number of factors: (1) operational numerical guidance and forecaster experience led to high confidence that a major downslope wind storm was possible; (2) verification of this forecast would lead to the first major downslope windstorm along the Wasatch Front in over a decade; (3) experimental high-resolution numerical forecasts run by the Salt Lake City National Weather Service Office were providing considerable specificity regarding the details of the impending storm; and (4) routine automated observations were already in place throughout the region such that a small number of additional observational assets available in the Department of Atmospheric Sciences could be used advantageously to mount a small field campaign to study the event. The resulting severity of the event combined with the apparent accuracy of the high-resolution model guidance and unprecedented data set for a Wasatch downslope windstorm ultimately led to completion of this study. As summarized in Chapter 1, this study is framed by five scientific questions. These questions will now be addressed based on the results presented in the preceding chapters.

5.1 How does this downslope windstorm compare to previous ones?

Holland (2002) provided a more comprehensive climatology of Wasatch downslope windstorms based on their occurrence at KHIF. Extending that work to include this event indicates that it had the second-highest maximum wind speed and gust at KHIF since 1979. The synoptic setup for this event was clearly established by ARWB. The large-scale characteristics of this episode (Figure 3.5) are quite similar to the small composite of major

wind events since 1979 (cf. Figure 3.3).

The original goal of the climatological work in this study was to address the causes for the lack of high wind events between 2000 and 2010, which is not likely related to changes to sensor exposure. The ARWB climatology developed by Strong and Magnusdottir (2008) was examined to assess whether there were fewer such episodes during this period over western North America. However, the results of that investigation were inconclusive in part because the methodology used to define ARWB events in that climatology allows for a wide spectrum of ARWB sizes and magnitudes. Similarly, there was no strong evidence to suggest that crest-level easterly winds were simply less frequent during the 2000–2010 period (Figure 3.1).

Compared to similar windstorms around the world, the Wasatch windstorm of 1 December 2011 had much in common with Bora windstorms of southeastern Europe: pulsating winds, gradual cooling, and destructive force (Smith and Sun 1987). They also resembled those observed on East Falkland: occurrence in the lee of steep but modest terrain, and within anomalous large-scale flow Mobbs et al. (2005).

The 1 December 2011 downslope windstorm occurred as a result of a well-defined synoptic setting, which can be summarized as follows:

- An ARWB event over western North America established the prevailing easterly flow in the midtroposphere over the Wasatch Mountains. The stalling of the associated potential vorticity maximum over southern Nevada maintained this easterly flow's position over the Wasatch range, and sustained the downslope windstorm past their typical demise during late morning.

- The gradient easterly wind near crest-level (700 hPa) developed rapidly between 0600 and 1200 UTC, initially oriented from the northeast, but veering by 1800 UTC to be more directly from the east before weakening after 2100 UTC.

- Common to downslope windstorms in other areas, mountain waves generated from the easterly flow orthogonal to the Wasatch may have been reflected back towards the surface by the stable layer (Smith 1985). This process may have also generated its own critical layer, seen in observational and numerical-simulation data, where

the cross-barrier component to the flow falls to zero (Peltier and Clark 1979) in downstream, and not upstream, profiles.

- As the large-scale lower-tropospheric height gradient from Wyoming to Nevada increased during the day, cold air surged across Wyoming. The Uinta Mountains may have shunted the initially northeasterly flow towards the Wasatch Front, leading to a barrier-jet-like feature, which could help advect the cold air westwards. Cold air filled in the lowest depressions allowing the barrier jet to continue downstream (and immediately upstream of the Wasatch Mountains at Morgan, UT) at an elevation of a few hundred meters above crest level.

5.2 What were the local characteristics of this event?

The downslope winds began abruptly ~0900 UTC in Davis County resulting from the initial push of the easterly flow across the Wasatch Mountains and trapped beneath the stable layer further aloft. The strongest winds were observed ~1500 UTC in Centerville, and ended abruptly in Davis County after 1900 UTC. A feature of this event uncommon to previous ones was the progression through midday of the strongest winds, and the subsequent damage further north into Weber County. The cross-barrier flow measured at OGP immediately above the locations in Weber County where damage occurred (including the Weber State University campus) continued to increase until late afternoon as a result of the synoptic-scale shifts in the large-scale flow (Figure 3.8). Observations during the morning from a vehicle-mounted sensor filled the spatial gaps between the automated observing sites along the Wasatch Front. Although peak winds were observed at numerous favored locations (fewer upstream obstructions, etc.), there was a general uniformity of the flow spilling over the mountains and reaching their base (i.e., widespread strong easterly winds of quasi-constant potential temperature that was close to values observed at jet level upstream of the Wasatch, and low dewpoint temperature). Temperatures within Weber Canyon from the vehicle-mounted sensor and at PWR were lower, indicating the additional effects of low-level gap flows travelling through this canyon (Figure 3.9).

The data from the rawinsonde released at 1100 UTC in Centerville revealed a clear underflow near the surface (Armi and Mayr 2011) before the sonde ascended rapidly within a rotor. An extremely-sharp subsidence inversion capped the rotor with strong winds

observed at that level. This bifurcation of the strongest winds (at the surface and at the level of the inversion) is similar to that found in large-eddy simulations of downslope flows (e.g., Hertenstein 2009). The characteristics of a self-induced critical layer further aloft may also be evident (Peltier and Clark 1979). The localized nature of the characteristic features of downslope windstorms below the crest of the Wasatch Range found near Centerville is apparent by comparing the vertical profiles at Centerville to the sounding at KSLC. The KSLC sounding has typical morning downvalley flows, decoupled from a well-mixed layer below crest-level, and hints of strong turbulence below a strong inversion near 700 hPa (Figure 3.14). Not surprisingly, the two profiles of temperature, moisture, and wind are quite similar to one another above crest level.

5.3 To what extent can a high-resolution model simulation capture temporal and spatial evolution of mesoscale and local features of the event?

Even with the relatively-rich observational data set available to examine this windstorm, a high-resolution WRF numerical simulation forced by NAM-analyzed conditions on the outer boundary provides critical information on the dynamical and thermodynamical structure associated with the event. Fortunately, the WRF model output maintained many of the synoptic-scale features evident from the ERA-Interim Reanalyses. The breaking of the Rossby wave in WRF output was slightly slower; deepening of the cut-off low continued until 1800 UTC over southern Nevada, whereas at this point, ERA-Interim reanalysis showed filling of the low to have already started.

The model 10-m winds along the Wasatch Front had many similarities to those observed, including maximum winds in Davis County, and strong winds in Weber County later in the day. However, the model's 10-m winds at crest level tended to be weaker than those observed along the crest. Examination of both vertical profiles and cross-sections in model output as a function of time illuminated the dynamical features of the windstorm. Earlier in the storm, model output showed characteristics of the barrier jet; later, it revealed a wider easterly push across Wyoming and the Wasatch Mountains. However, the model's response to the flow across the Wasatch barrier beneath the strong stable layer is to develop a stronger mountain wave/hydraulic jump than was likely present. This results in model vertical profiles at the western base of the Wasatch Mountains that are more akin

to extreme-amplitude mountain-wave windstorms (e.g., Grubišić and Billings 2008). The model creates a band of dry air, flowing parallel down the terrain along isentropes, from high above the model terrain and plunging close to the surface. A lateral jet, evident in the Centerville observed profile surmounting the superadiabatic layer, does not form in the model simulation.

5.4 What are the impacts of upstream mountain ranges that may deflect the flow traveling towards the Wasatch Mountains?

Following similar WRF-terrain modification by West and Steenburgh (2011) and Alcott and Steenburgh (2013), we investigated the ability of the Uinta Mountains (a major barrier to meridional flow across the Wyoming/Utah border) to steer northeasterly lower-tropospheric flow more directly towards the Wasatch Mountains. If the Uinta Mountains are leveled in a WRF simulation to an elevation only slightly higher than that of much of western Wyoming, then southwestward cold advection is less apt to be blocked, and spills further south across the Wasatch Front into Utah County. However, as synoptic-scale flow later in the day veers towards due-easterly, then the blocking effect of the Uinta Mountains is lessened.

5.5 Is the enhanced forecast skill for this windstorm evident in an ensemble reforecast?

The NWS first mentioned a possible downslope windstorm along the Wasatch Front in an AFD ~90 h before its onset. Confidence in this forecast was supported by operational high-resolution model runs. To evaluate this apparent enhanced mesoscale predictability, an ensemble of WRF runs was performed, with all reforecast data taken from a GEFS/R2 forecast initialized 29 November with each member forced on its boundary by a corresponding GEFS/R2 ensemble member. To the author's knowledge, few (if any) GEFS-forced WRF simulations have been created in this fashion. Caveats for this study to evaluate predictability of this event include: concerns related to underdispersion of the perturbation ensemble members; the limited number (10) of perturbed ensemble members (compared to 100 ensemble members used by Reinecke and Durran 2009; Durran et al. 2012); and the evaluation of a single GEFS reforecast time.

Ultimately, seven of the ten perturbation members, plus the control member, success-

fully simulated a windstorm in the correct location and of comparable magnitude. The other three failed to do so, revealing a bimodal distribution. However, the windstorms in all members were delayed by ~6 h, related to the slower evolution of the associated ARWB in this reforecast's initial analysis.

The differences between ensemble members were primarily related to differences in 700-hPa gradient wind direction, and the geopotential-height depth of the low center over southern Nevada at this level. Figure 4.19 showed the differences between with-windstorm and no-windstorm ensemble members along north–south and southwest–northeast cross-sections at 1800 UTC, and revealed the critical distinction in with-windstorm members to be stronger easterly winds upstream of the Wasatch crest. Surprisingly, there was little difference in potential temperature profiles.

The spread in ensemble members was especially apparent in time series of winds at Centerville and KSLC. At Centerville, there is very little spread between members during the first ~66 h; in contrast, between 0600 UTC 1 December and 1200 UTC 2 December, the members diverge significantly, in general falling into with-windstorm and no-windstorm clusters (especially ~1900 UTC 1 December). The time series at KSLC reveals good agreement while in large-scale northerly flow, which suggests the large scale was at this time more predictable. During and after the windstorm, however, there is no discernible coherency between any ensemble members at KSLC.

5.6 New questions and future work

The climatology of Wasatch windstorms marked a barren period between 2000 and 2010 where no criteria-matching windstorms occurred at KHIF. It was shown that this was not directly related to the frequency of strong winter easterly flow at 700 hPa. A climatology of cut-off lows centered on southern Nevada may highlight a potential explanation for this dearth of windstorms. Conversely, the answer may be even more complex, and demand a more rigorous study.

Peak winds associated with Wasatch windstorms often begin around sunrise, at the time of maximum static stability. Independently, the strongest large-scale forcing is provided when the gradient wind at 700 hPa is somewhat clockwise of 45°. The phasing of these two ingredients may be related to previous forecast failures, but was not investigated in this

study.

Santa Ana winds near Los Angeles, California, were creating a similar magnitude of disruption at roughly the same time as the Wasatch windstorm on December 1, 2011. It follows that the forecast of these Santa Ana winds was likely challenging: Figure 4.16 highlights the large spread in ensemble members in this region at the same time as damage was occurring along the Wasatch Front. Future investigation into predictability of this and other Santa Ana cases, occurring on the cyclonic side of the ARWB event, would make an interesting counterfoil to this study of Wasatch windstorms.

The origin of the extended predictability associated with this windstorm remains unknown. Uncertainty in numerical forecasts is often large downstream of diffluent, strong wind such as jet-exit regions (e.g., Oortwijn 1998). Conversely, confluent airstreams bring together parcel pairs, reducing initial-condition uncertainty to an extent (measured by the Lyapunov exponent by Cohen and Schultz 2005). Hence, confluence north of the Uinta Mountains, leading to an easterly barrier jet upstream of the Wasatch Front, may enhance the predictability of Wasatch windstorms. A second GEFS/WRF ensemble run, but without the Uinta mountains, may address the magnitude to which predictability is sensitive to their upstream presence. Air parcel trajectories may also highlight confluence seen near the Uintas. In addition, it is unknown whether the longer predictability seen in this Wasatch windstorm is related to its association with ARWB. As seen in Figure 4.16, there is little spread in regions of higher geopotential heights, which are upstream of the Wasatch Front in the Wasatch windstorm configuration. This may yield an ensemble mean closer to verification than in windstorms associated with prevailing westerlies (Boulder; in the Owens Valley).

While these results apparently reveal a surprisingly-long predictable timescale for windstorm phenomena, compared to $\sim$12 h seen by Reinecke and Durran (2009), this one case study says nothing of their generality to all Wasatch windstorms. In fact, a weaker windstorm on 4–5 May 2013 along the same zone as in this study was underestimated by around a factor of two; gusts of over 25 m s^{-1} at Centerville were not mentioned in the final AFD before they occurred. Whether this apparent lack of predictability is related to diminished larger-scale forcing (e.g., Islam et al. 1993; Hohenegger and Schär 2007) remains a future research question. Moreover, error growth can be constrained by strong

synoptic-scale forcing that quickly advects away small perturbations (Zhang et al. 2003). The dry nature of Wasatch windstorms may also preclude large upscale growth of errors seen in other mesoscale predictability studies (summarised by Durran et al. 2012). The abundance of GEFS/R2 data, available from 1985 to the present (Hamill et al. 2013), allows similar predictability studies to this one for other Wasatch windstorms, both weakly and strongly forced.

REFERENCES

Abatzoglou, J. T., R. Barbero, and N. J. Nauslar, 2013: Diagnosing Santa Ana winds in Southern California with synoptic-scale analysis. *Weather and Forecasting*, **28**, 704–710.

Alcott, T. and W. J. Steenburgh, 2013: Orographic influences on a Great Salt Lake-effect snowstorm. *Monthly Weather Review*, **141**, 2432–2450.

American Meteorological Society, 2013: Glossary of Meteorology: downslope windstorm. URL `http://glossary.ametsoc.org/wiki/Downslope_windstorm`

Ancell, B. C., 2013: Nonlinear characteristics of ensemble perturbation evolution and their application to forecasting high-impact events. *Weather and Forecasting*, in press.

Armi, L. and G. J. Mayr, 2011: The descending stratified flow and internal hydraulic jump in the lee of the Sierras. *Journal of Applied Meteorology and Climatology*, **50**, 1995–2011.

Chrust, M. F., C. D. Whiteman, and S. W. Hoch, 2013: Observations of thermally driven wind jets at the exit of Weber Canyon, Utah. *Journal of Applied Meteorology and Climatology*, **52**, 1187–1200.

Cohen, R. A. and D. Schultz, 2005: Contraction rate and its relationship to frontogenesis, the Lyapunov exponent, fluid trapping, and airstream boundaries. *Monthly Weather Review*, **133**, 1353–1369.

Colman, B. and C. Dierking, 1992: The Taku wind of Southeast Alaska: its identification and prediction. *Weather and Forecasting*, **7**, 49–64.

Decker, S. and D. Robinson, 2011: Unexpected high winds in Northern New Jersey: a downslope windstorm in modest topography. *Weather and Forecasting*, **26**, 902–921.

Dee, D. P., S. M. Uppala, A. J. Simmons, P. Berrisford, P. Poli, S. Kobayashi, U. Andrae, M. A. Balmaseda, G. Balsamo, P. Bauer, P. Bechtold, A. C. M. Beljaars, L. van de Berg, J. Bidlot, N. Bormann, C. Delsol, R. Dragani, M. Fuentes, A. J. Geer, L. Haimberger, S. B. Healy, H. Hersbach, E. V. Hólm, L. Isaksen, P. Kå llberg, M. Köhler, M. Matricardi, A. P. McNally, B. M. Monge-Sanz, J.-J. Morcrette, B.-K. Park, C. Peubey, P. de Rosnay, C. Tavolato, J.-N. Thépaut, and F. Vitart, 2011: The ERA-Interim reanalysis: configuration and performance of the data assimilation system. *Quarterly Journal of the Royal Meteorological Society*, **137**, 553–597.

Doyle, J. and D. Durran, 2002: The dynamics of mountain-wave-induced rotors. *Journal of the Atmospheric Sciences*, **59**, 186–201.

Doyle, J., C. Epifanio, A. Persson, P. Reinecke, and G. Zängl, 2013: Mesoscale modeling over complex terrain: numerical and predictability perspectives. *Mountain Weather Research and Forecasting: Recent Progress and Current Challenges*, F. Chow, S. De Wekker, and B. Snyder, eds., Springer, 531–590.

Durran, D., P. Reinecke, and J. Doyle, 2012: Large-scale errors and mesoscale predictability in Pacific Northwest snowstorms. *Journal of the Atmospheric Sciences*, **70**, 1470–1487.

Grubišić, V. and B. J. Billings, 2008: Climatology of the Sierra Nevada mountain-wave events. *Monthly Weather Review*, **136**, 757–768.

Hamill, T. M., G. T. Bates, J. S. Whitaker, D. R. Murray, M. Fiorino, T. J. Galarneau, Y. Zhu, and W. Lapenta, 2013: NOAA's second-generation global medium-range ensemble reforecast data set. *Bulletin of the American Meteorological Society*, in press.

Hertenstein, R. F., 2009: The influence of inversions on rotors. *Monthly Weather Review*, **137**, 433–446.

Hohenegger, C. and C. Schär, 2007: Atmospheric predictability at synoptic versus cloud-resolving scales. *Bulletin of the American Meteorological Society*, **88**, 1783–1793.

Holland, L., 2002: *Downslope windstorms along the Wasatch Front*. M. S. Thesis, University of Utah, 86 pp.

Horel, J., T. Potter, L. Dunn, W. Steenburgh, M. Eubank, M. Splitt, and D. Onton, 2002a: Weather support for the 2002 Winter Olympic and Paralympic Games. *Bulletin of the American Meteorological Society*, **83**, 227–240.

Horel, J., M. Splitt, L. Dunn, J. Pechmann, B. White, C. Ciliberi, S. Lazarus, J. Slemmer, D. Zaff, and J. Burks, 2002b: Mesowest: cooperative mesonets in the western United States. *Bulletin of the American Meteorological Society*, **83**, 211–225.

Hoskins, B., M. McIntyre, and A. Robertson, 1985: On the use and significance of isentropic potential vorticity maps. *Quarterly Journal of the Royal Meteorological Society*, **111**, 877–946.

Islam, S., R. Bras, and K. Emanuel, 1993: Predictability of mesoscale rainfall in the Tropics. *Journal of Applied Meteorology*, **32**, 297–310.

Jiang, J. H., 2002: Upper Atmosphere Research Satellite (UARS) MLS observation of mountain waves over the Andes. *Journal of Geophysical Research*, **107**, 8273.

Kühnlein, C., A. Dörnbrack, and M. Weissmann, 2013: High-Resolution Doppler Lidar Observations of Transient Downslope Flows and Rotors. *Monthly Weather Review*, in press.

Lilly, D. K. and E. J. Zipser, 1972: The Front Range windstorm of 11 January 1972: a meteorological narrative. *Weatherwise*, **25**, 56–63.

Lorenz, E., 1969: The predictability of a flow which possesses many scales of motion. *Tellus*, **21**, 289–307.

Manley, G., 1945: The Helm Wind of Crossfell, 1937-1939. *Quarterly Journal of the Royal Meteorological Society*, **71**, 197–219.

Markowski, P. and Y. Richardson, 2010: *Mesoscale Meteorology in Mid-latitudes*. Wiley-Blackwell, 407 pp.

Marriott, W., 1886: The Helm Wind of August 19th, 1885. *Quarterly Journal of the Royal Meteorological Society*, **12**, 1–10.

McIntyre, M. M. and T. Palmer, 1984: The 'surf zone' in the stratosphere. *Journal of Atmospheric and Terrestrial Physics*, **46**, 825–849.

Mobbs, S., S. Vosper, P. Sheridan, R. Cardoso, R. Burton, S. Arnold, M. Hill, V. Horlacher, and A. Gadian, 2005: Observations of downslope winds and rotors in the Falkland Islands. *Quarterly Journal of the Royal Meteorological Society*, **131**, 329–351.

Norte, F. A., A. G. Ulke, S. C. Simonelli, and M. Viale, 2008: The severe Zonda wind event of 11 July 2006 east of the Andes Cordillera (Argentine): a case study using the BRAMS model. *Meteorology and Atmospheric Physics*, **102**, 1–14.

O'Donoghue, A. J., 2012: Remembering the winds of 2011: Utah's 'most devastating wind event' in decades happened 1 year ago. *Deseret News*, Salt Lake City.

Oortwijn, J., 1998: Predictability of the onset of blocking and strong zonal flow regimes. *Journal of the Atmospheric Sciences*, **55**, 973–994.

Palmer, T., 1993: Extended-range atmospheric prediction and the Lorenz model. *Bulletin of the American Meteorological Society*, **74**, 49–65.

Peltier, W. and T. Clark, 1979: The evolution and stability of finite-amplitude mountain Waves. Part II: surface wave drag and severe downslope windstorms. *Journal of Atmospheric Sciences*, **36**, 1498–1529.

Peltier, W. and J. Scinocca, 1990: The origin of severe downslope windstorm pulsations. *Journal of the Atmospheric Sciences*, **47**, 2853–2870.

Reinecke, P. and D. Durran, 2009: Initial-condition sensitivities and the predictability of downslope winds. *Journal of the Atmospheric Sciences*, **66**, 3401–3418.

Richner, H. and P. Hächler, 2013: Understanding and forecasting Alpine Foehn. *Mountain Weather Research and Forecasting: Recent Progress and Current Challenges*, F. Chow, S. De Wekker, and B. Snyder, eds., Springer, 219–260.

Silver, N., 2012: *The Signal and the Noise: Why So Many Predictions Fail – but Some Don't*. Penguin, 544 pp.

Smith, R., 1985: On severe downslope winds. *Journal of the Atmospheric Sciences*, **42**, 2597–2603.

Smith, R. and J. Sun, 1987: Generalized hydraulic solutions pertaining to severe downslope winds. *Journal of Atmospheric Sciences*, **44**, 2934–2939.

Steenburgh, W., 2013: A Major Forecast Bust.
URL `http://wasatchweatherweenies.blogspot.com/2013/05/a-major-forecast-bust.html`

Strong, C. and G. Magnusdottir, 2008: Tropospheric Rossby wave breaking and the NAO/NAM. *Journal of the Atmospheric Sciences*, **65**, 2861–2876.

Thorncroft, C. D., B. Hoskins, and M. McIntyre, 1993: Two paradigms of baroclinic-wave life-cycle behaviour. *Quarterly Journal of the Royal Meteorological Society*, **119**, 17–55.

Vosper, S., 2004: Inversion effects on mountain lee waves. *Quarterly Journal of the Royal Meteorological Society*, **130**, 1723–1748.

Wei, M., Z. Toth, R. Wobus, and Y. Zhu, 2008: Initial perturbations based on the ensemble transform (ET) technique in the NCEP global operational forecast system. *Tellus A*, **60**, 62–79.

Welch, W. and D. Rice, 2011: 100-mph Santa Ana winds whip Southwest. *USA Today*.

West, G. L. and W. Steenburgh, 2011: Influences of the Sierra Nevada on Intermountain cold-front evolution. *Monthly Weather Review*, **139**, 3184–3207.

Whiteman, C. D., 2000: *Mountain Meteorology: Fundamentals and Applications*. Oxford University Press, USA, New York, 355 pp.

Zhang, F., C. Snyder, and R. Rotunno, 2003: Effects of moist convection on mesoscale predictability. *Journal of the Atmospheric Sciences*, **60**, 1173–1185.